Biochemical Applications of FT-IR Spectroscopy

Arthur Pistorius

Voor Myriam
Aan Fransje en Max

Biochemical Applications of FT-IR Spectroscopy

Een wetenschappelijke proeve op het gebied van de
Natuurwetenschappen

Proefschrift

ter verkrijging van de graad van doctor
aan de Katholieke Universiteit Nijmegen,
volgens besluit van het College van Decanen in het
openbaar te verdedigen op woensdag 25 september 1996,
des namiddags om 3.30 uur precies

door

Arthur Marinus Antonius Pistorius

geboren op 10 mei 1961
te Breda

Promotor: Prof. dr. J.J.H.H.M. de Pont
Co-promotor: Dr. W.J. de Grip

Manuscriptcommissie
Prof. dr. C.W. Hilbers
Prof. dr. W.W. de Jong (Universiteit van Amsterdam)

Stellingen, behorende bij het proefschrift:
"Biochemical Applications of FT-IR Spectroscopy"

1. Het verwijderen van de thio-palmitoylresten van rhodopsine, zoals voor-
   gesteld door Ganter et al., is af te raden, omdat dit resulteert in een
   niet correct functionerend foto-pigment.

   Ganter, U.M. et al. (1992) Photochem. Photobiol. 56, 57–62.

2. De vele onderzoekers die zich bezighouden met het simuleren van IR
   spectra, verkregen via Fourier zelf-deconvolutie, zouden eens reken-
   schap moeten afleggen van de door hen toegepaste bandbreedtes.

3. Met Tolkien kan over de methode voor voorspelling van de tertiaire
   structuur van eiwitten, uitgaande van de primaire structuur, gezegd
   worden dat iemand, die véél voorspelt, ook wel eens iets voorspelt
   dat uitkomt. Dat is echter geen verdienste van de gebruikte voor-
   spellingsmethode.

   Tolkien, J.R.R. "Sprookjes" (vertaald uit het Engels)
   De Grip, W.J. et al. (1993) in: Molecular mechanism of
   generation of electric signals in sensory cells (F. Tokunaga,
   ed.) The Taniguchi Foundation, Osaka, Japan, pp. 26–40.

4. In het visueel pigment van de octopus kan het tegen-ion van de gepro-
   toneerde Schiff base waarschijnlijk teruggevonden worden in het amino-
   terminale domein.

5. Luo et al. en Martin et al. hadden betere spectra -signaal/ruis ver-
   houding, basislijn artefacten- verkregen als ze hun accessoire voor foto-
   accoustische IR spectroscopie in de kast hadden gelaten.

   Luo, S. et al. (1994) Anal. Biochem. 216, 67–76.
   Martin, B. et al. (1990) Arch. Biochem. Biophys. 276,
   94–101.

6. De toelatingseisen voor het register van Europese Chemici doen onrecht
   aan de 'Laatsten der Oude-stijlers'.

7. Meer Nederlandse biochemici zouden een constructieve bijdrage moeten leveren door het beschikbaar stellen van onderzoeksgegevens aan het wereldwijde computernetwerk Internet, in plaats van alleen maar informatie uit dit net te consumeren.

8. Voor de puristen onder de Franse onderzoekers valt het te betreuren dat de voorgedrukte 'Request-A-Print' kaartjes nog steeds beginnen met: 'Dear collegue, ...'

9. Het voornemen om de contributie voor trim-hockeyers te verdubbelen, teneinde de kas van de Koninklijke Nederlandse Hockey Bond te spekken, moet nog eens zorgvuldig overwogen worden.

10. Bij de radiografische modelbouwsport staan de beste stuurlui altijd aan de wal.

Arthur Pistorius   25 september 1996.

Dankwoord

Op deze plaats wil ik een aantal mensen bedanken, die hebben bijgedragen aan de totstandkoming van dit proefschrift: promoveren doe je per slot van rekening niet alleen.

Petra, Jenny, bedankt voor de introductie in de biochemie en de hulp bij het ontleden van de vele koeie-ogen voor NMR en infrarood experimenten. Lieveke, Margriet, Peter en Frank, mijn kamergenoten van 2.15. We hoeven niet altijd op de zelfde golflengte te zitten en moleculaire biologie zal m'n vak toch wel niet worden: ik wil jullie graag bedanken voor de prettige sfeer binnen de werkgroep De Grip.

De samenwerking met collega's van andere vakgroepen in het Trigon en daarbuiten heb ik zeer op prijs gesteld. Patricia Groenen, Gieljan Bosman, Clemens Prinsen, Feico Schuurmans Stekhoven, Nico Sommerdijk, Henno van den Hooven, Bert Rietman, John van Duijnhoven en Wim Wolkers (Landbouw Universiteit Wageningen) wil ik hier graag noemen. Jullie belangstelling voor de mogelijkheden van de infrarood spectroscopie en het delen van interesse in biochemisch en organisch-chemisch onderzoek heb ik zeer gewaardeerd. Kregen we maar wat meer tijd om ècht wat van onze samenwerking te maken.

Professor Tesser en Hans Adams van de vakgroep Organische Chemie wil ik bedanken voor hun hulp bij de synthese van peptiden.

Een bijzondere ervaring was de kennismaking met electronenmicroscopische technieken op het laboratorium voor Experimentele Plantkunde (professor Mariani). Huub, bedankt voor je vakkundige hulp bij het gebruik van de apparatuur en assistentie in de doka.

Fysisch-chemisch onderzoek in een biochemische omgeving is heel verantwoordelijk werk. Hoe blijf je netjes omgaan met zoveel samengestelde pieken in een spectrum? Je kunt er wel van alles uithalen! Inspirerend en leerzaam op het gebied van data-behandeling en de analyse van infrarood

spectra waren dan ook de visites aan de groep van professor Van der Maas (sectie Analytische Molecuul Spectrometrie, Rijksuniversiteit Utrecht), waar Roel Ferwerda, Menno Kappers en Bert Lutz in belangrijke mate hebben bijgedragen aan het inzicht in deconvolutie-operaties en in de gebruiksmogelijkheden van Raman spectroscopie.

De staf en medewerkers van het CAOS/CAMM centrum en de afdeling C&CZ van de Faculteit der Natuurwetenschappen mogen ook niet onvermeld blijven. Niet alleen voor de hulp bij het oplossen van diverse computerproblemen en bij de praktische realisatie van dit proefschrift, maar ook voor mijn omscholing tot systeembeheerder.

Je moet vooral een goede conditie en uithoudingsvermogen hebben om een promotie te voltooien. Daarom is de donderdagavond gereserveerd voor de trimhockeyclub: daar komt geen ICS seminar tussen. Beste trimmers en trimsters, sstt, jullie belangstelling, aanmoedigingen en gezelligheid heb ik altijd zeer op prijs gesteld.

Tenslotte wil ik mijn ouders bedanken voor hun niet aflatende belangstelling voor een technisch nogal ingewikkeld onderzoek en voor het feit dat ze me in de gelegenheid hebben gesteld om te kunnen gaan studeren.

Lieve Myriam, je geduld is zwaar op de proef gesteld. Bedankt voor je steun!

Contents

ix

x

Abbreviations

ACTH	adrenocorticotrope hormone
ATR	attenuated total reflection
AU	absorbance units
cGMP	3',5'-cyclic guanosinemonophosphate
CD	circular dichroism (spectroscopy)
CHAPS(O)	cholamido propanesulfonate(N-oxide)
DOM	n-dodecyl-β-D-maltoside
DSC	differential scanning calorimetry
FITC	fluorescein isothiocyanate
FSD	Fourier self-deconvolution
FT-IR	Fourier transform infrared (spectroscopy)
FWHH	full width at half height
GMP, GDP, GTP	guanosine mono-, di-, tri phosphate
GPR	G-protein coupled receptor
IRE	internal reflection element
MCT	mercury cadmium telluride
Me$_2$SO	dimethyl sulphoxide
NCA	normal coordinate analysis
NG	n-nonyl-β-D-glucoside
NMR	nuclear magnetic resonance (spectroscopy)
opd	optical path difference
PAGE	polyacrylamide gel electrophoresis
PA(S)	photoacoustic (spectroscopy)
PC	phosphatidylcholine
pdb	Protein Data Bank
PE	phosphatidylethanolamine
PMSF	phenylmethylsulphonylfluoride
PS	phosphatidylserine

RIS, ROS	rod inner segment(s), rod outer segment(s)
SDS	sodium dodecyl sulphate
SNR	signal to noise ratio
TLC	thin layer chromatography

Chapter 1

An introduction to FT-IR spectroscopy

Including: Pistorius, A.M.A. (1995) *Spectrosc. Eur.* 7, 8–15.

1.1 Introduction

One of the most versatile analytical chemical techniques is infrared (IR) spectroscopy. Especially since the introduction of Fourier transform (FT) infrared spectroscopy, this technique is now increasingly used besides NMR spectroscopy for quantitative and qualitative analyses in many different fields of applications. Among these are the analysis of space and the earth's atmosphere, pharmaceuticals, (bio-)membranes and (bio-)polymers, paintings of the old masters and microbiological applications.

In this chapter, a short introduction on (FT-)IR spectroscopy is given. In paragraph 1.2, some IR basics are treated. In this paragraph also the difference between IR and Raman spectroscopy is pointed out, however, without discussing Raman instrumentation. Paragraph 1.3.1 offers an introduction to the technical aspects of FT-IR spectroscopy [119]. Although the information content of an IR spectrum, whether obtained from a dispersive or a FT-IR spectrometer is the same, using the latter offers certain advantages over dispersive instruments [120]. These advantages are briefly discussed in 1.3.2. The improved performance of IR spectrometers allows the use of alternative sampling techniques, and hence the analysis of less common or small or other 'difficult' samples.

Paragraph 1.3.3 is devoted to some of these (expensive) devices, which have contributed to the enormous increase in the use of IR spectroscopy [121].

In paragraph 1.4, factors which determine the appearance of an IR spectrum are discussed. These factors might be used to obtain more information from, often complex, spectra. Finally (paragraph 1.5) some methods are presented to analyse overlapping spectral features. This section is quite important, since this situation is encountered in practically all spectra of samples of biological origin.

1.2   Vibrational spectroscopy

In the spectrum of electromagnetic waves (Fig. 1.1), about 300 nm to the red, relative to the absorption maximum of the visual pigment rhodopsin (498 nm), the near infrared region (NIR; nearest to red light) begins, which is followed by the mid infrared (MIR; rather arbitrary between 2500 and 25000 nm) and the far infrared (beyond 25000 nm).
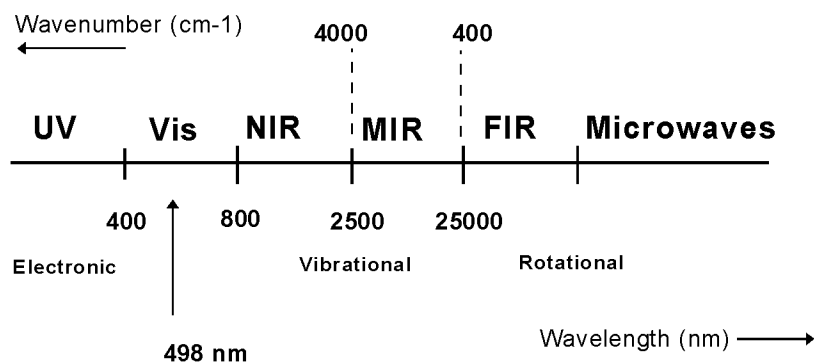
Figure 1.1: *Part of the electromagnetic spectrum. Wavelength and frequency axes are not scaled.*

It is common practice to express frequencies in this spectral region in wavenumbers, i.e. reciprocal wavelengths, or:

$$\tilde{\nu}(cm^{-1}) = \frac{1 \cdot 10^7}{\lambda(nm)} \qquad (1.1)$$

with the wavenumber, $\tilde{\nu}$, in cm^{-1}(or Kaiser) and the wavelength, λ , in nm. Thus the mid IR range, which in practice is the most important (see below), roughly lies between 4000 and 400 cm^{-1}.

Unlike UV-vis spectroscopy, which probes transitions between electronic states, IR and Raman spectroscopy are used to detect transitions between molecular rotational or vibrational energy levels [162, 20, 65]. The difference between these two types of vibrational spectroscopy is that IR spectroscopy detects vibrations, during which the electrical dipole moment changes, while Raman spectroscopy is based on the detection of vibrations, during which the electrical polarizability changes. The change in polarizability can be pictured by realizing that, owing to certain vibrations, the volume of the molecule is changed. This results in a change in the electron density of the molecule and hence, a different response to an electrical field is observed. A classical example is given by CO_2, a linear, non-polar molecule (Fig. 1.2).

Anti-symmetric

IR-active, Raman-inactive

Symmetric

IR-inactive, Raman-active
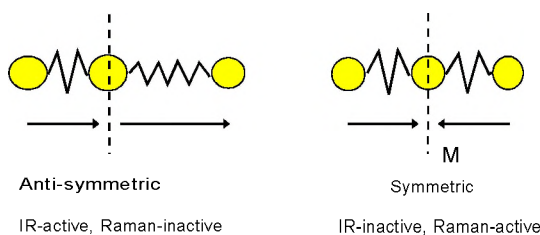
Figure 1.2: *Stretching vibrations in CO_2. The anti-symmetric stretching vibration results in a change in the dipole moment of the molecule and hence, is IR active. Due to the preserved symmetry (mirror plane, M, in the right figure) the dipole moment remains unchanged (zero) during the symmetric stretching vibration. Hence, this vibration is not observed in the IR spectrum of CO_2. The arrows indicate the direction of the movement of the oxygen atoms at a certain time-point, relative to the central carbon atom.*

Simultaneous stretching of both C=O bonds, (symmetric stretching vibration) does not result in a change of the dipole moment (which is zero) and will not result in a band in the IR spectrum, although for this vibration, a band in the Raman spectrum is observed (increase in molecular volume). Stretching of one C=O bond and simultaneously shortening of the other C=O bond (anti-symmetric stretching vibration) creates a dipole and hence, this vibration is IR active but will not show up in the Raman spectrum.

Most absorption bands, associated with stretching and bending vibrations in organic molecules, including materials from biological origin, occur at more or less discrete positions in the MIR range.

$\tilde{\nu}$ (cm^{-1})	Assignment	Mainly observed in:
$\pm$ 2900	ν_{as}(C-H) in CH$_2$	lipids
$\pm$ 2850	ν_{s}(C-H) in CH$_2$	lipids
$\pm$ 1740	ν(C=O) in esters	lipids
		overlap with ν(COOH)
		of Asp and Glu
$\pm$ 1650	ν (C=O) or amide I	proteins
		protein backbone conformation
$\pm$ 1540	δ(N-H) or amide II	protein backbone conformation
		overlap with ν(C=C) in Tyr
$\pm$ 1460	δ(C-H)	lipids
$\pm$ 1400	ν_{s}(COO$^-$)	protein: Asp, Glu
$\pm$ 1235	ν_{as}(PO$_2^-$)	phospholipids, nucleic acids
$\pm$ 1100	a.o. ν(C-OH)	carbohydrates

Table 1.1: *Some vibrational bands of biochemical importance. ν denotes a stretching vibration, δ , a bending vibration. The subscripts as and s refer to anti-symmetric and symmetric vibrations.*

Owing to the fact that the band pattern of the spectrum depends both on the sample composition and on the micro-environment of the molecules present, this spectral region can yield much information concerning molecular structure. Some bands which are of particular biochemical importance are the amide I and amide II vibrations between 1700 and 1500 cm^{-1}, representing the amide backbone of peptides and proteins, bands around 2900, 1740, 1400 and 1230 cm^{-1}, representing (phospho)lipids and several bands around 1100 and below 1000 cm^{-1} which can be attributed to carbohydrates or nucleic acids (table 1.1). The wide variety of bands resulting from polar functional groups, which can be observed in the MIR range makes IR spectroscopy the most important vibrational spectroscopic technique for studying bio-materials.

1.3 Technical aspects of IR spectroscopy

1.3.1 Instrumentation

An optical spectrometer basically consists of a broadband light source, a prism or a grid for dispersing the light, a slit for wavelength selection and a detector. The slit is passed slowly across the spectrum, generated by the dispersive element. Thereby, the sample is irradiated with light, continuously changing in wavelength, and the non-absorbed (i.e. transmitted) light is registered by the detector. In the case of IR spectroscopy, this meant for many years that it took 12 minutes to acquire a spectrum from 4000 to 400 cm^{-1} with rather moderate signal to noise ratio and low resolution, during most of which time the detector was registering noise. The developement of Fourier transform IR (FT-IR) spectroscopy has changed this picture drastically, and nowadays, IR spectroscopy again is recognized as an invaluable counterpart to pulse Fourier transform NMR spectroscopy for the analysis of molecular structure [164].

The most important feature of a FT-IR spectrometer is that detection of all frequencies is performed simultaneously, instead of one by one, as is the case in the dispersive set-up. Frequency selection of the absorbed radiation is performed afterwards, by means of the Fourier transformation. This concept was realized by Fellgett [39], who put to use the principles of the famous Michelson interferometer for IR spectrometry [146] (Fig. 1.3).

The operation of this instrument is most easily explained by considering monochromatic light, which is passed through a beamsplitter: a semi-transparent and semi-reflecting optical element. The resulting beams are directed to a stationary mirror (M1) and a moving mirror (M2) and, subsequently, backreflected to the beamsplitter. Here the beams recombine, i.e. interfere: depending on the pathlength difference between a and b (Fig. 1.3), the beams enhance or extinguish each other. Constructive interference occurs if the pathlength difference (opd or δ) equals an integer multiple of the radiation wavelength:

$$\delta = n \cdot \lambda \qquad n = 0, 1, 2, ... \qquad (1.2)$$

and destructive interference occurs if the pathlength difference equals an odd multiple of the half wavelength:

$$\delta = (n + \frac{1}{2}) \cdot \lambda \qquad n = 0, 1, 2, ... \qquad (1.3)$$
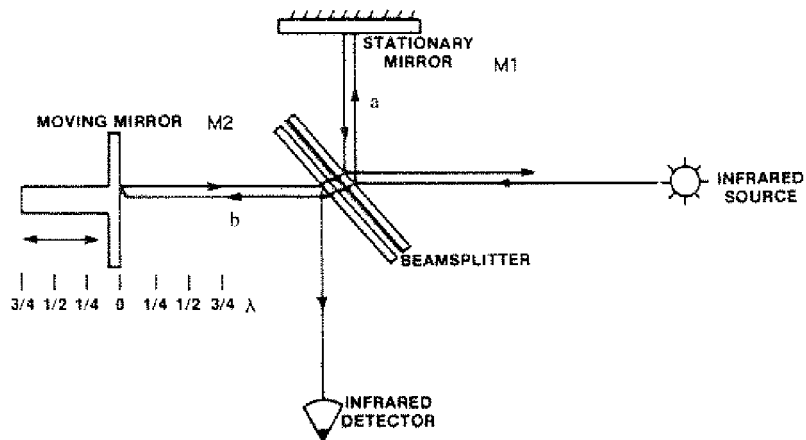
Figure 1.3: *Optical layout of a Michelson interferometer. Radiation from the source is split and directed to a fixed mirror (M1) and a mirror, moving along the optical axis (M2). After backreflection, the beams recombine at the beamsplitter and the resultant is reflected to the infrared detector. The sample is placed in the final path from beamsplitter to detector.*

The pathlength difference is created by moving M2 forward and backward along the optical axis with a typical speed of about 1 cm/s and a stroke of about 1 cm and equals twice the mirror displacement. Owing to this periodic movement, a cosine modulated signal or interferogram is observed at the IR detector (Fig. 1.4). The detected signal thus depends on the position of the moving mirror. This information is digitized and stored in the memory of a computer. The Fourier transformation [54] of the interferogram is defined by:

$$E(\tilde{\nu}) = \int_{-\infty}^{\infty} I(\delta) \cdot e^{i\tilde{\nu}\delta} d\delta \qquad (1.4)$$

and produces the frequency spectrum, which for trace A in figure 1.4 contains a single line at 500.0 cm^{-1} (not shown). In other words, the Fourier transformation results in a conversion of a distance-dependent signal (the $I(\delta)$) to a frequency-dependent signal, expressed in reciprocal distance units (the IR spectrum or $E(\tilde{\nu})$).

Since the stroke of the moving mirror and the computer storage space are limited, the transforming integral is limited by applying an apodization operation, i.e., the integral is only calculated over the stroke of the moving
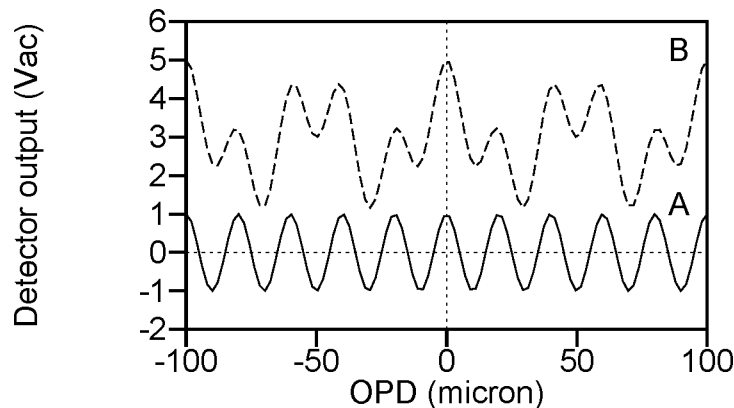
Figure 1.4: *Interferogram of a monochromatic source with a wavelength of 20 μm (trace A) and an interferogram of two monochromatic sources with wavelengths 20 and 50 μm respectively (trace B). The optical path difference (OPD) equals twice the mirror displacement. Trace B is offset for clarity.*

mirror (M2), instead of an infinite pathlength difference. As a result, the signal to noise ratio is somewhat increased at the expense of a reduction in resolution. The numerical evaluation of the transforming integral is performed by using the so-called fast Fourier transformation (FFT) algorithm, developed by Cooley and Tuckey [21].

The same principle applies to a broadband source, emitting many frequencies. In this case an interferogram, consisting of superimposed cosine waves is observed (Fig. 1.5, trace A). The emission or single beam spectrum (Fig. 1.6, trace A) of this 'source-only interferogram', obtained after Fourier transformation, shows a background spectrum (i.e. no sample in the beam), which may be considered as the instrument's signature since it is determined by the source, beamsplitter (KBr), detector characteristics (in this case a narrow band MCT detector) and the sample chamber's atmosphere (water vapour, carbon dioxide). If we now put a sample in the beam, the interferogram does not seem to be very much changed (Fig. 1.5, trace B).

However, Fourier transformation now yields the sample single beam spectrum (Fig. 1.6, trace B), in which the sample characteristics (a polystyrene film) are superimposed on the background. The familiar transmittance spectrum can be calculated by ratioing the sample single beam spectrum against the background single beam spectrum (Fig. 1.7). For analytical purposes,
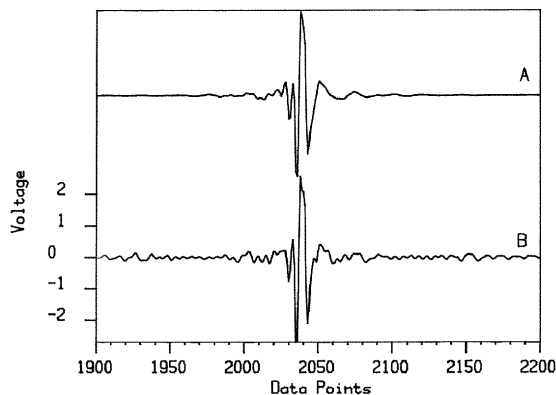
Figure 1.5: *Expanded interferograms derived from a broadband IR source. Trace A, interferogram without a sample in the beam; trace B, interferogram of a polystyrene film.   The full spectrum is composed of 4064 datapoints, evenly divided over an opd of 0.25 cm.*
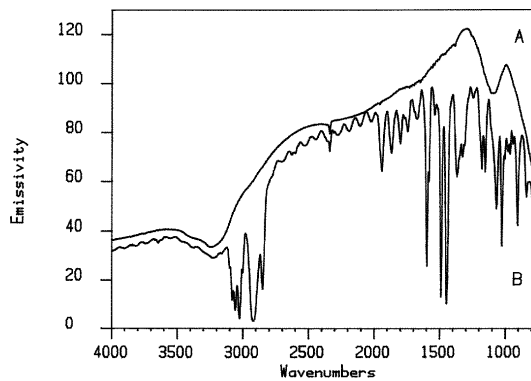
Figure 1.6: *Single beam FT-IR spectra. Trace A, Background spectrum, obtained after Fourier transformation of the interferogram A in Fig. 1.5; trace B, single beam spectrum of a polystyrene film, obtained after Fourier transformation of interferogram B in Fig. 1.5.*
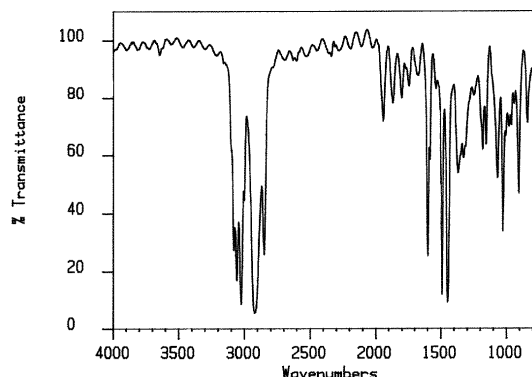
Figure 1.7: *Transmittance spectrum of a polystyrene film. This 'double beam' spectrum is obtained by ratioing the traces A and B of Fig. 1.6, according to:* $\%T = E_{sample}/E_{background} \cdot 100\%$

the absorbance spectrum can be calculated from the transmittance spectrum $(A(\nu) = -\log(T(\nu)\,))$.

1.3.2 Fourier transform versus dispersive IR spectroscopy

The superior performance of FT-IR instruments over dispersive instruments is basically due to a few very important features of the interferometer [120]. These are known as

1. the multiplex or Fellgett advantage

2. the wavenumber accuracy or Connes advantage.

Often, the energy throughput or Jacquinot advantage is also mentioned. However, this advantage is relatively small and treatment of this feature may rapidly become confusing. Therefore it is not considered in this thesis.

The multiplex advantage reflects the fact that all frequencies in the FT-IR spectrum are measured together in one stroke of the moving mirror and that each acquired datapoint contains information about all frequencies. This means that, in principle, using a moving mirror velocity of 1 cm/s, a complete spectrum with a resolution of 1 cm^{-1} can be obtained in 1 second

(neglecting the time needed for demultiplexing, i.e. Fourier transformation), which is a considerable reduction in acquisition time. Otherwise stated, if a FT-IR instrument is allowed to accumulate and average a few hundred spectra in the same time required for the acquisition of a spectrum on a dispersive instrument, a spectrum with an exceptionally high signal to noise ratio can be obtained. Alternatively, the short acquisition time enables to perform time-resolved experiments. Typical applications of this type of experiments can be found in photoreceptor research [136]. The time resolution can even be improved by employing an instrument with a dedicated step-scan interferometer [154].

The enhanced wavenumber accuracy (better than 0.1 cm^{-1}) which can be achieved with a FT-IR instrument is the result of the very precise sampling of the interferogram. This sampling process is triggered by the interferogram of a red HeNe laser ($\lambda = 632.8$ nm or $\tilde{\nu} = 15802.78$ cm^{-1}). As mentioned before, the interferogram of a monochromatic source (i.e. laser) is a cosine. This independent laser signal is generated with the IR interferometer optics. The zero-crossings of this signal are counted electronically and the IR interferogram is typically sampled every second zero-crossing (Fig. 1.8).
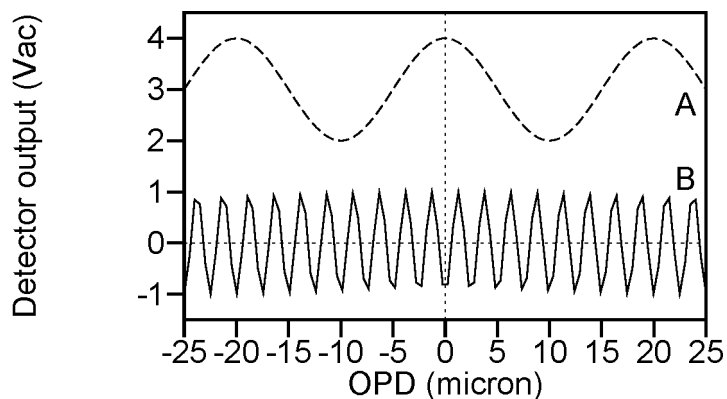
Figure 1.8: *Sampling an interferogram (trace A), using a laser reference signal (trace B). After each second zero-crossing of the laser interferogram, the IR signal is measured by the analog to digital converter.*

The choice of a red laser meets the so-called Nyquist criterion, which states that the highest frequency component present in the spectrum, must be sampled twice in order to obtain an accurate measurement. Thus, frequencies

below 4000 cm^{-1} are always oversampled, which leads to highly reproducible and accurate IR spectra. In the case of laser quadrature detection, two laser reference signals with a phase difference of 90° are generated. Comparison of both signals not only yields the optical path difference but also whether the moving mirror is travelling forward or backward. This technique enables the optimal use of the maximum stroke of the moving mirror, i.e. one can obtain a higher spectral resolution by recording asymmetrical interferograms or one can obtain twice as many interferograms by acquisition of interferograms in both mirror travelling directions [1].

1.3.3 Sampling techniques

The distinguished features of FT-IR spectrometers (high signal to noise ratio, acquisition speed, high accuracy) allow the analysis of samples which could not easily studied before, e.g. aqueous solutions, surface coatings or dark-coloured solids. Companies manufacturing FT-IR instrumentation have also stimulated this developement by offering a wide range of expensive sampling accessories, which further aid in the analysis of 'difficult' samples. In this paragraph, a few infrared sampling techniques, which are relevant for bio-chemical samples, are briefly discussed [121]. Micro-sampling, IR imaging and combined techniques, such as GC-IR, HPLC-IR or MS-IR are outside the scope of this thesis.

The most common IR-analytical apporach is the transmission mode. This technique however, already imposes practical problems, since biochemical processes occur in an aqueous environment. Unfortunately, the strong IR-absorption bands of water interfere badly, especially around 1650 cm^{-1}, which is inside the range where important structural information on proteins can be obtained. In order to minimize the absorbance by the solvent, one must use high sample concentrations, a short-pathlength cell (less than 0.01 mm) which is difficult to handle, and afterwards perform spectral subtraction of the solvent. Recently, mixtures of water with organic solvents (e.g. 1,1,1-trifluoroethanol or Me$_2$SO) have been examined as solvent for biochemical samples [70, 69]. By applying this method, a cell with a more normal path-length (0.025-0.050 mm) can be used and solvent subtraction is more reliable. Thus, protein secondary structure can be analyzed but owing to the physical

---

[1]Owing to slight differences in the forward and backward scans, this option has never been implemented.

properties of these solvents (dielectric constant, dipole moment), the possibility exists that the structure of the protein has been changed by the solvent, e.g. conversion of β to α-type secondary structure [70]. Detailed functional studies are more difficult, since the spectral artifacts, associated with solvent subtraction are shifted to lower wavenumbers and many biochemical reactions are strongly influenced by such conditions.

Alternatively to H_2O, ^2H_2O may be used. However, owing to isotope exchange, bands may shift and kinetic parameters, e.g. protein denaturation, also will be influenced by the isotope effect. Mixtures of H_2O with ^2H_2O as used in the deuterium dilution technique (Ddt) [173], although somewhat more elaborate, are expected to give better results.

Transmission spectra of biomembranes are most conveniently obtained by depositing these samples as a thin film on IR-transparent, water resistant AgCl windows, e.g. using the iso-potential spin drying method [18]. Prior to analysis, these samples can be fully rehydrated with a small amount of water or any buffer solution, still yielding useful IR spectra. The spin drying method appears also to be applicable to water-soluble proteins (this thesis, chapter 4). Estimates of the secondary structure from the amide I and amide II bands in IR spectra of such dehydrated proteins are in good agreement with estimates from IR measurements in solution or from crystallographic or NMR data.

A sampling technique, which is gaining in importance the last few years is reflection IR spectroscopy. Basically, there are 3 ways to generate an IR spectrum from reflected IR light viz. through specular, diffuse or attenuated total reflection (ATR) (Fig. 1.9). The nature of the sample largely determines the usefulness of the method, e.g. smooth surfaces can be analyzed using specular reflection, and powdered solids or reactions of gasses at catalytical surfaces can be studied relatively easy by diffuse reflectance spectroscopy (DRIFT). Attenuated total reflection spectroscopy however, is the most promising technique for analyzing liquids or biochemical samples in an aqueous environment. In an ATR experiment, the sample (typically a liquid, paste or film) is brought into close contact with a trapezoid, IR-transparent crystal or internal reflection element (IRE) and IR radiation is passed through the latter with an angle of incidence, defined by the geometry of the crystal. At the IRE-sample interface, depending on the refractive indices of sample and IRE, IR radiation partially penetrates into the sample (evanescent wave). The back-reflected light beam is attenuated, owing to absorption by the sample, and finally reaches the detector [12, 41]. Using
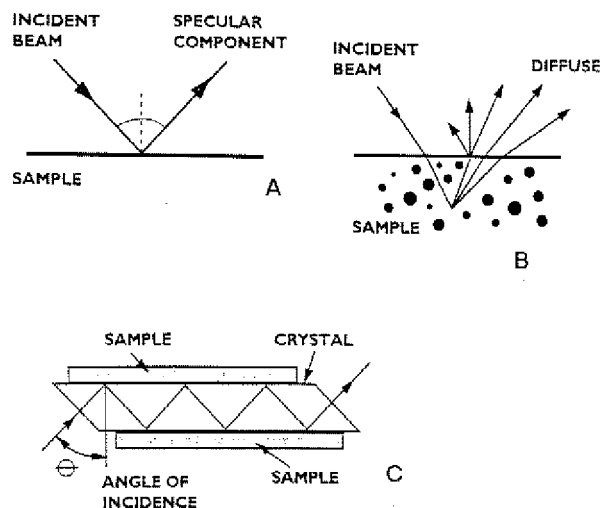
Figure 1.9: *Methods using reflected IR light. A, Specular reflection. The angle of incident light equals the angle of reflected light; B, diffuse reflectance. Incident radiation diffuses within the sample and is reflected under several angles; C, Attenuated total reflection. Incident radiation reflects within the crystal or IRE and partially penetrates the sample. The back-reflected beam is attenuated due to absorption by the sample.*

this technique, effective pathlengths of some micrometers at the most are obtained and this facilitates the analysis of aqueous samples. It should be noted, however, that the penetration depth is also a function of the radiation wavelength. Hence, the obtained spectra do not fully resemble true absorbance or transmittance spectra (Fig. 1.10 and 1.11). Since, in principle, the relation between the the effective pathlength and IR wavelength relation is known, a wavelength-dependent scaling factor may be introduced.

ATR-IR spectroscopy is especially useful for biomembrane research (i.e. membrane structure and dynamics: lipid phase transitions, protein-lipid interactions and orientation studies) [29, 40, 157]. The most rewarding experiments in this field are those, in which the sample can be immobilized on the surface of the IRE. Under this condition, the liquid environment (pH, buffer components, addition of co-factors) can be altered and the spectral response of the sample can be monitored, without major spectral distortion by water absorption [6].
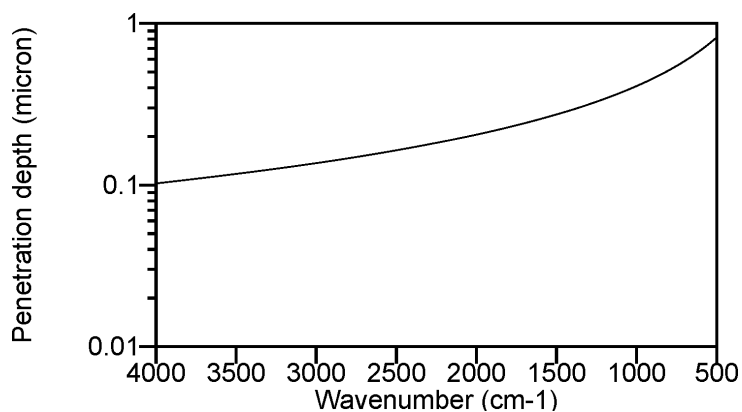
Figure 1.10: *Penetration depth versus infrared frequency. Employing a germanium IRE with an angle of incidence, Θ of $45°$, this relation can be approximated by: $d_p(\mu m) = 0.41 \times 10^3/\tilde{\nu}\,(cm^{-1})$*

ATR spectroscopy also finds its use for studying the secondary structure of proteins, and, when the sample can be properly oriented, for analysis of the relative orientation of specific components.
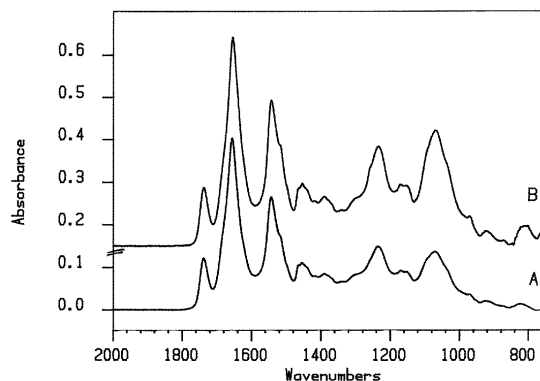
Figure 1.11: *Comparison of an absorption spectrum and an ATR-IR spectrum of bovine photoreceptor membranes. Trace A, absorption spectrum; trace B, ATR-IR spectrum. The ATR spectrum is scaled using the band around 1740 cm^{-1} as a reference. The bands below this position appear relatively stronger in the ATR spectrum (longer wavelenghts). This is most clearly seen at the phosphate band around 1237 cm^{-1} and the broad band around 1100 cm^{-1}.*

One of the less common techniques for the detection of IR absorbance bands is to utilize the photo-accoustic effect [64]. Since no special sample preparation is required, this expensive sampling and detector device is particularly suited for solid samples (Fig. 1.12).
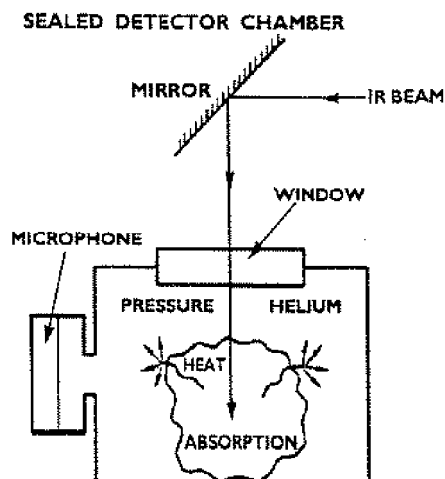
Figure 1.12: *Combined sampling and detector accessory for photo-accoustic IR spectroscopy (PAS)*.

The sample is put into a sample chamber which is purged and filled with an inert detecting gas (helium) and subsequently sealed. The infrared beam, modulated by the interferometer, is partially absorbed by the sample and this causes the sample to heat up and expand slightly. The resulting modulated vibration of the sample is taken over by the detecting gas, thereby generating a faint audiofrequent signal, which is detected by the microphone. Owing to the low signal to noise characteristics of the detector and the quenching of the signal by water (vapor) this technique is less suitable for biochemical IR applications. Nevertheless, some papers have appeared, in which PAS is described for use in biochemical investigations [90, 130, 91].

1.4 Analysis of IR spectra

1.4.1 Peak assignment strategies

IR spectra of bio-macromolecules consist of many bands which, in principle, contain information about structural aspects of the molecule under study.

In order to retrieve this information, the observed spectral bands have to be assigned to distinct components of the molecule or supramolecular structure [12]. In many cases, comparison with IR spectra of analogues or smaller model compounds is neccessary to unequivocally assign the spectral features. In addition, enzymatic methods give the opportunity to make selective modifications, which certainly will give rise to changes in the IR spectrum, e.g. proteolysis, oxidation/reduction, phosphorylation, isomerization or conjugation. A more sophisticated method of protein modification is site-directed mutagenesis, either by molecular biological techniques or by (semi-)synthesis. Although these techniques are very time consuming, relative to the acquisition and analysis of FT-IR spectra, the combined efforts may result in a detailed knowledge of structure-function relationships within the protein under study.

The most fundamental way however, to identify absorption bands in an IR spectrum is to make use of non-radioactive isotope substitution. The vibration, exerted by 2 atoms may be approximated by a harmonic oscillator. According to the classical mechanics, the vibrational frequency is:

$$\nu = \frac{1}{2\pi}\sqrt{\frac{k}{\mu}} \tag{1.5}$$

with k a force constant, determined by the chemical bond strength and μ the reduced mass of the 2 atoms ($\mu = m_1 \cdot m_2/(m_1 + m_2)$). Assuming that the bond strength, which is an electronic property, does not change, converting a C-^{1}H bond into a C-^{2}H bond results in a C-^{2}H stretching vibration with a frequency which is 1.37 times lower than the $\tilde{\nu}(C -^1 H)$ frequency.

An example of isotope labeling by solvent exchange is the estimation of the secondary structure of proteins in aqueous solution. By dissolving the protein in ^2H_2O, the amide hydrogen atoms are exchanged by deuterium atoms. This results in a decrease in the corresponding amide I and amide II frequencies, except for β-sheets, which are 'protected' by internal hydrogen bonds, and the less accessible transmembrane α-helices. Other substitutions e.g. ^{12}C to ^{13}C, ^{14}N to ^{15}N or ^{16}O to ^{18}O show less dramatical but equally useful frequency shifts, which allow the IR-spectroscopist to utilize all spectral components.

1.4.2 Environmental effects

Another way to study biochemical systems using IR spectroscopy is to look at the spectral response to changes in the environment, e.g. pH, temperature, influence of light or solvent. The use of a polarized IR measuring beam also belongs to this category. Since the effects of these factors are predictable, the observed spectral changes may be correlated to certain components of the system. Some examples of applications may illustrate which type of information can be obtained from these experiments.

By lowering the temperature the photolytic cascade of rhodopsin can be blocked at a very early intermediate: bathorhodopsin. Analysis of the bathorhodopsin minus rhodopsin IR difference spectrum, obtained after illumination, reveals that at this stage, the major changes changes have occurred in the bands originating from the chromophore. These changes can be interpreted in terms of the photo-isomerization of the 11-*cis* to a strained *all-trans* isomer. In these studies, isotopically labeled retinal analogues were used to confirm the assignment of the chromophore vibrational bands, as mentioned in the previous paragraph [28].

IR spectra of membrane samples, measured as a function of temperature, show shifts of bands, associated with the phospholipids (C-H stretching and bending vibrations, C=O stretching in ester bonds, phosphate diester stretching modes). These experiments give, complementary to DSC, information about (phospho)lipid phase transitions (Fig. 1.13). IR spectroscopy however, has the advantage that, in addition to the transition temperature, information is obtained about other conformational changes or specific interactions, e.g. with the lipid headgroups or (unsaturated) acyl chains (this thesis chapter 5).

By using linearly polarized IR light, the observed absorption is a function of the orientation of the sample relative to the incident beam. If the vibrational transition moment, a vector which lies parallel to the dipole moment of an oscillating dipole, is oriented parallel to the electrical vector of the incident, polarized light, maximum absorption occurs. A minimum is obtained if the transition moment is oriented perpendicularly to this electrical vector, i.e. parallel to the direction of propagation of the polarized light. This phenomenon can be used e.g. to determine the orientation of lipid fatty acid acyl chains or of membrane spanning protein fragments, assuming an α-helical geometry or, alternatively, to assign certain spectral components. A typical example of this application is given by Earnest et al. [35], who
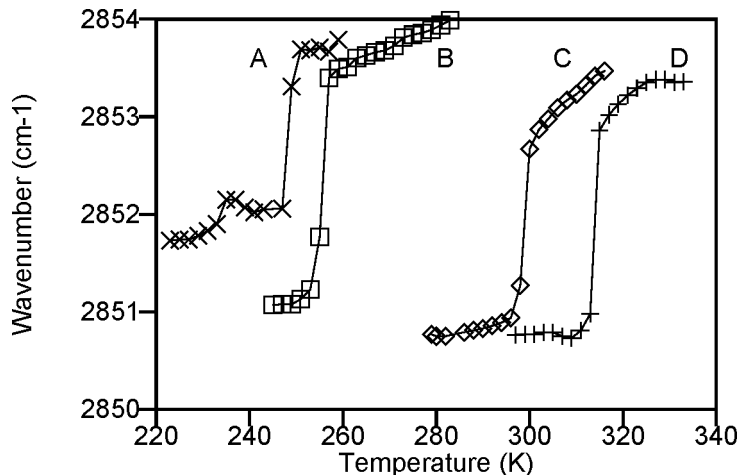
Figure 1.13: *Typical temperature dependencies of the absorbance maximum of $\nu_s(C-H)$ in liposomes of selected phospholipids. The discontinuities represent the gel to liquid crystalline phase transition. A,16:1,16:1-PC; B, 18:1,18:1-PC; C, 14:0,14:0-PC and D, 16:0,16:0-PC.*

showed, by analyzing the IR linear dichroism of the amide I bands around 1639 cm^{-1}, that the membrane spanning domains of bacteriorhodopsin do not contain β-type structure. Also, measuring the dichroic ratio $(A_{\parallel}/A_{\perp})$ is a way to discern antisymmetric and symmetric vibrations, e.g. in CH_2, PO_2^- groups, or imides and anhydrides.

1.5   Analysis of overlapping bands

An IR spectrum of a non-cyclic and non-linear molecule, containing a total number of N atoms, theoretically consists of 3N-6 spectral bands. These bands represent the vibrational degrees of freedom in this molecule. For example, the IR spectrum of glycine, the simplest amino acid, contains 24 bands and for a spectrum of a typical phospholipid this number becomes about 400. Not all these modes are separately observed in the spectrum but it is obvious that in spectra of biomacromolecules, overlap of bands seriously impairs the analysis and interpretation of the spectrum. The number of bands which can be distinguished in the spectrum is limited by the bandwidths of the spectral components and by the optical resolution of the spectrometer.

In order to reduce this problem, several mathematical techniques have been developed to separate overlapping bands, being:

- derivative spectroscopy

- Fourier self-deconvolution (FSD)

- curve fitting

Derivatization as well as FSD transform the absorption bands to lineshapes with a narrower width, thereby resolving overlapping components. Often, these methods are referred to as resolution enhancement techniques, but one has to keep in mind that only graphical resolution (i.e. the appearance of the spectrum) is improved; the actual optical resolution is still determined by the spectrometer settings, or more precisely, by the maximum stroke of the moving mirror.

Curve fitting is the process of regenerating a measured spectrum by mathematically adding a pre-defined number of bands with known peak positions, bandwidths and lineshape functions. Subsequently, these parameters are iterated until the theoretically generated spectrum and the measured spectrum coincide to a high degree. Since these methods will be routinely used throughout this thesis, a short description and typical applications of these methods in IR spectroscopy are presented in the following paragraphs.

1.5.1 Derivative spectroscopy

Mathematically, derivatization is a relatively simple procedure to determine absorption maxima of overlapping bands. Assuming Lorentzian band profiles, the first derivative has a zero-crossing at the band center, where the second derivative has a negative maximum.

The second derivative which, in practice is the most important, is further characterized by two zero-crossings and has a bandwidth which is 2.7 times smaller than the halfwidth of the original band [77]. This process is illustrated in figure 1.14. Trace A shows a simulated spectrum, consisting of 3 Lorentzian bandshapes at 1650 (FWHH=10 cm^{-1}, peakheight=0.25 AU), 1600 (FWHH=20 cm^{-1}, peakheight=0.25 AU) and 1550 cm^{-1}(FWHH=40, peakheight=0.25 AU). Trace B shows the first derivative of A with zero crossings at 1650, 1600 and 1550 cm^{-1}, and a decreasing peak-to-peak height with a concommitantly increasing bandwidth.

The second derivative (trace C) yields narrower bands with negative peak maxima. It is clear that in the second derivative, the peakheight also is cor-
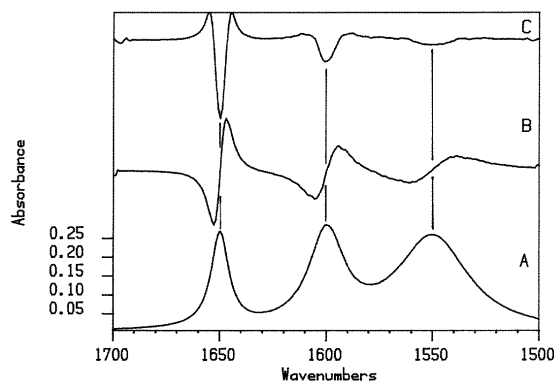
Figure 1.14: *Derivative spectroscopy for determination of peak positions. A, synthetic absorption spectrum, consisting of 3 bands with varying linewidths (FWHH is 10, 20 and 40 cm^{-1} respectively); B, first derivative of A, showing zero-crossings at absorbance maxima; C, second derivative of A, smoothed over 13 datapoints. The derivative exhibits negative maxima at the peak positions in the absorption spectrum.*

related with the original bandwidth and that broad bands will easily escape detection. Thus, the second derivative consists of negated and narrowed bandshapes, compared to the absorption spectrum.

Derivatization, however, strongly enhances noise and other sharp bands as well, such as water vapour bands, since narrow bands yield very steep derivative signals. To compensate for the increase in noise, a smoothing procedure is usually applied [142, 77]. Spectral distortion by water vapour peaks is circumvented best by performing acquisition of the IR spectra with an instrument, purged with very dry air or nitrogen gas, thereby obviating the need for spectral subtraction of the water vapour bands, which may introduce additional artifacts.

Another, fortuitous, effect of derivatization is its 'baseline correcting' ability. This is due to the fact that the derivative of a sloping baseline changes only little relative to the other bands in the spectrum. Hence, the baseline in the second derivative spectrum always runs flat at zero absorbance units.

1.5.2 Fourier self-deconvolution

One of the most useful as well as most abused methods for analyzing overlapping bands in IR spectra is deconvolution (FSD). This versatile method is applied in many other scientific fields, including pharmacodynamics, electronics, psychology and meteorology, and was adapted by Kauppinen et al. [76, 77] for IR spectroscopy.

Deconvolution can be regarded rather literally as a filtering operation: depending on the input parameters, one can smooth or enhance the characteristics of selected bands (resolution enhancement), e.g. just as the bass and treble of a HiFi stereo set are adjusted. Other applications are baseline correction and lineshape transformations (e.g. Lorentzian to Gaussian). The reverse operation, i.e. convolution, is applied every time when, prior to Fourier transformation, a measured interferogram is apodized with, by example, a triangular function.

Many reviews have already appeared on this subject but since it appears that FSD can easily be misused and that the results even depend on the make of deconvolution software, a short introduction on the deconvolution procedure and the parameters involved seems to be justified. The examples in this section are generated by making use of the Mattson EXPERT-IR analytical software [2].

The convolution operation is defined by:

$$f(x) * g(x) = \int_{-\infty}^{\infty} f(l) \cdot g(x - l) dl \qquad (1.6)$$

where $*$ denotes the convolution of $f(x)$ and $g(x)$. Obviously, this definition is difficult to use in practical cases. The convolution theorem, however, states that:

$$\mathbf{FT}\{f(x) * g(x)\} = F(\nu) \cdot G(\nu) \qquad (1.7)$$

where $f(x)$, $F(\nu)$ and $g(x)$, $G(\nu)$ are Fourier pairs according to: $\mathbf{FT}\{f(x)\} = F(\nu)$ and $\mathbf{FT}\{g(x)\} = G(\nu)$ or, in other words, Fourier transformation of a convolution of two functions is equal to the product of the corresponding transformed functions in the co-domain.

---

[2]The EXPERT-IR suite is not without flaws. The area under an absorption band should equal the area under its deconvoluted profile. In order to keep a constant integral after band narrowing, the peak height has to be increased. However, a decreased peak height is found instead.

Deconvolution is the reverse operation, i.e. we want to know $F(\nu)$, which is deconvoluted from the real, measured (FT-IR) spectrum $F(\nu)*G(\nu)$. Since f, F and g, G are Fourier pairs respectively, the convolution theorem can be rewritten to:

$$f(x) \cdot g(x) = \mathbf{FT^{-1}}\{F(\nu) * G(\nu)\} \tag{1.8}$$

The interferogram of the deconvoluted spectrum can be obtained by:

$$f(x) = \frac{\mathbf{FT^{-1}}\{F(\nu) * G(\nu)\}}{g(x)} = \frac{1}{g(x)} \cdot I(x) \tag{1.9}$$

with $I(x)$ the reverse Fourier transformation of the measured spectrum and $g(x) = \mathbf{FT^{-1}}\{G(\nu)\}$ represents a function which, itself, is convolution of the original apodization function (triangular) and a lineshape function (approximately Lorentzian). The deconvoluted spectrum can be obtained simply, by Fourier transformation of $f(x)$. Depending on the application, a combination of a new apodization function and a lineshape function must be defined. This will be illustrated in a few examples.

Deconvolution is most frequently used to resolve overlapping bands. For this application the lineshape function should approximate the real lineshape, in most cases being an unknown convolution of Lorentzian and Gaussian functions. Subsequently, the linewidth of the lineshape function and the desired linewidth in the resulting deconvoluted spectrum must be defined which, of course, cannot be less than the instrumental resolution. For this purpose, the K-factor is introduced. The K-factor determines the multiple by which the bandwidth of the previously determined lineshape function is decreased if such a band occurs in the measured spectrum. A K-value between 0 and 1 results in a smoothed spectrum and a K-value larger than 1 results in a spectrum with an enhanced band separation, relative to the measured spectrum. The additional second apodization function which is required in the deconvolution operation appears to be not very critical for this application, but it should be noted that application of a quadratic apodization function during deconvolution results, according to the derivative theorem, in a second derivative spectrum [77]. A second derivative spectrum however, can be obtained more easily using another algorithm [142].

The following figures show the effect of the selected linewidth and K-factor on the appearance of the deconvoluted spectra, starting with a synthetic spectrum, consisting of 3 bands with linewidths of 10, 20 and 40 cm^{-1}. Choosing a narrow bandwidth results in a little better band separation, which cannot

be compensated for by increasing K. This only results in an increase of the noise (Fig. 1.15 left panel). Choosing an intermediate bandwidth gives a better band separation but it also results in spectral distortion of narrower components (Fig. 1.15 right panel). This is especially true when selecting an even broader bandwidth. In this case a good separation of broad spectral components can be obtained but the side lobes on the narrower components can easily be misinterpreted as 'real' (Fig. 1.16).
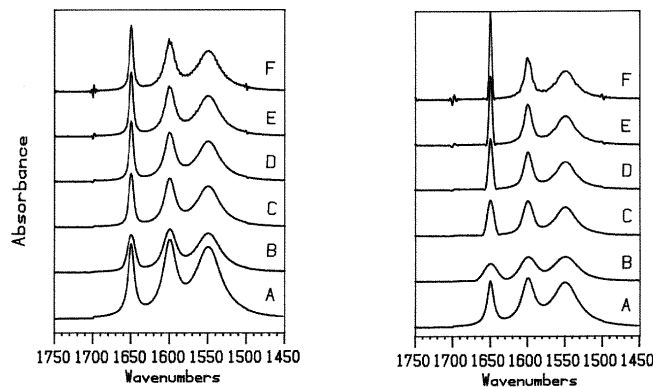
Figure 1.15: *Deconvolution of a synthetic spectrum. Left panel: Input bandwidth is 10* cm⁻¹. *A. Original spectrum; B, K=0.5. A smoothed spectrum is obtained; C, K=1.0. No smoothing or narrowing; D, K=1.5; E, K=2.0; F, K=2.5. Only higher K-factors result in band narrowing, but mainly of the narrow band. Right panel: Same spectrum as in left panel but the input bandwidth is now 20* cm⁻¹.

The deconvolution operation can also used for 'smoothing' a spectrum, which suffers from fringing. These fringes normally originate from a transient voltage change in the main power supply of the spectrometer or by internal reflection of the IR beam in a sample (e.g. see Fig. 1.7). In these cases, a spike will occur in the interferogram which, after Fourier transformation, results in a cosine wave across the full spectrum. In case that the interferogram is not available anymore for correction of this artifact (so-called 'interferogram editing'), deconvolution can sufficiently remove the fringes without distortion of the absorption bands, using a K-factor of 1.00 (no smoothing), a Bessel or a cosine apodization function and a bandwidth defined by the distance between the fringes (Fig. 1.17).
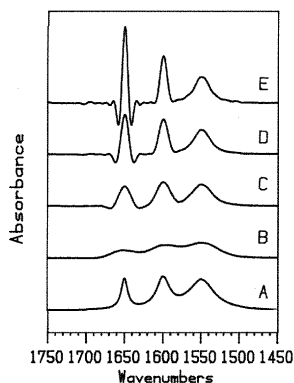
Figure 1.16: *Same spectrum as in figure 1.15 but the input bandwidth is now 40* cm^{-1}. *Obviously, higher K-factors result in severe spectral distortion of narrow bands. Therefore, trace F is omitted.*
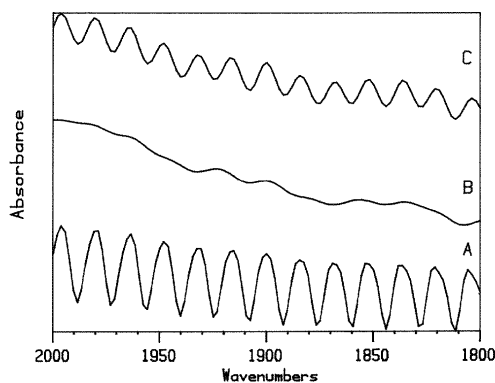
Figure 1.17: *Application of FSD for removal of fringes from a FT-IR spectrum. A, expanded part of a spectrum of a shining and reflecting AgCl window; B, deconvoluted spectrum from A, using the distance between the fringes as the bandwidth, a K-factor of 1.00, a Lorentzian lineshape and a cosine apodization function (A Bessel function performs equally well); C, same as trace B, but using a* sin$^2(x)/x^2$ *apodization.*

1.5.3   Curve fitting

Curve fitting is the procedure by which a spectral feature is simulated, based on theoretical assumptions. The input parameters for the simulation are changed until the simulated profile matches the measured profile. The parameters which generate the 'best fit' are used to describe the measured profile in a more quantitative way, e.g. the area under 2 bands representing the relative concentrations of components in a mixture.

In biochemical IR spectroscopic applications, this method especially finds its use in the analysis of amide I band profiles of proteins [151, 152]. Due to different hydrogen bonding patterns in secondary structural elements, this band consists of several components, representing the relative amount of e.g. α-helical or β-type secondary structure present.

The amide I components in the spectrum of a protein with an unknown secondary structure can also be related to the amide I components of a set of reference spectra, originating from proteins with a known secondary or tertiary structure. This is the basis of the multi-component quantitative analysis or pattern recognition method, which relies on the partially least squares (PLS) procedure for resolving the relative contributions of α-helical, β-type or turn structures [139, 85]. Although this is an elegant method, requiring no elaborate and time consuming curve fitting procedures, the applicability is restricted owing to the, contrary to popular belief, still inadequately understood relationship between the amide bands in an IR spectrum and the secondary structure of a protein.

The pioneering work of Miyazawa [99], Krimm and Bandekar [7], who carried out normal coordinate analysis (NCA) on model peptides and proteins, has produced a more theoretical basis for a correlation between the number and approximate positions of the amide I components and the secondary structure of a protein. Treatment of NCA, however, which involves time-dependent perturbation calculations, is beyond the scope of this thesis.

Performing curve fitting analysis requires that the number of bands and, preferably, the peak positions are known beforehand. Also an initial guess of the input bandwidths and lineshapes has to be made [156]. Therefore, curve fitting is usually carried out on deconvoluted or 'resolution enhanced' spectra, making use of the fact that the relative areas under deconvoluted profiles remain the same. Here we arrive at the point that deconvolution largely determines the outcome of the analysis, since overdeconvolution gives rise to distortion of the relative peak areas or even may introduce erroneous

bands, which are afterwards taken as real, measured bands. In the procedure developed by Goormaghtigh et al. [56], this problem is addressed by performing a final fitting procedure on a spectrum, deconvoluted with a K-factor of 1.0 (i.e. no band narrowing). Still the danger exists that bands which, due to a higher K-factor, might be introduced erroneously in an earlier stage of the procedure, using a higher K-factor, are not recognized as such.

As an alternative to the use of deconvoluted amide I profiles, Dong [32] preferred to determine the relative areas in second derivative spectra. However, this method should be definitively abandoned, since there is no relation between the area in the second derivative and the absorbance spectrum. This e.g. is illustrated in figure 1.14, which clearly shows that the ratio of the areas of the bands at 1550 and 1650 cm^{-1} of 4 to 1 (trace A) is not preserved in the second derivative (trace C).

We prefer a more conservative approach, which involves curve fitting of the original, measured absorption spectra (Fig. 1.18).
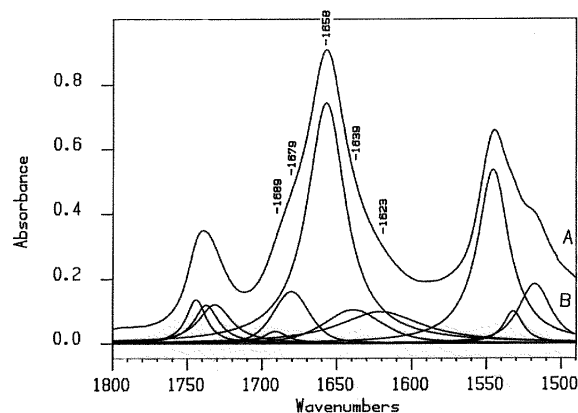
Figure 1.18: *Decomposition of absorption bands by curve fitting. A, expanded IR spectrum of photoreceptor membranes, showing amide I and amide II bands, which largely represent the secondary structure of the photoreceptor protein, rhodopsin; B, separate spectral components, as deduced by secondary derivative analysis, deconvolution and curve fitting. Co-addition of these bands yields the same spectrum as compared to trace A.*

The number of input bands and the peak positions are taken from a second derivative or a moderately deconvoluted spectrum. Additional bands may be added, guided by shoulders present in the deconvoluted spectrum and by the difference between the measured profile and the profile, generated by

co-addition of the input bands. After full optimization, the best fit can be examined by comparing the deconvoluted spectrum of the best fit with that of the originally measured spectrum, using identical deconvolution parameters. This final check, immediately discloses errors in linewidths as well as omitted or spurious bands. The complete fitting procedure of parts of absorbance spectra is quite laborious, but in our opinion it yields the most honest and realistic results, since spectral manipulation is kept to a minimum [93].

1.6 Outline of this thesis

The success of studies, aiming at the elucidation of the structure and function of complex biochemical systems, such as the photoreceptor membrane, or receptors in general, heavily depend on the development of instrumentation capable of detecting minute changes in the receptor, evoked by light or by binding of an agonist. In the last decade, FT-IR spectroscopy has proven to be such a technique, which not only detects protein structural changes but also is useful for studying membrane structure and dynamics and interactions between reacting components.

In this chapter, an introduction on (FT-)IR spectroscopy is given, covering some theoretical background, instrumentation and analysis of IR spectra. The use of difference spectroscopy is outside the scope of this thesis, although it is frequently used in photoreceptor research.

Chapter 2 introduces the photoreceptor, rhodopsin, as a prototype of the superfamily of G-protein coupled receptors.

In chapter 3, the versatility of FT-IR spectroscopy is illustrated by applying it to the quantitative and qualitative analysis of residual detergent in bio-membranes.

Until recently, the photoreceptor membrane has been mainly studied by means of FT-IR difference spectroscopy, to analyze light-induced conformational changes. An IR spectrum of a protein however, also contains direct information regarding the secondary structure of the protein under study. Chapter 4 describes such a study on the secondary structure of rhodopsin, utilizing the amide I and amide II bands in the IR spectrum of photoreceptor membranes. In order to avoid interference by vibrational bands of water, a new approach was explored by using dehydrated membrane films.

As a preparatory study before analyzing the more complex and highly unsaturated lipid matrix in the photoreceptor membrane, in chapter 5 the

interactions between another transmembrane protein, viz. Na^+, K^+-ATP-ase, and its lipid matrix are explored. This chapter mainly focusses on IR-signals, originating from phospholipids. The method of analyzing the results is derived from the analysis of industrial polymers.

Finally (chapter 6), a study related to the age-dependent, non-enzymatical degradation of proteins is presented as another illustration of the versatility of FT-IR spectroscopy. A succinimide derivative of the amino acid aspartic acid, which is believed to be an intermediate in the protein aging process, is characterized by means of vibrational spectroscopy.

This thesis finishes with a summarizing discussion.

Chapter 2

The photoreceptor, rhodopsin

2.1 Introduction

Acting like a photographic film, the retina is the tissue in the vertebrate's eye that registers the light, projected onto its photo-sensitive surface. Almost instantaneously, the detected light is converted into nerve impulses. These electrical signals are transferred to the central nervous system, where they are recombined, ultimately leading to perception of an image [161]. The photosensitivity of the retina resides in two types of specialized photoreceptor cells, viz. rod and cone cells (Fig. 2.1). The often cone-shaped cells, concentrated in the 'yellow spot' or fovea (the area around the optical axis of the human retina), are associated with color vision and operate under bright light conditions. According to their wavelength sensitivity, the human cone cells can be divided into the three sub-types red, green and blue, corresponding to the wavelength at which maximum absorption occurs (565, 535 and 420 nm respectively) [161, 108]. The more abundantly occurring rod shaped cells (95 % of approximately 130 million photoreceptor cells in the human retina), are located more to the periphery of the retina, and are responsible for vision under dim light conditions and have their maximal sensitivity at about 498 nm.

A schematic drawing of a rod cell is given in figure 2.2. It appears that the rod cell is divided in two main compartments, viz. the rod outer segment (ROS) and the rod inner segment (RIS). The inner segment ends in a synapse, which provides for intercellular signal transfer. This compartment contains the nucleus and the other organelles, required for cell maintenance,

31
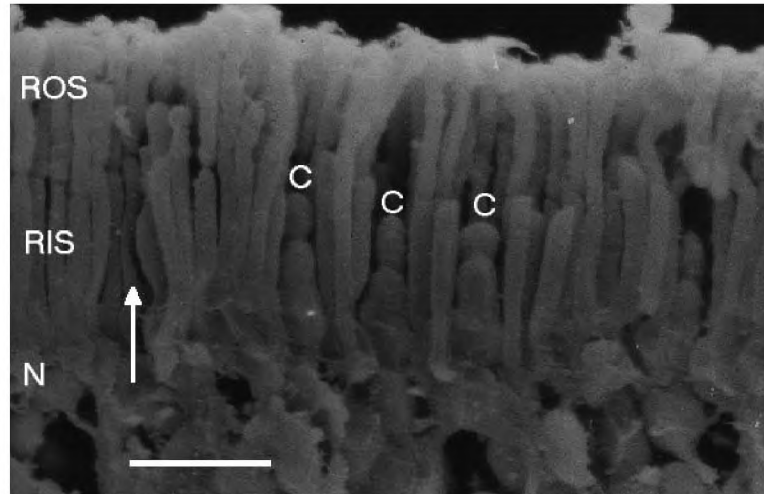
Figure 2.1: *Scanning electron micrograph of the bovine retina. Clearly visible are the slender, segmented rod cells and, some isolated, shorter cone cells (C). The rounded shapes in the lower part of the photograph harbor the photoreceptor cell nuclei (N). The direction of incident light is indicated by an arrow. The neuronal cell layers (which should be below the nuclear layer) and the retinal pigment epithelium layer (on top of the rod outer segments) are not visible in this photograph. The bar represents 10 µm. (With thanks to H.P.M. Geurts, Dept. of Electron Microscopy, Faculty of Science)*

whereas the outer segment harbors a stack of flattened vesicles or discs (typically several hundred up to some thousand in rod cells), which contain the components necessary for photoreception. The axons of the ganglion cells, which transmit the retinal 'message' via the optic nerve to the central nervous system, are located at the surface of the retina. This means that, prior to detection in the outer segments, the light passes through the ganglion cell layer, a layer of intra-retinal neurons and the rod inner segments.

The cone cells have an overall construction similar to the rods, but the outer segments are usually shorter and their photoreceptor membranes are not 'pinched off' from the cell membrane after their assembly. Although rod and cone cells are morphologically and functionally different, evidence is available that the underlying mechanisms through which these cells convert light into an electro-physiological response are very alike.
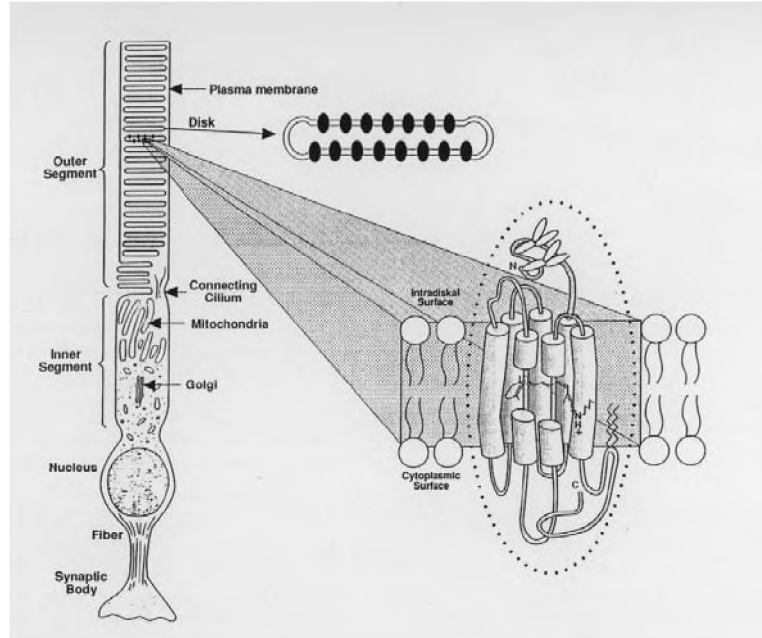
Figure 2.2: *Schematic drawing of a rod cell. The outer segment contains about up to a thousand discs, which form the major sites for photoreception. The inner segment contains the other cellular organelles. The nucleus is somewhat separated from the inner segment. The right part shows the positioning of rhodopsin, which consists of the apoprotein, opsin, and a prosthetic group, 11-cis retinal, in the centre of the protein. (Adapted from [61]. See also Fig. 2.1).*

The large predominance of the rod cells, relative to the cone cells, makes them better accessible to biochemical analysis and allows to study the structural and functional properties of the rod phototransduction system in more detail. Eventually, such studies will also contribute to the understanding of (hereditary) lesions to the human visual system, e.g. color blindness [108] or retinitis pigmentosa [2, 9].

2.2 Structure of photoreceptor membranes

The primary light reaction occurs within the photoreceptor protein, rhodopsin. This protein is embedded in the phospholipid matrix of the ROS cell

membrane as well as in the membranes of the stack of flattened vesicles or discs (Fig. 2.2 right). Unlike other receptors, which are activated by binding of an agonist, rhodopsin contains a covalently bound prosthetic group, 11-*cis* retinal, which is derived from vitamin A [107]. In the last stage of the light reaction of rhodopsin, this group is released and the apoprotein opsin, i.e., a protein lacking its prosthetic group, is formed. By re-incorporating 11-*cis* retinal, the light-sensitive protein, rhodopsin, is regenerated.

Bovine rod opsin is an integral membrane protein, consisting of a single polypeptide chain of 348 amino acids and a molecular weight of approximately 41000. Its primary structure was determined independently by Hargrave [62] and Ovchinnikov [111] in the early eighties. Post-translational modifications include glycosylation [60] at Asn_2 and Asn_{15} and thio-palmitoylation at Cys_{322} and Cys_{323} [113]. Opsin also contains a disulfide bridge between Cys_{110} and Cys_{187}.
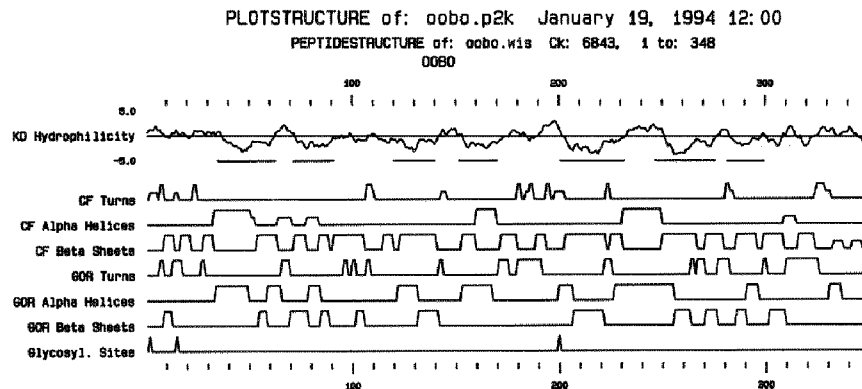
Figure 2.3: *Complete protein sequence analysis of bovine opsin. Hydrophilicity analysis, according to Kyte and Doolittle [82], KD, is combined with the secondary structural predictions according to the methods by Chou and Fasman [16], CF, and Garnier et al. [50], GOR.*

Accessibility studies [113, 112], employing limited proteolysis, monoclonal antibodies and various labeling techniques, combined with computer assisted sequence analysis [117] (Fig. 2.3), demonstrate that opsin has an odd number of membrane spanning domains (most probably 7). This implies that the amino terminus and the carboxy terminus of the protein are located at opposite sides of the membrane. This has recently been confirmed experimentally by electron scattering studies [144].

Early biophysical studies have disclosed that opsin and rhodopsin contain a large proportion of α-helical structure (about 57 %), oriented almost perpendicularly to the membrane surface [150, 137, 33]. These results are more or less in contrast with the earlier predictions of secondary structure, owing to the fact that these methods are based on the structure of globular proteins. However the most recently developed method, employing neuronal networks [135, 134] performs better (58 % helical trans membrane domains and 30 % extended, i.e. β-type secondary structure) [1].

Combination of all experimental data lead to the two-dimensional model, presented in figure 2.4. In the past few years, other models have been put forward, but essentially, they all show the same features [111, 62, 117].
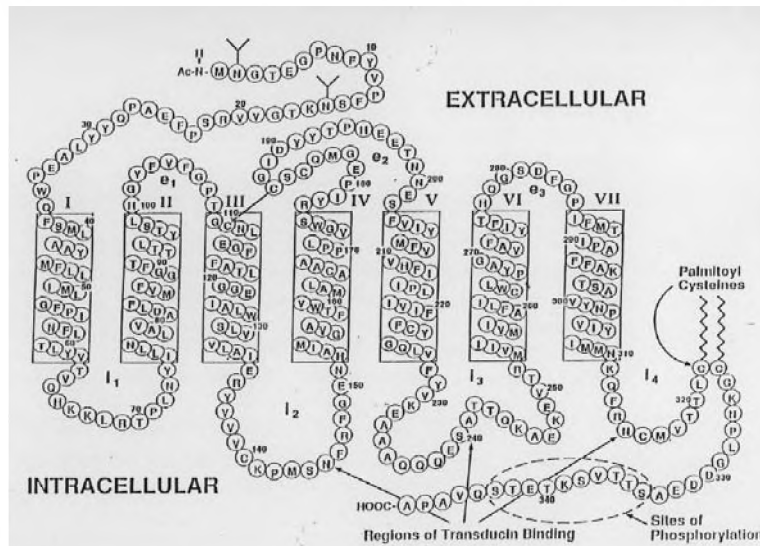
Figure 2.4: *Structural model of bovine opsin, based on immunochemical, proteolysis, labeling studies and computer assisted sequence analysis. The putative transmembrane segments are boxed (Adapted from [61]).*

The phospholipid composition of the ROS membranes is rather uncommon with regard to its high degree of unsaturation and the presence of extremely long acyl chains (Table 2.1) [102]. Major lipid species are PC, PE and PS. Owing to their high degree of unsaturation, PS and PE are capable of forming non-bilayer structures (polymorphism) [102].

---

[1]It should be noted that this method still places the supposed Schiff base counterion, Glu_{113}, *outside* any trans membrane domain.

acyl chain	ROS	PS	PE	PC
Mole-% of total:		19 ± 2	43 ± 1	38 ± 2
16:0	18.3	6.2	12.7	26.0
18:0	21.7	21.9	25.8	18.5
18:1/2	7.1	1.8	4.4	4.7
20:4	6.3	3.2	4.0	4.5
22:5/6	37.5	46.5	50.0	33.3
24:4/5/6	3.4	19.3	3.1	2.4
26:4/5/6	0.4			1.1
28:4/5/6	1.3	0.6		0.2
30:4/5/6	0.2			0.7
32:4/5/6	1.7	0.3	0.1	5.5
34:4/5/6	1.8	0.3		2.7
36:4/5/6	0.2			0.4

Table 2.1: *Phospholipid composition of ROS membranes [102]. Values are in mole-%.*

The presence of rhodopsin however, prevents the formation of non-bilayer, i.e. hexagonal H_{II}, structures in spite of the high Ca^{2+} content of the intra-discal space [103]. The role of the ultra-long and highly unsaturated phospholipids is still unclear but the work of Gibson and Brown [165, 53] has already revealed that the phospholipid headgroup composition as well as the degree of unsaturation influence the formation of the signal transducing intermediate, metarhodopsin II.

2.3   The photolytic cascade

Upon capture of a photon, the 11-*cis* double bond in the chromophore of rhodopsin, retinal, isomerizes to the *trans* conformation. This triggers a sequel of structural changes in rhodopsin, known as the photolytic cascade. The photolytic intermediates have been identified at low temperatures by their maximum absorbance wavelengths (Fig. 2.5) [161, 171].

The first intermediate, formed within picoseconds after illumination, is bathorhodopsin. At this stage, according to FT-IR difference spectroscopy, changes have predominantly taken place in the chromophore, reflecting the
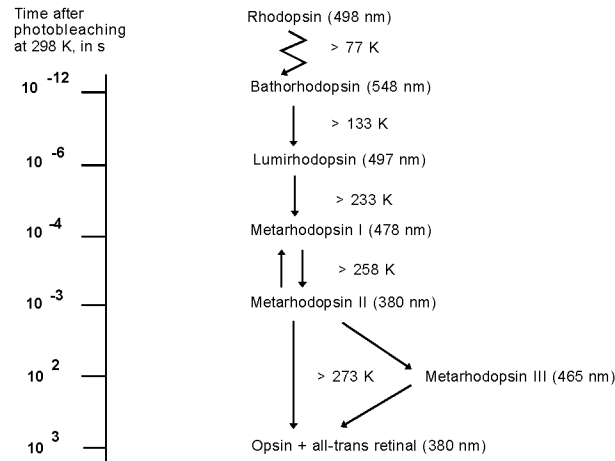
Figure 2.5: *Photolytical cascade of rhodopsin. The photolytic intermediates were identified at low temperatures by their spectral properties (absorbance maximum is indicated).*

conversion of 11-*cis* to a somewhat strained *all-trans* retinal chromophore [28]. Initial vibrational spectroscopic (FT-IR and Raman) studies have mainly focussed on this intermediate with regard to the assignment of the vibrational bands associated with the chromophore [115, 28, 44]. Hereto, rhodopsin analogs have been formed by regenerating opsin with numerous retinal analogs, with a variety of isotope substitutions, *cis* double bond locations and ring or chain substituents. The next intermediate, lumirhodopsin, is mainly characterized by a relaxed *all-trans* chromophore [28, 45, 46]. Small protein secondary structural changes now also appear, which augment upon transition to the next intermediate, metarhodopsin I [27, 28, 46]. Structural changes in the chromophore are no longer detected. The most important, i.e. signal transducing intermediate, metarhodopsin II, shows the largest protein secondary structural changes relative to unilluminated rhodopsin [27, 28]. By removal of the protein domains, protruding from the membrane surface, it can be shown that some of these changes occur at the cytoplasmic side of the photoreceptor membrane [43, 118]. Formation of metarhodopsin II is also accompanied by changes in the hydrogen bonding network, proposed to surround the chromophore [27]. Recently, it has been shown that Asp_{83} is involved in this network [129, 36].

Metarhodopsin II decays to form opsin and *all-trans* retinal, part of which
is bound as a distinct species, metarhodopsin III. During these transitions,
the structural changes which appeared in the formation of metarhodopsin II,
are partially reversed [136]. Figure 2.6 shows the formation of the late pho-
tolytic intermediates, as monitored by UV-vis spectroscopy. Upon illumi-
nation during 15 seconds, at ambient temperature, a pH of 6.5 and a time
resolution of 2 minutes, the major intermediate formed is metarhodopsin II
(λ_{MAX}=380 nm). In absence of other components of the signal transduction
'machinery', this intermediate, quite slowly, decays to form metarhodopsin III
(λ_{MAX}=465 nm) and opsin plus *all-trans* retinal.
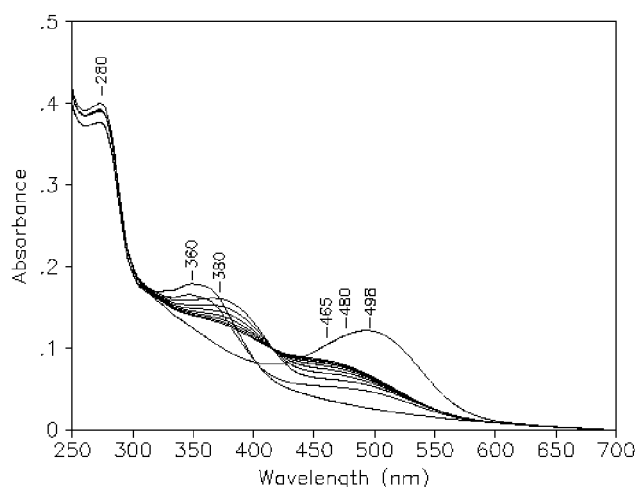
Figure 2.6: *Photolysis of rhodopsin. After illumination during 15 sec-
onds (pH=6.5 at ambient temperature), rhodopsin is mainly converted into
metarhodopsin II (λ_{MAX}=380 nm). This intermediate slowly decays to
metarhodopsin III (λ_{MAX}=465 nm), as is evident from the decreasing ab-
sorbance at 380 nm and concommittantly increasing absorbance at 465 nm.
After 20 minutes, NH_2OH is added, which captures the liberated* all-trans
*retinal (λ_{MAX}=360 nm). Finally, a second illumination bleaches a residual
small amount of rhodopsin.*

2.4 Signal transduction in the photoreceptor cell

Metarhodopsin II is the only photoproduct of rhodopsin, which is capable of initiating the cascade of enzymatic processes, resulting, by means of hyperpolarization of the photoreceptor cell, in the generation of a receptor potential. The complete process of transforming a visual stimulus into an electrical response is more generally called phototransduction, i.e. the energy, corresponding with electromagnetic radiation (photon) is used to generate an amplified, electrochemical signal (an electrical potential difference across a cell membrane).

The structural changes which have occurred in rhodopsin at the stage of meta(rhodopsin) II are such that a GTP-binding protein (the so-called G-protein or transducin, T) forms a complex with the light-activated rhodopsin [149, 59]. This binding allows exchange of the GDP for GTP in the α-subunit of the G-protein. The GTP-T_α complex dissociates from the $\beta\gamma$ -subunits and in turn, activates a cyclic GMP phosphodiesterase (PDE), which hydrolyzes cGMP into GMP [128] (Fig. 2.7).
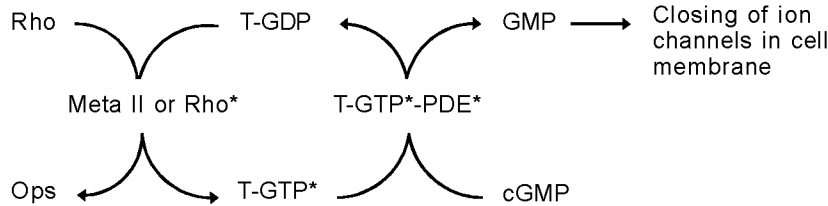
Figure 2.7: *Triggering of signal transduction by photo-activation of rhodopsin. Rho, rhodopsin; Ops, phosphorylated opsin; meta II, metarhodopsin II. An asterisk denotes an activated complex.*

Since cGMP is an allosteric agonist of an aselective cation channel in the plasma membrane of the ROS, the resulting decrease in cGMP concentration leads to closure of these channels, thereby reducing the influx of Na^+ into the photoreceptor cell. The K^+ -selective channels however, are not affected, owing to which the cell hyperpolarizes towards the K^+ -equilibrium potential. This hyperpolarization (receptor potential) immediately spreads towards the

synapse where, finally, a nerve impulse is generated by modulating the release of a neurotransmitter. The extreme sensitivity of this system comes from the fact that even a single photon can activate rhodopsin, which in turn can activate several hundred G-protein molecules per second. In the next steps the gain is further increased, since each activated PDE hydrolyzes 4200 cGMP molecules per second. This, ultimately, inhibits the influx of more than a million Na^+-ions per second [128, 149].

For proper vision, the activated rhodopsin (i.e. meta II) has to be rapidly inactivated. Since spontaneous decay of meta II is too slow ($t_{1/2}$ of about 60 s at 310 K), a parallel mechanism has evolved. Meta II becomes phosphorylated by a very specific rhodopsin kinase on several sites at the cytoplasmic domains [116, 109, 97], which facilitates the binding of a 48 kD protein, arrestin or S-antigen [83]. This complex inhibits further activation of any G-proteins. Rhodopsin is regenerated from opsin again upon subsequent dephosphorylation and incorporation of 11-*cis* retinal. Meanwhile, remaining activated GTP-T_α subunits are self-inactivated by their intrinsic GTPase activity and subsequently rebind to the $T_{\beta\gamma}$ subunits.

2.5 The family of G-protein coupled receptors

The principles of the scheme for signal transduction, presented in the previous paragraph, not only appears to be valid for photoreceptor proteins (including cone cell photoreceptors and invertebrate photoreceptors), but for a large class of membrane receptors, many of which are of pharmacological importance. Well-known examples are the adrenergic, the muscarinic, the cholinergic and the dopaminergic receptors. By comparing the genetic organization and the amino acid sequences, these receptors show many common structural features, owing to which they have been grouped in the still growing superfamily of G-protein coupled receptors (GPR) [67, 110].

From a practical point of view, rhodopsin can be considered as a model member of this superfamily, owing to its high abundance in the highly specialized photoreceptor outer segments, which makes it easily accessible to study its signal transduction and regulatory pathways by biochemical methods. In this paragraph some of the similarities and differences of the G-protein coupled receptors are discussed on the basis of their primary structure [127].

The GPRs are characterized by their 7 transmembrane domain topography (Fig. 2.4). The N-terminus is at the extracellular side of the membrane and, consequently, the carboxy terminus is at the intracellular side. These transmembrane segments are predicted to have a largely α-helical structure, but conserved Pro residues disturb the regular helical structure, thereby creating a binding cavity for an agonist (or retinal). Moreover, the transmembrane domains also contain charged residues in a mainly apolar environment, which are involved in agonist binding. Except for the GPRs with a short extracellular N-terminal sequence, some Asn residues at the N-terminus are glycosylated. A disulfide bridge, very likely to be formed between Cys_{110} and Cys_{187} in bovine rhodopsin, can also be located at equivalent positions in most other GPRs. Glu_{113}, the postulated counterion of the protonated Schiff base in visual pigments or of ammonium group bearing agonists, is also conserved, either at positions equivalent with 113 or at the equivalent position 111 i.e., immediately adjacent to Cys_{110}.

At the end of the third transmembrane domain, at the intracellular side, the almost invariant sequence Asp-Arg-Tyr (Glu-Arg-Tyr in bovine rhodopsin) is found. This sequence has been shown to be involved in G-protein interaction but is also required for correct insertion of *de novo* synthesized receptors in the membrane of the endoplasmatic reticulum. The second and third intracellular loops, as well as the C-terminus, are involved in G-protein binding. In these domains, little resemblance can be found, reflecting the fact that the receptors bind specific G-proteins. Finally, the C-terminus contains a variable number of Ser and/or Thr residues, which become phosphorylated during the desensitizing stage of the activated receptor.

Chapter 3

Analysis of residual detergent

3.1   Introduction

Apart from dishwashing purposes and polyacrylamide gel electrophoresis (PAGE), detergents play another important role in biochemical research laboratories. This type of compounds is frequently used during the preparation of proteoliposomes, i.e., synthetic combinations of a selected membrane protein with (phospho-)lipids in a pre-defined composition. The lipid matrix of these proteoliposomes can be experimentally varied and hence, they also allow to study protein-lipid interactions, e.g. by means of physicochemical techniques. Recently, a review by Silvius [147] has appeared, which deals with the background of reconstitution techniques. The more practical aspects are covered by Hjelmeland [66], Furth [42] and Klausner [78].

Considering their chemical structure, detergents resemble (phospho)lipids; they also possess a polar headgroup and a non-polar tail. According to their headgroup composition, detergents are classified as cationic, anionic, zwitterionic or polar non-ionic. Some examples are given in figure 3.1.

The formation of proteoliposomes, the so-called reconstitution procedure, initially requires a micellar solution of the purified membrane protein in a suitable detergent [66]. In the mixed micelles, the non-polar domains of an integral membrane protein are covered by the non-polar detergent tails, and thus shielded from the aqueous phase.
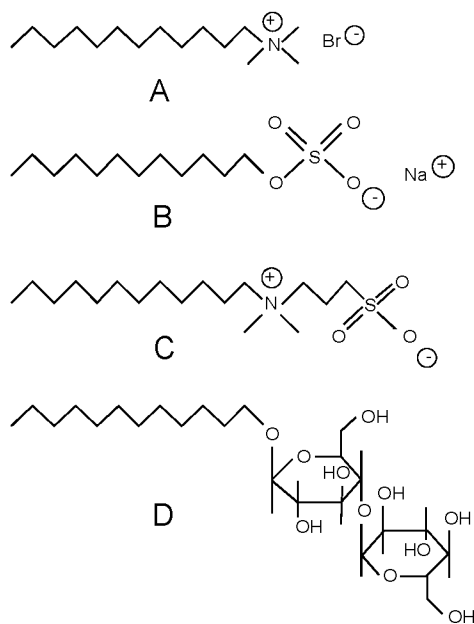
Figure 3.1: *Some representatives of commonly used detergents. A, dodecyl trimethyl ammonium bromide (DTAB, cationic); B, sodium dodecyl sulphate (SDS, anionic); C, N-dodecyl-N,N- dimethyl-3-ammonio-1-propanesulfonate (zwittergent 3-12, zwitterionic); D, 1-β-D-dodecylmaltoside (DOM, polar non-ionic).*

The detergent headgroup will confer a surface charge or a nonionic polar interface to the protein-detergent micelles, which will effectuate strong hydration. The latter effects will keep the protein in solution. Detergent selection largely depends on the protein, e.g., periferal or integral membrane protein and required stability or enzymatic activity of the protein in the micellar solutions. The most promising detergents for this purpose are the anionic cholate-type detergents, the polar nonionic detergents, like the alkylglycosides and the zwitterionic detergents, like CHAPS or Zwittergent 3-12 [66, 167].

After solubilization, the protein solution is mixed with the required (phospho)lipid(s) and through removal of the detergent, proteoliposomes are generated, in which the protein has re-inserted into the lipid bilayer. Removal of detergent can, dependent on the type of detergent, be performed by sucrose density centrifugation [78], dialysis [163], by adding an insoluble detergent-

scavenger like Bio-Beads [22] or by diluting the suspension below the critical micelle concentration (CMC) of the detergent being used.

This critical micelle concentration indicates the concentration at which the detergent solution is saturated with detergent monomers. Above this concentration, formation of micelles will occur. Dilution or dialysis are effective at removing detergents with a relatively high CMC (in the mM range, e.g. cholate and its derivatives). The use of Bio-Beads is to be considered for removal of detergents with a low CMC (e.g. $C_{12}E_8$, CMC=0.087 mM), since these detergents are difficult to remove by methods, based on the concentration difference of the detergent, e.g. across a dialysis membrane.

Verification of the complete removal of the detergent is essential, since small amounts of residual detergent may already affect the lipid phase behavior and/or the properties of the membrane protein [150, 125, 24]. Quantitation of residual detergent is commonly done by performing a parallel experiment with radiolabeled detergent, if available [22]. In such an experiment, the loss of radiolabel in the proteoliposomes is followed as a function of time. Although this determination gives fairly accurate results, there are a few but important disadvantages. Firstly, a costly, qualified C-level laboratory is required. Secondly, expensive, radiolabeled detergents are needed, of which only a limited number is available.

It occurred to us that analysis by FT-IR spectroscopy could provide an useful alternative since it does not require labeling of the detergent. As a consequence, in principle all types of detergents, whether anionic, cationic, zwitterionic or non-ionic, can be analyzed. Once calibration data for a standard preparation are available, quantitation of the detergent can be obtained very rapidly. For routine analysis this procedure can be automated, making use of the quantitative analysis software which is often provided with FT-IR instruments and computers.

In this chapter, this method is exemplified by applying it to two different types of common detergents, viz. the anionic detergent tris-(hydroxyethyl)-ammonium cholate (Fig. 3.2) and the non-ionic detergent 1-β-dodecyl maltoside (Fig. 3.1D). Selection of a characteristic band, suitable for quantitation and calibration is demonstrated. In the case of tris-(hydroxyethyl)-ammonium cholate, its removal during reconstitution of Na^+,K^+-ATPase using dialysis or adsorption to Bio-Beads is followed in time, using both our FT-IR approach and the radiolabeling method. The advantages of the IR-method are discussed.

HO
12
17
20
COX
3
7
HO
R
A. R=OH, X=OH
B. R= H , X=OH
C. R=OH, X=NH(CH$_2$)$_3$$\overset{\oplus}{N}$(CH$_3$)$_2$(CH$_2$)$_3SO\overset{\ominus}{_3}$
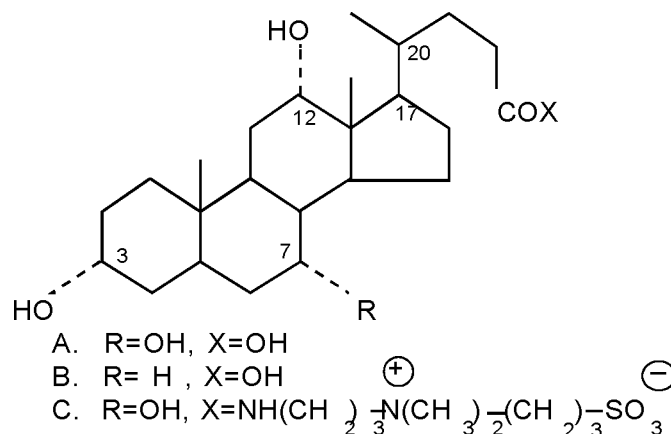
Figure 3.2: *Some derivatives of cholic acid, employed as detergent. A, cholic acid; B, deoxy cholic acid (lacks C7-OH); C, CHAPS.*

3.2   Materials and methods

3.2.1   Sample preparation

Water washed bovine photoreceptor membranes [26] and rabbit kidney Na^+, K^+-ATPase(EC 3.6.1.37) membrane sheets [74] were isolated and characterized according to standard procedures. These preparations have protein/phospholipid ratios of 1/65 and 1/300, respectively. Dodecylmaltose (CMC, 0.16 mM) was synthesized and purified as described before [25]. Sodium cholate (CMC, 14 mM; Merck, Darmstadt, FRG) was recrystallized and converted into tris-(hydroxyethyl)-ammonium cholate (tris-cholate) in order to avoid interference during ion transport studies with Na^+, K^+-ATPase.

Calibration samples for FT-IR analysis were prepared by mixing aliquots of the detergent solution in water (0.5 % w/v) with proteoliposome suspensions of known composition. These samples were deposited on AgCl windows (Fischer Scientific, Pittsburgh, PA), using the iso-potential spin drying method [18]. The films typically contained 1 nmol of Na^+, K^+-ATPase or 3 nmol of rhodopsin. Alternatively, aliquots of proteoliposomes can be applied to AgCl (or CaF_2) windows and dried in an exsiccator over a desiccant.

3.2.2 Reconstitution of Na^+,K^+-ATPase into its native lipids

In a typical reconstitution experiment, Na^+, K^+-ATPase membrane sheets (4.00 mg protein/ml in water) were mixed either with ^{14}C-cholate (radiolabel assay; 1.99 GBq/mmol; Amersham, Little Chalfont, UK) or with 'cold' cholate (FT-IR measurements) in a 1:1 molar ratio of cholate to phospholipid, and were diluted with water to yield a final volume of 10 ml. The resulting suspensions were dialyzed against 2 l water during 50 hours at ambient temperature. The time course of removal of cholate was determined either by monitoring the ^{14}C signal or by FT-IR analysis of 0.3 ml aliquots, taken from the dialysis tubing. Radioactivity of ^{14}C-samples was measured in a Packard scintillation counter (Packard, Meriden, CT) after mixing with 4 ml Opti-Fluor scintillation fluid (Packard). It should be noted that this experiment only mimics the final stage of removal of the detergent, since the added amount of detergent is not sufficient to dissolve the membrane protein.

Alternatively, we tried to remove the cholate with Bio-Beads SM-2 (Bio-Rad, Richmond, CA) according to a described procedure [22]. The amount of Bio-Beads required to give a half time of about 30 minutes was determined by adding increasing amounts of the beads to a fixed amount of ^{14}C-cholate. The residual amount of cholate in the supernatant was determined after incubation for 30 minutes at room temperature, under continuous shaking. In the final experiment, Na^+, K^+-ATPase membranes (0.18 mg/ml in water) were mixed with cholate, as described above. After this period, Bio-Beads were added to a concentration of 120 mg/ml. The removal of cholate by the beads was determined in the same way as described for the dialysis method.

3.2.3 FT-IR measurements

FT-IR spectra were measured in the transmission mode, either with a Perkin-Elmer 1720 X (Norwalk, CT) or a Mattson Cygnus 100 (Madison, WI) single beam spectrometer, equipped with a liquid nitrogen cooled, narrow band MCT detector and interfaced to a microcomputer. The sample compartment was continuously purged with dry nitrogen gas (20 l/min).

Acquisition parameters: Resolution, 8 cm^{-1}; zero filling, twice; number of co-added interferograms, 64; moving mirror speed, 1.27 cm/s; wavenumber range, 4000–750 cm^{-1}; apodization function, triangle; time needed for acquisition and processing of a spectrum, 30 seconds; typical signal/noise

ratio (2200-2000 cm^{-1}), better than 4×10^3.

3.2.4   FT-IR Data analysis

Data acquisition and analysis were performed with the EXPERT-IR software (Mattson). Baseline correction was performed to compensate for the absorbance by the AgCl windows, by manually entering the baseline points at fixed frequencies.

Fourier self-deconvolution parameters [76]: Bandwidth, 16 cm^{-1}; K-factor, 2.0; apodization function, $\sin^2(x)/x^2$; lineshape function, Lorentz.

3.3   Results and discussion

3.3.1   IR-Characteristics of detergents

Prior to quantitation, a characteristic detergent absorption band must be selected, which allows it to be identified in the presence of the many overlapping bands, exhibited in the IR spectra of biomembranes [41]. In figure 3.3 the IR fingerprint region of several cholate-type detergents are collected. The strong carboxylic acid (Fig. 3.3B, 1740 cm^{-1}) and carboxylate (Fig. 3.3A, 1590 and 1400 cm^{-1}) stretching vibrations are easily identified. Another prominent feature is the C-O stretching vibration at 1080 cm^{-1}, which is missing in the spectrum of deoxycholic acid, owing to the absence of the C7-OH group (Fig. 3.3C, indicated by an arrowhead).

CHAPS, an amide derivative of cholic acid (Fig. 3.3D) can be identified by the strong and broad sulfonate band around 1200 cm^{-1}. This band is quite unique because it usually does not occur in IR spectra of common proteoliposome preparations. Quantitative determination of CHAPS should also be possible by alkaline hydrolysis and subsequent reaction with ninhydrin, as proposed recently for amide-containing detergents by Brenner-Henaff et al. [13]. In proteoliposomes however, the high 'background' of phospholipids (phosphatidylserine) and proteins (polypeptide backbone, side chains of Lys) seriously interferes with this determination. The advantages of using FT-IR spectroscopy in this case are obvious.

From these spectra we conclude that cholate is most conveniently determined by the carboxylate symmetric stretching vibration around 1400 cm^{-1}, since the contribution by the detergent to the bands at 1590 and 1080 cm^{-1}
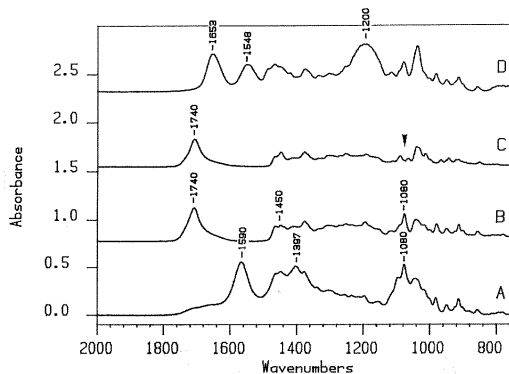
Figure 3.3: *FT-IR spectra of selected cholate-type detergents. Trace A, tris-(hydroxyethyl)-ammonium cholate(anionic). This spectrum exhibits relatively strong δ (CH$_2$) (around 1450* cm^{-1}*) and ν (C-OH) (around 1080* cm^{-1}*) vibrational bands, owing to the tris-(hydroxyethyl)ammonium counterion; trace B, cholic acid; trace C, deoxy-cholic acid (lacks C7-OH group, arrowhead); trace D, CHAPS (zwitterionic). The spectra are scaled, using the strongest $\tilde{\nu}$ (C-H) around 2900* cm^{-1} *and are displayed with offset absorbance axes.*

is more difficult to separate from several other protein and/or lipid vibrations. Although the amino acid side chains of Asp and Glu also contribute to this band, it was chosen since in spectra of proteoliposomes, this band is well-resolved from other vibrational bands (e.g. C-H bending modes around 1450 cm^{-1}) [41]. The contribution by amino acids can be easily compensated for, using proper calibration.

Another important class of detergents consists of the polar, non-ionic detergents. This group contains the alkylglycosides and alkoxy-derivatives, like Triton X-100. IR spectra of these types of detergents are presented in figure 3.4. In the case of the alkylglycosides, the only bands suitable for our purpose, are the carbohydrate C-O stretching bands between 1000 and 1200 cm^{-1} (Fig. 3.4A and 3.4B). Using these highly characteristic bands even the sugar moiety can in principle be identified (e.g. glucose: 1161 cm^{-1}; maltose: 1148 cm^{-1}). The alkoxy-type detergents are easily recognized and quantitated by the characteristic C-O-C stretching band at 1110 cm^{-1}(Fig. 3.4C and 3.4D), which is quite uncommon in IR spectra of biomembranes. This band has already been employed in the quantitative analysis of ethoxylate surfactants in waste water [4].
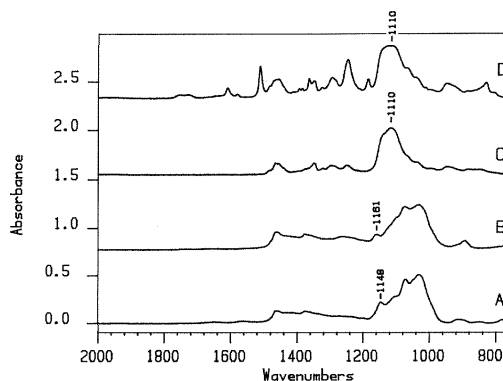
Figure 3.4: *FT-IR spectra of selected nonionic detergents. Trace A, dode-cylmaltose (DOM); trace B, nonylglucose (NG); trace C, $C_{12}E_8$; trace D, Triton X-100. Scaling and axes offset as in figure 3.3. Bands, selected for quantitation are indicated by their wavenumber.*

Using the same acquisition parameters, IR spectra of in total about 60 representative detergents have been recorded. After annotation and indexing these spectra will be made available as a public spectral library on the world-wide computer network, Internet. Access is most easily obtained by using a network navigator program 'Gopher'[1]. Remote database comparison is also considered as an option. It is the author's opinion that such a project is an efficient, user-friendly and cheap alternative to the commercially available libraries (e.g. Sadtler's 'Surface Active Agents' spectral library of some 9000 spectra costs about kfl. 50,-, excluding searching software) and it is to be hoped that more research groups in the field develop similar initiatives.

3.3.2   Calibration of the method

Since the carboxylate band of cholate at 1397 cm^{-1} appears well separated from other bands, calibration of the quantitative analysis of cholate is rather straightforward, provided that baseline correction is carried out consistently. A_{1397} values are ratioed against the A_{1233} value (PO_2^- antisymmetric stretching vibration) to provide a direct relation with the membrane lipid matrix, in which the detergent is imbedded (Fig. 3.5). Linear regression analysis yields the equation: $y = 0.428 \cdot x + 0.657$ (standard deviation, 0.12; correlation coeffi-

---

[1]a provisional service is running at GOPHER://fourier.fmw.kun.nl/
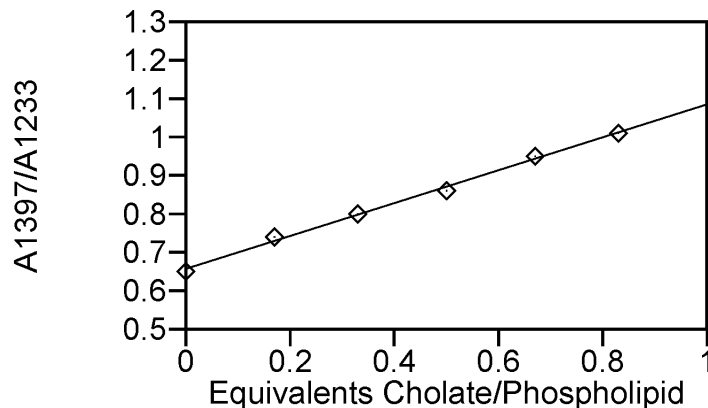
Figure 3.5: *Calibration graph for the determination of cholate in proteolipo-somes. Data are obtained directly from baseline corrected spectra.*

cient, 0.998), with y, the A_{1397}/A_{1233} ratio and x, the detergent/phospholipid molar ratio. Hence, this allows accurate estimation of residual detergent down to as low as one detergent in ten phospholipids (Fig. 3.5).
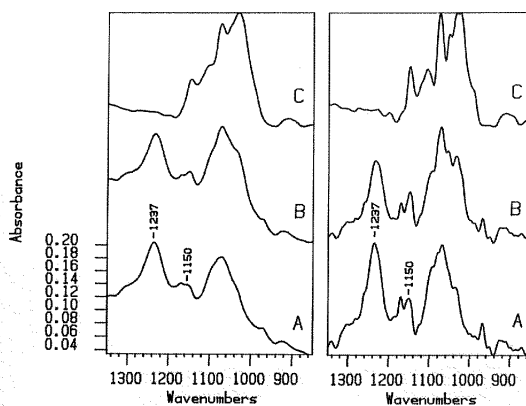
Figure 3.6: *Band separation by deconvolution. (Left) Trace A, absorption spectra of photoreceptor membranes; trace B, DOM in photoreceptor mem-branes with a molar ratio of DOM to phospholipids of 1 to 3; trace C, DOM. (Right) Same spectra as in left panel, but deconvoluted with linewidth 16* cm^{-1}; *K-factor, 2.0; lineshape function, Lorentz; apodization,* $\sin^2(x)/x^2$.

Prior to quantitative analysis of DOM, the characteristic band at 1150 cm^{-1} is separated from other bands by applying Fourier self-deconvolution
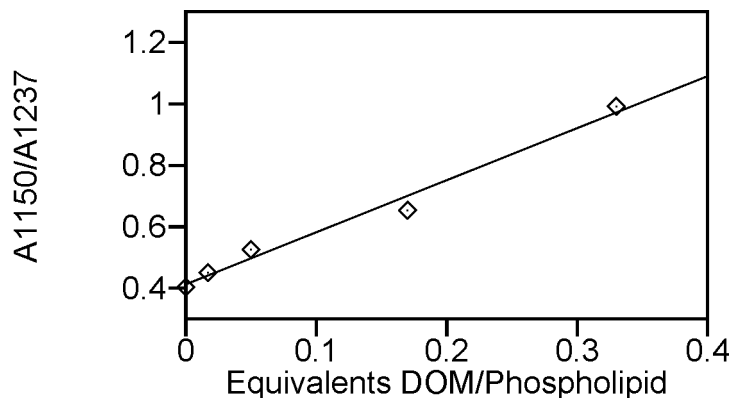
Figure 3.7: *Calibration graph for the determination of DOM in photorecep-tor membranes. Data are obtained from baseline corrected and deconvoluted spectra.*

(Fig. 3.6). Other bands between 1100 and 1000 cm^{-1} have also been tested, but the band at 1150 cm^{-1} appears to be the most reliable for quantitation. The IR absorption at 1150 cm^{-1}, observed in the baseline corrected and deconvoluted spectra is again ratioed to the phosphate band, which now appears at 1237 cm^{-1}. In this way, again a linear calibration graph is obtained (Fig. 3.7). Linear regression analysis of these data gives: $y = 1.694 \cdot x + 0.413$ (standard deviation, 0.21; correlation coefficient, 0.992). The detection limit is in the same order as that for cholate.

3.3.3   Radiolabeling versus FT-IR

The availability of ^{14}C-cholate gives the opportunity to compare the perfor-mance of the FT-IR method with the existing radiolabel method. Hereto, cholate-dissolved Na^+, K^+-ATPase was reconstituted by dialysis into its own, native lipids, according to a standard procedure. The removal of cholate was monitored in a parallel experiment by FT-IR spectroscopy and scintillation counting. Figure 3.8 shows the loss of cholate versus time as measured by either method. The total amount of cholate, measured before the start of the dialysis procedure, was set to 100 %. The datapoints from both analyses agree very well and can be described by a semi-exponential decay curve with a half-life of about 5.5 hours.
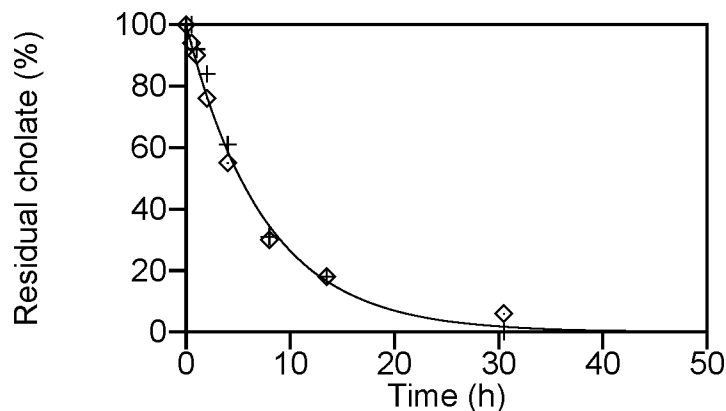
Figure 3.8: *Comparison of radiolabel and FT-IR method for determination of tris-(hydroxyethyl)-ammonium cholate, remaining during dialysis. All values are ratioed against the values obtained before dialysis is started. The curve represents a semi-exponential decay with a half-life of 5.5 hours. $+$, A_{1397}/A_{1233} by FT-IR; $\diamond$, loss of ^{14}C signal.*

In a similar experiment, we studied the removal of cholate by Bio-Beads. Unfortunately, Bio-Beads can also bind variable amounts of phospholipids and membrane protein [147, 22]. This will seriously affect the radiolabel assay, since it cannot correct for this loss, unless the phospholipids are radiolabeled as well. On the other hand the FT-IR approach intrinsically corrects for this loss, due to the fact that the detergent to phospholipid ratio is measured. Figure 3.9 shows the decay curves obtained for this experiment. Clearly, the radiolabel shows removal of cholate with a half time of about 30 minutes under these conditions. However, owing to binding of phospholipids to the beads, this does not reflect the real amount of detergent remaining in the proteoliposomes, relative to the amount of phospholipids. This ratio is given by the IR analysis and the resulting curve strongly deviates from the absolute loss in radiolabel. The deviation is most obvious at later time points when, owing to the reduction in free cholate, the chance that mixed detergent-lipid micelles will bind to Bio-Beads, strongly increases.

In fact the radiolabel assay strongly underestimates the residual *relative* amount of detergent. This, again is a reminder that reconstitution procedures, employing Bio-Beads, should be carried out with a large excess of phospholipids. From these results, it can be concluded that the IR method
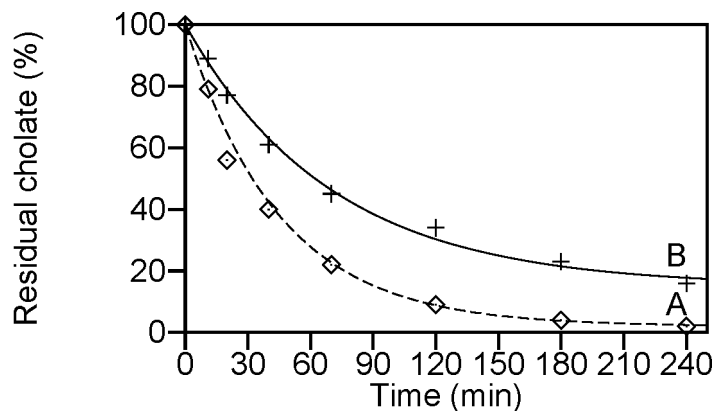
Figure 3.9: *Removal of tris-(hydroxyethyl)-ammonium cholate from a mixture with* Na^+, K^+*-ATPase proteoliposomes, by Bio-Beads SM-2. The figures, obtained before the beads were added, are taken as 100 %. A, loss of* ^{14}C *signal; B, decrease of* A_{1397}/A_{1233}.

is somewhat less sensitive than the radiolabel method but nevertheless gives a good indication whether the detergent has been sufficiently removed as well as whether the absolute amount of phospholipids has been retained. Another very important feature of the IR method, we advocate here, is its general applicability.

3.4   Conclusion

We have demonstrated that FT-IR spectroscopy provides a good approach to the qualitative and quantitative analysis of residual detergent in biomembrane preparations. Although it is less sensitive than a radiolabel assay, IR analysis is faster, less expensive, safer and has a wider scope, since virtually all detergents can be analyzed by this method. Furthermore, because detergent as well as phospholipid and/or protein derived bands are measured simultaneously, FT-IR spectroscopy allows direct, *in situ* estimation of the residual detergent to phospholipid and/or protein ratio, and therefore can also be used under conditions where uncontrollable loss of lipid or protein components occurs.

Chapter 4

The secondary structure of rhodopsin

4.1   Introduction

During the initial stages of the visual process in the vertebrate rod photoreceptor, the light activated photoreceptor protein, rhodopsin, changes its structure in a cascade of spectroscopically distinct intermediates, eventually leading to hyperpolarization of the receptor cell and finally to a nerve impulse (this thesis, chapter 2).

Rhodopsin belongs to the superfamily of G-protein coupled receptors and can be considered as a model for this family since, in contrast to most other members, it can easily be obtained relatively pure in large amounts. Also, its signal transduction pathways have been studied extensively. Analysis by UV-Vis spectroscopy has revealed spectrally distinct intermediate stages in the light-induced activation of rhodopsin. In order to study the underlying conformational changes in chromophore, protein and lipid matrix, FT-IR spectroscopy has proven to be an invaluable and non-invasive technique [28, 43].

Over the last years, FT-IR spectroscopy has also become increasingly popular to estimate the secondary structure of proteins in general, using band fitting analysis of the amide I band [151, 56, 139]. This band (1610–1690

cm^{-1}) represents a peptide bond vibration, mainly involving C=O stretching, while the amide II band (1520–1560 cm^{-1}) mainly results from N-H bending vibrations. In the absence of crystals of sufficient quality for electron diffraction or X-ray crystallography, FT-IR spectroscopy indeed is the only way in which such structural information can be acquired for rhodopsin. Downer et al. [33] reported the first quantitative estimate of the secondary structure of rhodopsin, which was recently improved by Garcia-Quintana et al. [49], who combined Fourier self-deconvolution with maximum likelyhood methods.

In this chapter, a FT-IR analysis of the secondary structure of rhodopsin in dehydrated photoreceptor membrane films is presented. First of all it is demonstrated for proteins, which have been studied extensively by FT-IR, NMR or X-ray diffraction, that structure analysis by FT-IR on dehydrated samples yields results, that compare well with the data from hydrated samples, but is more easy to perform. Subsequently, we have exploited limited proteolytic treatment to assign some of the secondary structural elements to the cytoplasmic domain of rhodopsin. The results are discussed in the light of current structural models for rhodopsin.

4.2   Materials and methods

4.2.1   Isolation of photoreceptor membranes

Bovine rod outer segments (ROS) were isolated in dim red light, using sucrose density gradient centrifugation and velocity sedimentation as described before [26]. The 280 nm/500 nm absorbance ratio of the resulting photoreceptor membranes was 2.0–2.2. Photoreceptor membrane films, suitable for FT-IR analysis, were prepared on AgCl windows, using the isopotential spin dry procedure [18, 27], and typically contained 3–6 nmol rhodopsin (120–240 μg of protein). This results in a dehydrated membrane film, with a spectrally fully normal rhodopsin. Its photolytic cascade, however, is blocked at the meta I stage.

The water-soluble proteins concanavalin A, cytochrome C, lysozyme and α-chymotrypsin were obtained commercially (Merck, Darmstadt, FRG). M13 gene V protein (M13-GVP) and its peptide derivatives, human muscle fatty acid binding protein (MFABP) and mutants and γ -crystallin were kindly provided by several colleagues at the Department of Biophysical Chemistry

and the Department of Biochemistry.

These proteins are also deposited on AgCl windows, using the spin-dry method.

4.2.2 Proteolysis

Proteolysis of rhodopsin with either proteinase K (EC 3.4.21.14, Merck, Darmstadt, FRG) or thermolysin (EC 3.4.24.4, Boehringer, Mannheim, FRG) was essentially performed as described before [27, 81], except that the proteolysis with proteinase K was performed without detergent solubilization, i.e. on the native membrane suspension, so that no reconstitution step was required. The ROS used for this preparation were isolated without PMSF in the isolation buffer, since this inhibits proteinase K activity. Proteinase K treatment of rhodopsin removes the C-terminal 24 amino acids (Lys_{325}–Ala_{348}), 14 amino acids in the third cytosolic loop (Lys_{231}–Gln_{244}) and cleaves the second cytosolic loop [27]. Short term (30 min) digestion of rhodopsin with thermolysin removes the C-terminal 12 amino acids (Val_{337}–Ala_{348}).

Analysis by SDS-polyacrylamide gel electrophoresis and immunoblotting [143], established that proteolysis was over 95 % complete. This limited proteolysis does not significantly alter the sequence or kinetics of the late photointermediates in hydrated (rhodopsin to meta II and meta III transitions) or dehydrated (rhodopsin to meta I) membranes (data not shown).

4.2.3 FT-IR measurements

FT-IR spectra were obtained with a Mattson Cygnus 100 spectrometer (Madison, WI), equipped with a liquid nitrogen cooled, narrow band MCT detector and interfaced to a microcomputer. The optical bench was purged with dry nitrogen gas at a flow rate of 20 l/min. Acquisition parameters: Resolution, 2 cm^{-1}; number of co-added interferograms, 512; moving mirror speed, 2.53 cm/s; wavenumber range, 4000–750 cm^{-1}; apodization function, triangle. The time needed for acquisition and processing of such a spectrum was 4.5 minutes. Signal to noise ratios between 2200 and 2000 cm^{-1} were found to be better than 4×10^3 in all cases. This should permit the use of a K-factor of up to 3.6 during deconvolution operations (The upper boundary of the K-factor is log(SNR) [76]).

Spectral display and analysis were carried out using the EXPERT-IR analytical software (Mattson). Fourier self-deconvolution parameters [76]:

Bandwidth, 18 cm^{-1}; K-factor, 1.8; apodization function, $\sin^2(x)/x^2$; line-shape function, Lorentz. Second derivative spectra were smoothed [142] over 13 datapoints.

Curve fitting of the original absorbance spectra was performed between 1800 and 1490 cm^{-1}, using rather 'conservative' deconvolution parameters (see above) for determining the number and position of the bands. This procedure avoids the introduction of erroneous bands in the final results: an error which seems to occur more often than is generally assumed, upon band fitting of deconvoluted spectra for which higher K-factors are used [152]. Assuming Lorentzian bandshapes, an initial parameter set was generated. Peak positions and bandwidths were manually adjusted, guided by the difference between the measured and the generated spectra. Peak-heights were calculated by the computer. The final optimization procedure, during which all parameters were free for adjustment, was performed automatically by the computer. The quality of the best fit was judged afterwards by the residual error intensity and by comparing the deconvoluted generated spectrum with the deconvoluted original spectrum (Kappers, M. and Van der Maas, J.H., personal communication).

4.3   Results

4.3.1   Pilot studies

In order to test the scope and limitations of estimating protein secondary structure in the dehydrated state from the amide I and amide II vibrational bands in IR spectra, a number of water-soluble proteins, varying in secondary structure, are analyzed. These proteins have been studied before, by means of X-ray crystallography or high resolution NMR spectroscopy and, in a number of cases, also by FT-IR spectroscopy, under several conditions. Analysis of secondary derivative spectra or deconvoluted spectra yields information on the various types of secondary structural elements present. These results, summarized in table 4.1, form the initial parameter set, neccessary for curve fitting. This procedure ultimately yields the relative amount of the structural elements, assuming that the molar extinction coefficient of the corresponding absorption bands is not significantly different. The quantitative results, given as percentages of the total area of the amide I band, are presented in table 4.2.

protein	α-helix	β-type	β-turns
GVP		1625, 1644 (1689)	1663, 1675
MFABP	1662	1639 (1689)	1673
Cryst.	1657	1638 (1689)	1657, 1666, 1676, 1689
Con. A		1633, 1640 (1694)	1655, 1666, 1678, 1694
Chymo	1660	1639 (1690)	1666, 1677
Lysozyme	1658	1646 (1689)	1666, 1676
Cyt. C	1658	1631 (1687)	1673

GVP, gene V protein; MFABP, muscle fatty acid binding protein; Cryst., γ-crystallin; Con. A, concanavalin A; Chymo, α-chymotrypsin; Cyt. C, cytochrome C.

Table 4.1: *Amide I bands, detected in FT-IR spectra of selected proteins in the dehydrated state, by applying secondary derivative and FSD analysis. Frequencies in* cm^{-1}. *Owing to their low relative intensity, and uncertain origin, the β-type bands around 1690* cm^{-1} *are placed between parentheses and are not considered in the final results of the β-sheet contribution.*

These values are compared with the results obtained by X-ray crystallography or high resolution NMR spectroscopy.

M13 Gene V Protein (GVP). The GVP, encoded by the filamentous phage M13 and related phages, is a small (dimer, 87 amino acids per monomer) single-stranded DNA-binding protein. Its structure and DNA-binding properties have been studied extensively by X-ray crystallography [148] as well as NMR spectroscopy [34]. The secondary structure can be described by three major β-loops, two of which are interconnected by the so-called broad connecting loop.

The β-loops are represented by a strong band at 1644 cm^{-1}(64 %), and two weaker bands at 1625 and 1690 cm^{-1}(5 and 11 %, respectively). One might argue that a band at 1644 cm^{-1} is more in agreement with a random, unfolded structure, but this frequency for random coils is only observed after exchange of the amide hydrogen atoms by deuterium atoms. Although the strongest β-type structural contribution to the amide I band is normally found below 1640 cm^{-1}, such a high frequency for β-type structures has been observed before, e.g. in the cyclic decapeptide gramicidin S [106]. The β-turns are represented by bands at 1663 and 1675 cm^{-1}(8 and 12 %). Assuming that the molar extinction coefficients of the major amide I bands

protein	α-helix	β-type	β-turns	not assigned
GVP		69	20 (20)	11
MFABP	10 (14)	60	14 (15)	16
Cryst.	<11 (11)	48 (52)	>24	17
Con. A	<13 (3)	56 (60)	>22	9
Chymo	7 (11)	50 (50)	29	14
Lysozyme	46 (45)	23 (20)	13	18
Cyt. C	55 (50)	>4 (10)	>12	29

GVP, Gene V protein; MFABP, muscle fatty acid binding protein; Cryst., γ-crystallin; Con. A, concanavalin A; Chymo, α-chymotrypsin; Cyt. C, cytochrome C.

Table 4.2: *Estimation of secondary structures of selected proteins, by band fitting of the amide I band in FT-IR spectra of dehydrated samples. The data in table 4.1 were used as starting set. The secondary structural contributions are expressed as relative areas (in %) of the amide I band (standard deviation, ± 2 %). The values between parenthesis represent the contributions as far as described by the pdb files. The 'less than' signs indicate the presence of β_I-turns, which also absorb at 1657* cm^{-1} *(α-helix position).*

are roughly equal and considering the band at 1690 cm^{-1} as a 'satellite' band of β-type vibrations, the β-turn bands (20 %) account for about 17 residues or 6 turns of 3 residues, which are also found by NMR spectroscopy [34].

Recently, two cyclic peptides of different length, mimicking the DNA-binding wing have been analyzed by NMR and FT-IR spectroscopy (Rietman, B. and Pistorius, A., unpublished results). Using both techniques, evidence was found for a β-sheet folding pattern in a cyclic 11-mer, giving rise to bands at 1632 and 1690 cm^{-1}, whereas a cyclic 23-mer exhibited a distorted structure and impaired DNA-binding. In this case, the IR spectrum only revealed a major band around 1671 cm^{-1}.

Human muscle fatty acid binding protein (MFABP). The tissue-specific fatty acid binding protein (133 amino acids), which exhibits homology with the cellular retinol binding proteins [158], consists of two five-stranded β-sheets, in an orthogonal orientation relative to each other, and two short α-helical fragments [172]. This protein can be obtained either by a laborious isolation procedure or by heterologous expression in E. coli bacteria [158]. The latter procedure results in a higher yield and a higher purity.

The β-sheets are characterized by a strong band at 1639 cm^{-1}(60 %). The band at 1673 cm^{-1} (14 %) accounts for the β-turns. A more detailed analysis is not possible owing to the presence of short α-helical segments. This contribution, which is expected at 1657 cm^{-1} could not be resolved from the possible turn-contribution at 1662 cm^{-1}.
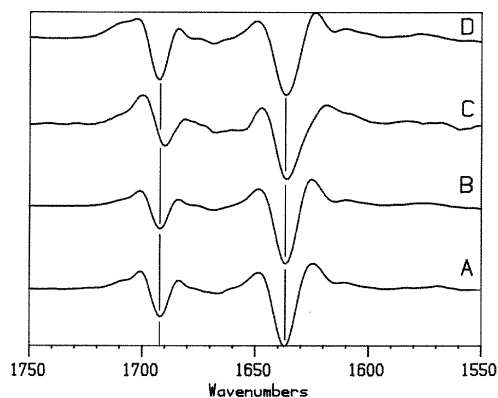
Figure 4.1: *FT-IR spectra of E. coli-derived MFABP and some selected mutants. Second derivative spectra, smoothed over 13 datapoints, are shown. A, native MFABP; B, Phe$_{57}$Ser. This position is located at the exterior of the protein. No structural change is observed; C, Phe$_{16}$Ser. This substitution apparently distorts part of the helical structure around this position. Ser is known to induce turn-structures; D, Thr$_{40}$Glu. A negative charge is introduced in the fatty acid binding cleft, possibly modifying the relative orientation of the β-clam, as deduced from the changing A_{1689}/A_{1638} ratio.*

By applying FT-IR spectroscopy to dehydrated samples of MFABP mutants, small secondary structural changes can be observed, as well as the modification of the amino acid side chain (Prinsen, C. and Pistorius, A., unpublished results). In figure 4.1, the second derivative of the carbonyl region of the IR spectra of wild type MFABP and some mutants are collected. The substitution Phe$_{57}$Ser in a solvent exposed β-turn has little or no effect on fatty acid binding affinity and no significant effects on secondary structure (Fig. 4.1A and B), whereas the same substitution (Phe$_{16}$Ser), located in a supposed α-helical domain, causes small but significant changes around the helix band and β-turn band (Fig. 4.1C). This mutant exhibits no binding of fatty acid. Another substitution, located in the fatty acid binding cleft (Thr$_{40}$Glu), primarily changes the relative intensities of the β-sheet bands at

1638 and 1689 cm^{-1}(Fig. 4.1D), possibly indicating a change in the relative orientation of the β-clam.

γ-crystallin. One of the main protein constituents of the vertebrates' eye-lens is γ-crystallin (174 amino acids) [10]. According to X-ray crystallography [166], this protein is folded into two globular domains, mainly consisting of β-sheets (52 %) and a small amount of α-helices (11 %). This is confirmed by our FT-IR results, which show a band at 1638 cm^{-1}(48 %). A band at 1657 cm^{-1} seemingly shows the correct value for the α-helical contribution (11 %). However, this value should be corrected for the strong absorption of β_I-turns at this position, which are known to be present. Our quantitative estimates are in agreement with those obtained from samples in H$_2$O by Lamba et al. [84].

Concanavalin A. Like γ-crystallin, the lectin, concanavalin A (237 amino acids) also possesses a relatively small amount of α-helical structure (3 %) and several β_I-turns. This results in a band at 1655 cm^{-1} with a relative intensity of 13 %, accounting for both structural types. The relative amount of β-sheet structures, represented by the bands at 1633 and 1640 cm^{-1}(60 %), is in good agreement with X-ray crystallography [86] and previous IR measurements [56, 139, 85].

α-chymotrypsin. Also α-chymotrypsin (241 amino acids) has also been studied before by FT-IR [56, 139, 85], as well as by X-ray crystallography [86]. Again, our results are in good agreement with previous reports. We measure a β-sheet contribution (1639 cm^{-1}) of 50 %, and an α-helix contribution (1660 cm^{-1}) of 7 %.

Lysozyme. Chicken egg lysozyme (211 amino acids) has a higher degree of helical structure (about 45 %) and less β-sheet (20 %) according to its crystal structure [86]. We find a band at 1658 cm^{-1}(46 %), which will represent α-helix and a band at 1646 cm^{-1}, which in view of its relative intensity of 23 % , could represent β-sheets, although as in the case of GVP, this frequency is rather high.

As noticed before by Bandekar [7], the amide II vibrational band of mainly α-helical proteins at about 1542 cm^{-1} also gives a good indication of the amount of α-helix. In the case of lysozyme, this yields a value of 43 %, which very well agrees. In most studies this band cannot be used, since the protein is usually dissolved in ^{2}H$_2$O, which shifts the amide II band to approximately mately 1450 cm^{-1}, owing to isotope exchange.

Cytochrome C. The major structural theme of the one-electron transfer protein, cytochrome C (103 amino acids), are α-helices, surrounding the

heme prosthetic group. These are represented by a band at 1658 cm^{-1} with a relative intensity of 55 %, in agreement with X-ray studies [86] and FT-IR studies [56, 139, 85]. Also here, the amide II band of cytochrome C gives a good indication of the amount of helical structure present: 48 %.

4.3.2 Application to rhodopsin

Figure 4.2 shows the absorbance spectrum of a dehydrated ROS membrane film, together with its deconvoluted spectrum and the second derivative spectrum (trace A, B and C respectively). By making use of FSD as well as second derivative spectra, we identify 5 amide I components and 2 major amide II components attributed to the polypeptide backbone, i.e. at 1623, 1639, 1658, 1679 and 1689 cm^{-1}(amide I) and at 1545 and 1529 cm^{-1}(amide II). Other vibrational bands in this region can be assigned to amino acid side chains, e.g., Tyr (1516 cm^{-1}, C=C stretching in aromatic ring), Glu and Asp (1596 cm^{-1}, COO$^-$ anti-symmetric stretching vibrations). The band around 1740 cm^{-1} mainly represents the lipid ester carbonyl stretching vibration.
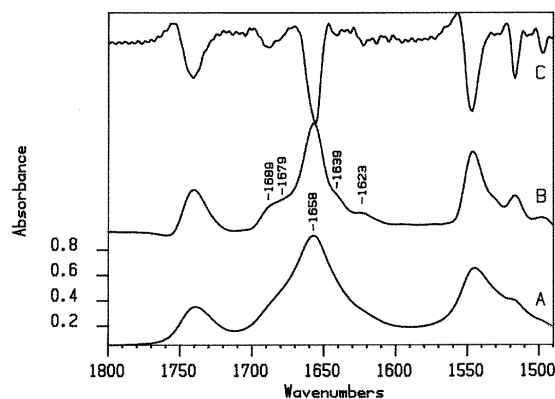
Figure 4.2: *Qualitative analysis of rhodopsin secondary structure. A, Original IR absorbance spectrum of unbleached, dehydrated photoreceptor membranes; B, spectrum A after deconvolution according to Materials and Methods section; C, second derivative of spectrum A.*

Curve fitting, based on this initial set, yields highly reproducible peak positions, fractional areas (table 4.3) and low residual error intensities (less than 0.05 % of the total integral of the amide I band). The amide II band, the ester carbonyl band and the amino acid side chain contributions are

This work				Garcia-Quintana	
$\tilde{\nu}$	$\Delta\tilde{\nu}_{\frac{1}{2}}$	A_{rel}	Assignments	$\tilde{\nu}$	A_{rel}
1623±1	34±1	12±2	β-strands	1626	11±1
1639±1	27±1	17±2	mainly β-sheet	1639	15±1
1658±1	16±1	55±2	mainly α-helical	1)	59±1
1679±1	16±2	12±2	β_{II} -turns	2)	12±1
1689±1	11±1	4±1	β-type	1690	4±1

1): combined contributions of 1649+1656+1666 cm^{-1}
2): combined contributions of 1674+1681 cm^{-1}

Table 4.3: *Amide I substructure composition of native rhodopsin. Peak positions and linewidths are given in* cm^{-1}. *The peak areas are given in percentages of the total amide I area. For comparison, the values, obtained by Garcia-Quintana et al. are given in the right part. The relative areas of the bands at 1649 and 1666* cm^{-1} *are added to the band at 1656* cm^{-1} *and the contribution of the band at 1674* cm^{-1} *is added to the band at 1681* cm^{-1}. *All values: mean ± rounded S.D. (n=3).*

incorporated in the analyses, in order to preclude truncation artifacts, but we focus on the amide I components, since these bands are readily accessible for secondary structural analysis.

Comparison of the deconvoluted measured amide I profile and the deconvoluted fitted band profile (Fig. 4.3, trace A and B), shows that the data from table 4.1 adequately describe the amide I band. When we apply higher K-factors and deconvolute the best fit (i.e. a generated spectrum with an amide I profile, composed of five discrete bands), actually more than the five original bands do appear (Fig. 4.3, trace C). This implies that, when curve fitting is performed on deconvoluted spectra instead of original ones, errors are certainly introduced when a too large K-factor has been selected.

Using a rather high K-factor (2.4-2.8), Garcia-Quintana et al. [49] resolved eight bands in the amide I profile of hydrated rhodopsin samples. However, if we combine adjacent bands, assigned to the same type of structural elements, a good agreement is observed (Table 4.3). The proportion of β-type structure (1623, 1639 and 1689 cm^{-1}) is very similar. The combined bands at 1674 and 1681 cm^{-1}(total area: 12±0.7 %) resolved by Garcia-Quintana et al., make
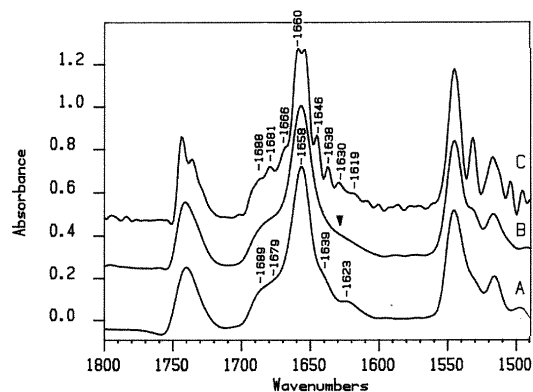
Figure 4.3: *Evaluation of the curve fitting procedure. A, measured absorbance spectrum after deconvolution (K=1.8); B, deconvolution (K=1.8) of a spectrum, composed of the 5 amide I components, obtained through curve fitting, shown in table 4.3; C, deconvolution of the same composed spectrum with 5 amide I components, but now with a higher K-factor (K=2.8). The band around 1658 cm^{-1} is split into 2 bands at 1660 and 1655 cm^{-1}. The arrowhead in trace B marks a minor fit imperfection.*

the same contribution as the single band we locate at 1679 cm^{-1}(area: 12±2 %), which is characteristic for β_{II}-type turns [7]. The main component in our spectra at 1658 cm^{-1}(area: 55±2 %) is largely due to the transmembrane α-helical elements, in agreement with other literature data [33, 63, 150].

As a first attempt to assign the amide I components to distinct parts of the protein, we used limited proteolysis with proteinase K or thermolysin to remove parts of the cytosolic domains, while leaving the overall structure and photochemical functionality (i.e. UV-vis spectrum and photolytical cascade) unaffected. Although the IR spectra even after deconvolution do not show that as clear (Fig. 4.4) as the curve-fitting, both treatments appear to strongly reduce the 1639-band in favour of the band around 1623 cm^{-1}(compare table 4.3 with table 4.4 and 4.5), while proteinase K also slightly reduces the α-helical contribution, as well as the band assigned to β_{II} -turns (Table 4.5).

The combination of the loss of a C-terminal protein fragment with a decrease in absorbance at 1639 and a concommittant increase in absorbance at 1623 cm^{-1} indicates in our opinion the presence of a double-stranded

$\tilde{\nu}(\text{cm}^{-1})$	$\Delta\tilde{\nu}_{\frac{1}{2}}(\text{cm}^{-1})$	A_{rel} (%)	Assignments
1620±1	34±1	28±3	β-strands
1633±1	13±1	2±1	β-turns
1657±1	16±1	55±1	mainly α-helical
1680±1	18±1	11±1	β_{II} -turns
1687±1	13±1	4±1	β-type

Table 4.4: *Amide I substructure composition of rhodopsin, after short treatment with thermolysin.*

β-sheet (1639 cm^{-1}) in this region which, after proteolytic removal of a C-terminal sequence, is converted to a single, extended β-strand (1623 cm^{-1}). The band around 1689 cm^{-1}, representing coupled vibrations within a β-strand [7, 99], remains constant. The additional loss of intensity at 1658 cm^{-1} by the action of proteinase K can be explained by the removal of 14 residues in a partly α-helical conformation from the third cytosolic loop,
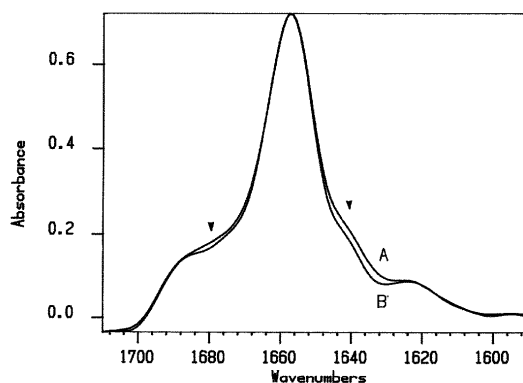
Figure 4.4: *Limited proteolysis of unbleached photoreceptor membranes. A, deconvoluted amide I profile of untreated membranes; B, same as A, after treatment with proteinase K. Loss of intensity is observed around 1640 and 1680* cm^{-1}. *Owing to the automatic scaling of the spectra, the loss of intensity sity at 1658* cm^{-1}*is obscured. Deconvolution is carried out according to Materials and Methods. The profile, obtained after thermolysin treatment, is omitted for clarity but only shows a 'dint' around 1640* cm^{-1}.

$\tilde{\nu}(\mathrm{cm}^{-1})$	$\Delta\tilde{\nu}_{\frac{1}{2}}(\mathrm{cm}^{-1})$	A_{rel} (%)	Assignments
1622±1	35±1	34±1	β-strands
1638±1	23±2	3±1	β-turns
1657±1	16±1	50±1	mainly α-helical
1679±1	16±1	9±1	β_{II} -turns
1689±1	12±1	5±1	β-type

Table 4.5: *Amide I substructure composition of rhodopsin, after treatment with proteinase K.*

between the transmembrane domains 5 and 6. Finally, the difference in the 1679 cm^{-1} absorbance between proteinase K and thermolysin treated samples suggests the presence of a β_{II} -turn in the C-terminal part of the protein, which is removed by proteinase K treatment. Since, following proteinase K treatment, most extra-membrane domains are present at the intradiscal side of the photoreceptor membrane, we assign the 1623 cm^{-1} band in the intact protein (Table 4.3) to β-type structure in the intradiscal part of the protein.

4.4 Discussion

4.4.1 Evaluation of curve fitting for secondary structural analysis

Our results indicate that the estimation of the secondary structure of proteins, from dehydrated samples, gives reliable results, when compared to analysis of hydrated samples by IR, NMR or X-ray crystallography. However several pittfalls remain, some of which also hold for analyses of proteins in the hydrated state.

1. In confirmation of earlier studies [140], the contribution of α-helices, calculated from the amide I band around 1658 cm^{-1}, may be slightly underestimated. This is especially true for very short helical fragments, which easily escape detection. In this case, the amide II component at 1545 cm^{-1}, which usually correlates very well with the α-helical content, seems to be of little help. The possible contribution of β_I - turns [7] also disturb the analysis of helical structures. In view of this

problem, structural analysis should start by assessing the types of β-structure, present in the protein under study. This problem was noticed before by Sarver an Krueger[141], who tried to analyze the amount of β-turns, using factor analysis. They showed that by combining all types of β-turns, no satisfactory results were found.

2. In our analysis, β-type structures are quantitated, using the strong bands below 1640 cm^{-1} only. The weak band around 1689 cm^{-1} not only represents β-strands but turn-structures as well and it remains a problem to separate these contributions. However, disregarding this band in a first approach only introduces a minor error, owing to its low relative intensity.

3. It is difficult to find operational parameters for unordered or 'random coil' structural elements. Owing to the flexible nature of these structural elements, these substructures may present themselves differently in solution and in the dehydrated state. Upon dehydration, they might e.g. convert into pseudo-helical segments, i.e. without intra-chain hydrogen bonds, or alternatively, generate a sequence of turn-structures, resulting in a contribution between 1660 and 1680 cm^{-1}. Although not conclusive, preliminary measurements on synthetic peptides and protein fragments, obtained by CNBr-cleavage ([138] and unpublished observations), indicate that the bands, associated with turn-structures, dominate the spectra, rather than the helical or β-type structures. A more detailed treatment of this problem is certainly needed, but is outside the scope of this thesis.

Recently, other groups have confirmed our findings that the overall secondary structure is usually preserved in dehydrated samples [138, 141, 126]. In cases where conformational changes, owing to dehydration, have been shown to occur, combined addition of a cryoprotectant (e.g. PEG) and a carbohydrate (typically sucrose or trehalose) maintains the native (tertiary) structure in the dehydrated state, and retains enzymatic activity after a lyophylization cycle [126]. On the other hand, it should be emphasized again that the dehydrated state allows quite reliable estimation of the β-strand contribution to a protein structure (with an error margin of <10 %). The same is true for α-helical structure and β-turns, providing the protein contains a large α-helical component (>30 %). furthermore dehydrated samples

allow much more easy sample handling and are devoid of potential solvent artifacts (e.g. solvent subtraction, incomplete ^{1}H/^{2}H exchange).

In general, further improvement in the estimation of protein secondary structure from FT-IR spectra, will come from pattern recognition methods, neuronal networks or partially least squares (PLS) analyses, since these methods practically are not limited by the finite spectral resolution.

Better discrimination between α-helices and β-turns in particular, will further increase the accuracy. However, this still requires detailed knowledge of the contributions of the individual components to the amide I and amide II band, in order to select a suitable reference set of proteins, which covers the full range of possible substructures.

4.4.2 The secondary structure of rhodopsin: Wet versus Dry

Although the high signal to noise ratio should permit higher K-factors, our impression is, that K-values above 2 do lead to overdeconvolution, an artifact which is often neglected in an effort to detect as many bands as possible. Using a rather high K-factor (2.4-2.8), Garcia-Quintana et al. [49] resolved eight bands in the amide I profile of hydrated rhodopsin samples. However, if we combine adjacent bands, assigned to the same type of structural elements, a good agreement is observed (Table 4.3). The proportion of β-type structure (1623, 1639 and 1689 cm^{-1}) is very similar. The bands at 1674 and 1681 cm^{-1}, resolved by Garcia-Quintana et al., together give the same contribution (total area: 12±0.7 %) as the single band we locate at 1679 cm^{-1}(area: 12±2 %), which is characteristic for β_{II} -type turns [7].

The main component in our spectra at 1658 cm^{-1}(area: 55±2 %) is largely due to the transmembrane α-helical elements, in agreement with other literature data [33, 63, 150]. Garcia-Quintana et al. [49] resolved this band in three components at 1649, 1656 and 1666 cm^{-1}, which they assigned to random coil, α-helix and α_{II}-helix or Ω-turn respectively. We think that these assignments can be questioned, since none of these subpeaks significantly shifts upon deuteration, as is usually only observed for less accessible α-helices. In fact, using higher K-factors (i.e. overdeconvolution), we can artificially 'resolve' our single, generated 1658-band into four bands at 1646, 1655, 1660 and 1666 cm^{-1}(fig. 4.2, trace C). Therefore, we think our results and those of Downer et al. [33], Haris et al. [63] and Stubbs et al. [150]

can be reconciled with those of Garcia-Quintana et al. [49] by assuming that the 1658 cm^{-1} peak represents rather 'normal' α-helical structure. Hence, we conclude that dehydrated photoreceptor membranes allow a good estimate of the secondary structure of rhodopsin, without the excessive data manipulation (i.e. solvent subtraction, smoothing, deconvolution) required for hydrated samples.

4.4.3   Refinement of the secondary structure of rhodopsin

Secondary structure analysis of proteins by means of curve fitting of amide I and amide II bands gains in value, when the absorption bands can be assigned to distinct parts of the protein under study. As a first approach for rhodopsin, we used limited proteolysis with proteinase K or thermolysin to remove parts of the cytosolic domains, while leaving the overall structure and photochemical functionality (i.e. UV-vis spectrum and photolytical cascade) unaffected.

The combination of the loss of a C-terminal protein fragment with a decrease in absorbance at 1639 and a concommittant increase in absorbance at 1623 cm^{-1} indicates in our opinion the presence of a double-stranded β-sheet (1639 cm^{-1}) in this region which, after proteolytic removal of a C-terminal sequence, is converted to a single, extended β-strand (1623 cm^{-1}). The band around 1689 cm^{-1}, reprepresenting coupled vibrations within a β-strand [7, 99], remains constant. The additional loss of intensity at 1658 cm^{-1} by the action of proteinase K can be explained by assigning a partly α-helical conformation to the third cytosolic loop, between the transmembrane domains 5 and 6, which is largely removed by proteinase K [27]. Finally, the difference in the 1679 cm^{-1} absorbance between proteinase K and thermolysin treated samples suggests the presence of a β_{II}-turn in the C-terminal part of the protein, which is removed by proteinase K treatment. Since, following proteinase K treatment, most extra-membrane domains are present at the intradiscal side of the photoreceptor membrane, we assign the 1623 cm^{-1} band to β-type structure in the intradiscal part of the protein.

The curve fitting analysis, presented above, opens up a way to refine the structural model for rhodopsin [117]. Our results agree with a β_{II}-turn in the C-terminal region, probably starting with the residues Asn$_{326}$Pro$_{327}$ [17]. This turn might connect 2 anti-parallel β-strands, which results in a β-

sheet. It has been shown [113] that the residues Cys_{322} and Cys_{323} are both anchored to the membrane by means of thio-palmitoyl chains. Since the palmitoyl chains are attached to adjacent residues, they are at opposite sides of the β-sheet plane, thereby orienting the β-sheet almost perpendicularly to the membrane surface. Thus Thr_{319} and Thr_{320} are placed in a shielded position, close to the membrane surface, which could explain why they are not phosphorylated by rhodopsin kinase, in contrast to Ser_{338} , Ser_{343}, Thr_{335} and Thr_{336} [97, 109, 116].

The presence of the structural elements we propose, is supported by computer assisted secondary structure predictions (chapter 2). The joint prediction results agree with a β-turn around position 325, flanked by β-strands, as well as with an α-helical segment around position 230 (third cytosolic loop), which is a major site or interaction with the G-protein, transducin [59]. Recently, high resolution NMR studies by Yeagle et al. [169, 170] have provided more solid support. A turn-helix-turn motif was proposed for the third cytoplasmic loop ($Lys_{231}-Arg_{252}$) and an anti-parallel β-sheet fragment, preceded by the β-turn mentioned above, was found in the C-terminus.

4.5 Conclusion

In conclusion, we have presented evidence that dehydration may sufficiently preserve protein structure to allow reliable estimation of their main structural features. This considerably simplifies sample handling and data analysis. Encouraged by these results, we have analyzed the global secondary structure of rhodopsin in dehydrated photoreceptor membranes. Our results do compare well with those obtained with hydrated samples. With the purpose of assigning structural elements, we repeated this procedure on proteolytically treated rhodopsin. The data present evidence for a double stranded β-sheet in the C-terminal domain and a helical segment in the loop, connecting the transmembrane domains 5 and 6. We tentatively assign a more complex β-type structure to the intra-discal protein domains, but this requires further analysis.

Chapter 5

Protein-lipid interactions

5.1 Introduction

The Na^+,K^+-transporting ATPase (EC 3.6.1.37) is the enzyme which maintains an electrochemical gradient of Na^+ and K^+ over cellular membranes, by means of active transport [131]. During a catalytic cycle, 3 Na^+-ions are pumped out of the cell and 2 K^+-ions are pumped into the cell. This process involves the phosphorylation of the enzyme by ATP. In a later stage of the cycle, inorganic phosphate is released again, eventually resulting in the net hydrolysis of 1 ATP into ADP and inorganic phosphate per cycle. This reaction requires Mg^{2+} as a cofactor (Fig. 5.1). The active form of the enzyme is a heterodimer ($\alpha\beta$), of which the α subunit (113 kDa) forms the catalytic centre and the β subunit (35 kDa, 55 kDa after glycosylation) plays a role in the stabilization of the K^+ occluded intermediate [92] and in targetting the enzyme to the cell membrane [51]. Both subunits are integral membrane proteins although there is still no consensus with regard to the number of transmembrane domains (8 or 10) of the α subunit [89].

Being an integral membrane protein, the transporting activity of Na^+,K^+-ATPase not only depends on ATP and cations, but is modulated by the phospholipid matrix as well. Thusfar, it has been established that negatively charged phospholipids yield the highest relative activities (see [30], but also [132] and [145]), whereas another member of the P-type ATPases: Ca^{2+}-ATPase, shows a preference for zwitterionic phospholipids [8]. Interestingly, with regard to the hydrophobic domains, these enzymes exhibit maximal activity when they are embedded in bilayers of certain thickness. In both
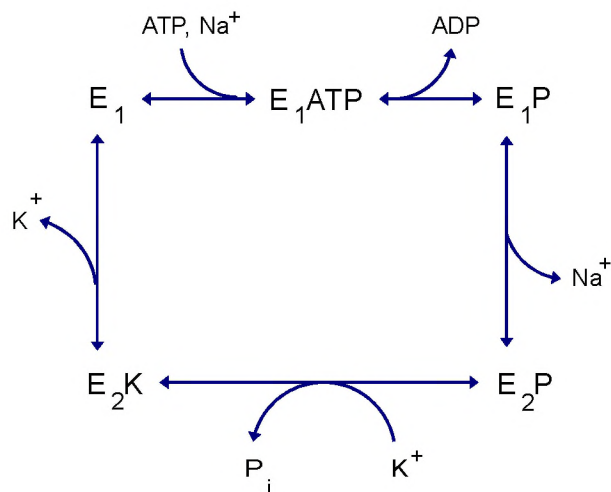
Figure 5.1: *Catalytic cycle of active countertransport of* Na^+ *and* K^+ *by* Na^+, K^+-*ATPase (simplyfied Albers-Post scheme).* $3\,Na^+$ *ions are exchanged by* $2\,K^+$ *ions, at the expense of 1 ATP.* E_1 *and* E_2 *denote the major conformational states of the enzyme.*

cases, the optimal membrane thickness is obtained with 20:1,20:1-PC [71, 72].

In order to gain more insight in the role of the lipid matrix in regulating the activity of Na^+, K^+-ATPase, we investigated the influence of a selected number of phosphatidylcholines, varying in unsaturation, on enzyme kinetic parameters. By changing the position and number of *cis* double bonds in lipid acyl chains, the thickness of a lipid bilayer can be changed. Since *any* effect of phospholipids on membrane embedded proteins implies a change in the interaction between these two components, we have characterized the interactions, occurring in purified rabbit kidney Na^+, K^+-ATPase proteoliposomes by means of the following methods: 1. FT-IR spectroscopy, using the temperature dependence of the symmetric CH_2 stretching vibration around $2850\ cm^{-1}$ and analysis of second derivative spectra of the carbonyl stretching region, between 1800 and $1500\ cm^{-1}$. These two approaches give information concerning the order of the lipid acyl chains and possible lipid-induced changes in the secondary structure of the enzyme, respectively, 2. isopycnic sucrose-gradient centrifugation, 3. electron microscopy and 4. determination of the $K_{0.5}$ for Na^+ -activated phosphorylation. The $K_{0.5}$ is defined as the Na^+ concentration, giving a half-maximal activation or phosphorylation level.

It appears that the interaction between protein and phospholipid markedly depends on the bilayer thickness of the phospholipid used, but qualitatively differs between low-melting, moderately saturated (16:0,18:1-PC) and highly unsaturated (18:3,18:3-PC) phospholipids. Whereas the acyl chain order of the first is disturbed by the enzyme, the perturbation of the latter is restrained indirectly through protein-protein interaction between the enzyme molecules. The unfavourable balance of hydrophobic lipid-protein interactions and polar protein-protein interactions enables the Na^+,K^+-ATPase to aggregate, causing an increased $K_{0.5}$ value for Na^+ in the enzyme's phosphorylation. Implications of these interactions for the practice of reconstitution are discussed in the light of the concept of hydrophobic matching.

5.2 Materials and Methods

5.2.1 Sample preparation and characterization

Rabbit kidney Na^+,K^+-ATPase was isolated according to the isopycnic zonal centrifugation method, developed by Jørgensen [74]. For centrifugation experiments and assay of the E_1 to E_2K transition, the enzyme was labeled with FITC (Sigma, St. Louis, MO) according to Karlish [75], except that the incubation time was 1.5 hours. Fluorescence measurements were carried out with a Shimadzu RF510. Determination of the overall hydrolytic activity (at 293 K) and the Na^+-stimulated phosphorylation reaction were performed as described before [145].

Liposome suspensions of selected phosphatidylcholines (39 mg/ml or 50 mM in water, Avanti Polar Lipids, Birmingham, AL) were prepared as described before [145]. All preparations contained 5.2 mM cholesterol. Phospholipids were handled under nitrogen or argon, whenever possible. According to TLC (HPTLC silica plates, chloroform/methanol/acetic acid/ water 40:10:10:1 v/v/v/v and chloroform/methanol/acetic acid/ water 40:15.3:6.3:-1 v/v/v/v, using iodine and phosphomolybdic acid staining), all phospholipids were chromatographically pure. The lipid composition is given in table 5.1.

In a typical reconstitution experiment, purified, non-labeled Na^+,K^+-ATPase (2 mg/ml in water) was mixed with freshly prepared liposomes in the required protein/lipid ratio. For activity assays of proteoliposomes, the water washing of Na^+,K^+-ATPase was omitted. After freeze-thawing three

acyl chain	Sph	PC	PI	PS	PE
Mole -%	18±1	36±1	13±1	5±1	28±1
14:0	1	3	1	1	24
16:0	31	39	16	16	9
16:1	5	3	4	3	3
18:0	13	5	27	27	6
18:1	16	29	12	27	18
18:2	13	15	12	14	9
18:3		1		1	1
20:4	6	3	18	9	27
22:0	3		1		<1
22:5	13	1	9	4	2

Table 5.1: *Phospholipid composition of* Na^+, K^+*-ATPase membrane sheets* *[122]. Sph, sphingomyeline.*

times, the mixture was sonicated under cooling during 5 minutes. This reconstitution procedure, which does not employ a detergent for solubilization of the enzyme, yields Na^+, K^+-ATPase proteoliposomes with retention of up to 50 % of the specific enzymatic activity. The protein to added lipid ratio was 1/1 by weight. In the case of 16:0,18:1-PC and 18:3,18:3-PC the ratios 1/3 and 1/10 were also applied, in order to test the range of the protein-lipid interaction. For the incorporation and activity assays (Table 5.2 and 5.3), protein to lipid mixing ratios of 1/50 by weight were used.

In order to verify the incorporation of Na^+, K^+-ATPase , the proteoliposomes (specific gravity, 1.03 g/ml) can be separated from the non-incorporated enzyme (specific gravity, 1.13 g/ml) by centrifugation through a 2 to 50 % w/v sucrose gradient, using fluorescence detection. The separation procedure could not be applied to the preparations destined for FT-IR spectroscopy or electron microscopy, owing to the absence of the fluorescent label in these preparations. Quantification of protein in the proteoliposome fraction was carried out after extraction of excess lipid with diethylether, according to Lowry in the detergent modification of Peterson [123]. Phospholid phosphate was determined according to Fiske Subbarow in the modification of Broekhuyse [14].

5.2.2 Electron microscopy

The liposomes and Na^+, K^+-ATPase proteoliposomes were characterized by electron microscopy, using 1. platinum-carbon shadowing of a dried suspension on a polyvinylaldehyde-coated copper grid (75 mesh); 2. Negative staining of the dried suspension with uranylacetate solution (2 %) and 3. freeze fracturing. Hereto the suspension was brought between 2 golden grids (150 mesh) and rapidly frozen in liquid propane. The samples were transferred to a BAF 400D freeze fracturing device (Balzer, Liechtenstein), fractured at 163 K and etched during 45 seconds. The fractured surfaces were coated with 2 nm platinum and 28 nm carbon, using an electron gun system. Finally, residual organic substances were removed by treatment with chromic acid (40 %). All preparations were examined with an EM 201 electron microscope (Philips, The Netherlands), employing an accelleration voltage of 60 kV.

5.2.3 FT-IR measurements

25 μl samples of liposomes or proteoliposomes were deposited as dehydrated films on AgCl windows (Fisher Scientific, Pittsburgh, PA), using iso-potential spin-drying [18]. For IR experiments, empty liposomes were not separated from the proteoliposome fraction. The films typically contained 1 nmole of Na^+, K^+-ATPase. Prior to measurements, the films were rehydrated with an imidazol buffer (pH 7.5; 25 mM) during 10 minutes. After this period, excess liquid was removed and the sample was covered with a second AgCl window and sealed with teflon tape. This sealing not only prevents dehydration of the sample but also protects the sample holder from severe corrosion by the AgCl windows. Unfortunately, its thermal conductivity is rather low, which, during an upward temperature scan results in a lower actual sample temperature than indicated by the temperature controller. By measuring the temperature profiles of dimyristoyl phosphatidylcholine (DMPC, T_m =299 K) and dipalmitoyl phosphatidylcholine (DPPC, T_m =314.5 K), we empirically established, that the actual sample temperature could be obtained by adding 2 K to the value indicated by the temperature controller. The reported temperatures are not corrected for this systematic error.

IR spectra were acquired in a stepwise temperature gradient from 278 to 328 K, with intervals of 2 K. The delay between each increment was 10 minutes and a stable temperature reading was obtained within 2 minutes.

The hysteresis in the downward temperature trajectory was 2–5 K.

FT-IR spectra were measured with a Cygnus 100 single beam spectrometer (Mattson, Madison, WI), equipped with a liquid nitrogen cooled, narrow band MCT detector and a computer controlled variable temperature cell (Specac, Orpington, UK). The sample compartment was continuously purged with dry nitrogen gas (20 l/min). Acquisition parameters: Resolution, 4 cm^{-1}; zero filling, twice; number of co-added interferograms, 128; moving mirror speed, 1.27 cm/s; wavenumber range, 4000–750 cm^{-1}; apodization function, triangle; time needed for acquisition and processing of a spectrum, less than 2 minutes; typical signal/noise ratio (2200–2000 cm^{-1}), better than 4×10^3.

5.2.4   FT-IR Data analysis

Data acquisition and analysis were performed with the EXPERT-IR software (Mattson). The use of hydrated membrane films permits to monitor the temperature dependent frequency shifts of the major lipid vibrational bands without baseline correction or spectral subtraction of the buffer. In a first approach we limited ourselves to the shift of the CH_2 symmetric stretching band around 2850 $cm^{-1}(\tilde{\nu}_s(CH_2))$ as a function of temperature.

Construction of interaction spectra [79], covering the entire spectral range, at selected temperatures, was attempted by subtraction of the IR spectrum of the Na^+, K^+-ATPase membrane sheets as well as the IR spectrum of the empty liposomes from the measured IR spectrum of the reconstituted proteoliposomes. The subtraction factors are approximated by the protein/lipid mixing ratios. This approach failed however, owing to varying baselines and slight differences in water content. Alternatively, the same information can be obtained by plotting the relative wavenumber shift of an individual spectral component, e.g. the methylene symmetric stretching band, as a function of temperature. When a mixture of 2 non-interacting components is made, the temperature profile of the mixture becomes a linear combination of the temperature profiles and the concentration of the individual components. The possible effects of *any* interaction can be revealed by calculating the relative frequency shift according to:

$$\Delta\nu_{LP} = \frac{\nu_{LP} - (x_P\nu_P + (1 - x_P)\nu_L)}{x_P\nu_P + (1 - x_P)\nu_L} \cdot 10^6 \qquad (5.1)$$

The subscript LP is encoding for proteoliposome, L for lipid alone and P for

the non-reconstituted, purified enzyme. $\Delta\nu_{LP}$ the frequency shift in ppm's (100 ppm represents a relative shift of about 0.3 cm^{-1}); ν_{LP} the frequency of $\tilde{\nu}_s(CH_2)$, observed in the prepared reconstituent; x_P , the weight fraction of the enzyme; ν_P , the $\tilde{\nu}_s(CH_2)$ frequency, observed in the Na$^+$, K$^+$-ATP-ase preparation and ν_L , the $\tilde{\nu}_s(CH_2)$ frequency, observed in the liposome preparation ($x_L = 1 - x_P$).

Fringes, resulting from internal reflection within the AgCl windows were removed by a deconvolution procedure (bandwidth was set to the separation between the fringes: 20 cm^{-1}; K-factor, 1.00; apodization, Bessel; lineshape, Lorentzian). The second derivatives of the filtered spectra were examined for the occurrence of changes in specific lipid or protein vibrational bands. Derivatization itself smoothes a slanting baseline and the broad water absorption bands around 3400 and 1650 cm^{-1}, which means that for qualitative analysis neither buffer subtraction nor baseline correction need to be made.

5.3 Results

5.3.1 Phospholipid dependent incorporation of Na$^+$,K$^+$-ATPase proteoliposomes

Sucrose density centrifugation offers a method to separate the non-incorporated enzyme from the desired proteoliposomes. By monitoring protein and phospholipid content throughout the gradient, an estimation of the incorporation of Na$^+$, K$^+$-ATPase in proteoliposomes can be made. Table 5.2 shows the percentage of incorporation in selected phosphatidylcholines, varying in saturation of the acyl chains. In this series, 16:0,18:1-PC seemingly behaves anomalously, since it is accompanied by 100 % protein incorporation though having a higher transition temperature (272 K) than 18:1,18:1-PC (251 K) with only 40 % incorporation. This suggests that mere membrane fluidity is no guarantee for a higher incorporation.

The influence of the changes in the lipid matrix on the kinetics of the Na$^+$-stimulated phosphorylation are listed in table 5.3.

These results demonstrate that, as expected, the enzyme activity depends on the membrane environment and lead to the preliminary conclusion that increasing fluidity of the membrane perturbs the tertiary structure of the enzyme, resulting in enhanced K$_{0.5}$(Na$^+$) values. This does not hold for 16:0,18:1-PC. However, it can be noted that 1. in the phosphoryla-

phospholipid	T_m (K)	Spec. Act. (μmol/mg·h)	Incorporation (%)
native		95±5	
18:0,18:1-PC	281.5	10	20±5
16:0,18:1-PC	272	30	100
18:1,18:1-PC	251	55	40
18:2,18:2-PC	220	20	90
18:3,18:3-PC	210	25	100

Table 5.2: *Specific hydrolytic activity (at 293 K) and incorporation of* Na^+,K^+-*ATPase in selected phosphatidylcholines. Native refers to the purified enzyme preparation.* T_m *values are obtained from literature [15]. The incorporation is represented as a percentage of protein, centered around the proteoliposome fraction (specific gravity, 1.03) upon sucrose gradient centrifugation. Protein to added lipid weight ratio, 1/50. All values ± rounded SD (n=2).*

tion reaction 16:0,18:1-PC is the only phospholipid showing a Na^+-sensitivity ($K_{0.5}(Na^+)$-value) comparable to that of the native enzyme, whereas 2. in the E_1 to E_2K transition, 16:0,18:1-PC is the phospholipid causing the highest $K_{0.5}(K^+)$ and $K_i(Na^+)$ values (data not shown). The difference between 1. and 2. is, of course, the presence of ATP in the phosphorylation analysis and its absence in the conformational transition assay (FITC prohibits

phospholipid	EP(max) (nmole/mg)	$K_{0.5}(Na^+)$ (mM)	nH_{Na^+}
native	1.90±0.05	0.3±0.1	1.3±0.1
16:0,18:1-PC	2.50	0.2	1.0
18:0,18:1-PC	0.65	0.8	1.0
18:1,18:1-PC	0.85	1.2	1.0
18:2,18:2-PC	0.85	1.9	1.1
18:3,18:3-PC	0.55	3.4	0.8

Table 5.3: *Enzyme kinetical parameters of* Na^+ *-dependent phosphorylation. The maximum phosphorylation level,* $K_{0.5}(Na^+)$ *and the Hill coefficient,* nH_{Na^+}, *are listed as a function of the phospholipid composition. Protein to lipid weight ratio, 1/50 or 66 μmole/mg. All values ± rounded SD (n=2).*

ATP binding), plus the fact that ATP causes opening of cation channels within the enzyme. Moreover, it may be that 16:0,18:1-PC is among the favourite phospholipids to allow this channel opening process to occur. A similar ATP/phospholipid antagonism, related to dissociation/association of the constituent enzyme $\alpha\beta$ subunits, has been reported for bovine brain PS [100].

5.3.2 Electron microscopy

The freeze-fracturing results of the Na^+,K^+-ATPase microsomal fraction were compared with those, obtained by Van Winkle et al. [159], and showed a good correlation with regard to vesicle size and protein distribution.
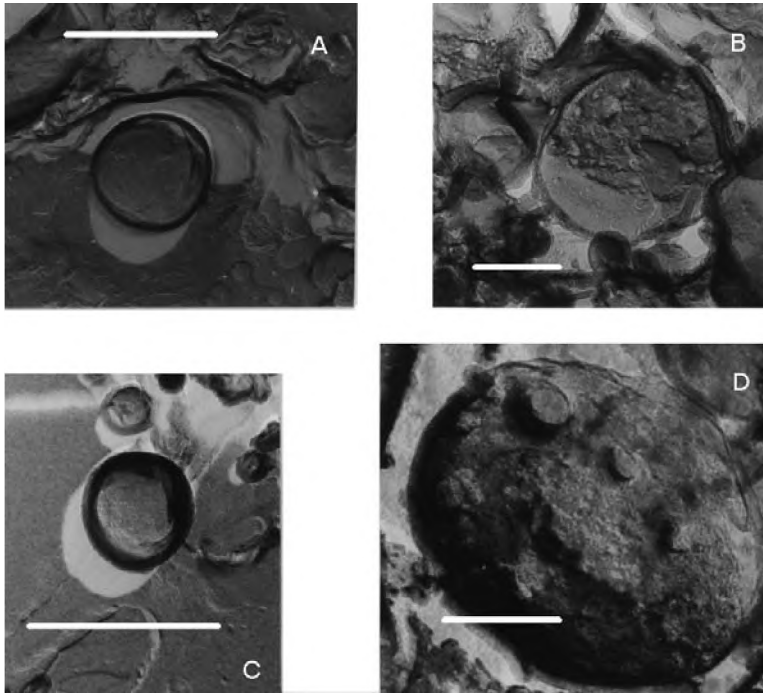

Figure 5.2: *Electron micrographs of* Na^+,K^+-*ATPase proteoliposomes, taken from freeze-etched preparations. A, empty vesicle of 16:0,18:1-PC; B, Na^+,K^+-ATPase in 16:0,18:1-PC (1/1 w/w). The white particles within the vesicle indicate the presence of the protein; C, empty vesicle of 18:3,18:3-PC; D, Na^+,K^+-ATPase in 18:3,18:3-PC (1/1 w/w). The bar represents 200 nm.*

Direct Pt/C-shadowing as well as freeze-fracturing experiments reveal that the empty liposomes of the preparations studied have vesicle diameters of approximately 100 ± 50 nm (Fig. 5.2A and C). The proteoliposome diameters of Na^+, K^+-ATPase incorporated in 16:0,18:1-PC and 18:3,18:3-PC are 300 ± 100 nm (Fig. 5.2B and D).

Owing to the larger protein to lipid ratios, used in our studies, this value is larger than the value (about 100 nm) found by Marcus et al. [94]. In the case of mixing Na^+, K^+-ATPase with 18:0,18:1-PC, no vesicles of this size nor with a rough surface could be found using the freeze-fracturing technique, thereby confirming the centrifugation experiments, i.e. incorporation of Na^+, K^+-ATPase hardly takes place in this phospholipid. Although we suggest that highly unsaturated phospholipids may give rise to protein aggregation (see discussion), no indication of such a phenomenon (larger particle size) was found when preparing the samples at ambient temperature.

5.3.3 FT-IR spectroscopy

It appears that Na^+, K^+-ATPase can only be incorporated effectively in relatively fluid phospholipids, which undergo gel to liquid crystalline transitions well below 273 K. Normally, protein/lipid interactions are studied by monitoring the effect of protein incorporation on the phase transition temperature, T_m. In this study we were also interested in the relation between lipid-protein interactions and enzyme activity, taking place between 273 and 310 K. Therefore, we studied the temperature profiles of the (proteo)liposomes above 278 K, i.e. in the range where the lipids mainly exist in the liquid crystalline phase. In a first approach, we confined ourselves to the analysis of temperature curves of the CH_2 symmetric stretching band ($\tilde{\nu}_s(CH_2)$) [57], representing the acyl side chains in the liposomes and thus the major part of the phospholipid molecule that is in contact with an integral membrane protein. This band shifts to higher wavenumbers when the membrane fluidity increases. Incorporation of Na^+, K^+-ATPase reduces this upshift to various extents. Figure 5.3 shows the temperature profiles, resulting from incorporation of Na^+, K^+-ATPase in 16:0,18:1-PC liposomes. The band frequencies range from about 2852.5 to 2854 cm^{-1} and a maximum downward shift of about 0.5 cm^{-1} is observed by incorporating one weight equivalent of Na^+, K^+-ATPase. By decreasing the protein/lipid ratio, the protein induced shift of the $\tilde{\nu}_s(CH_2)$ band decreases and the temperature profile now returns to that of the empty vesicles. Na^+, K^+-ATPase incorporated in 18:3,18:3-PC
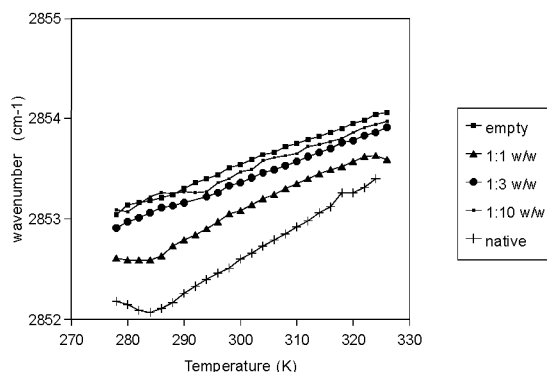
Figure 5.3: *Temperature dependence of $\tilde{\nu}_s$(CH$_2$) in the fluid phase of 16:0,18:1-PC-reconstituted* Na$^+$,K$^+$-*ATPase. Protein to lipid mixing ratios (w/w) are indicated at the right. 'empty' refers to the pure liposomes.*

shows a more or less similar behaviour at increased frequencies of 2853–2858 cm^{-1}(Fig. 5.4). The maximum downward shift is up to 4 cm^{-1} instead of the 0.5 cm^{-1}, observed for 16:0,18:1-PC.

In order to compare the results obtained with the various phospholipids quantitatively, we plotted the relative wavenumber shift as a function of temperature, according to equation 5.1 [79]. The results of these calculations are presented in figure 5.5 (Na$^+$,K$^+$-ATPase in 16:0,18:1-PC at various mixing ratios) and in figure 5.6 (Na$^+$,K$^+$-ATPase in 18:3,18:3-PC at various mixing ratios).

Surprisingly, these plots now show different behaviour for 16:0,18:1-PC (positive difference), i.e. a promoted methylene vibration and 18:3,18:3-PC (negative difference), i.e. a restrained methylene vibration relative to the algebraic sum of the frequencies. Considering the experimental conditions and the wavenumber accuracy of FT-IR instruments, relative differences between ±100 ppm are interpreted as 'no interaction'. In this respect, the crossing-over of the curves, observed in figure 5.4 and figure 5.6 can be disregarded, since it occurs in a range where no apparent interaction between the enzyme and 18:3,18:3-PC is found. At lower protein/added lipid mixing ratios (1:3 and 1:10 respectively), the curves nearly run parallel, but at reduced relative differences, indicating that the interactions rapidly become
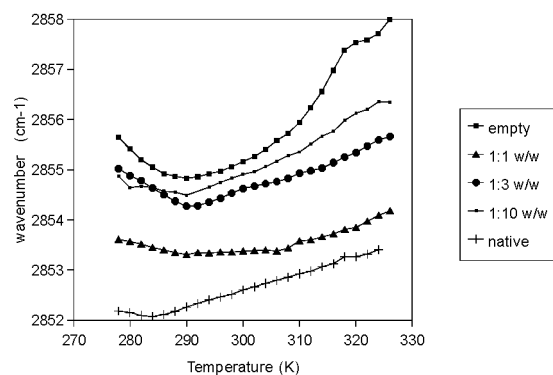
Figure 5.4:   *Temperature dependence of $\tilde{\nu}_s$(CH$_2$) in the fluid phase of 18:3,18:3-PC-reconstituted* Na$^+$, K$^+$-*ATPase . Protein to lipid mixing ratios (w/w) are indicated at the right. 'empty' refers to the pure liposomes. The cross-over point in the 1:10 and 1:3 curves at 283 K, indicates an incomplete thermal equilibration at the start of the 1:10 curve (see text).*
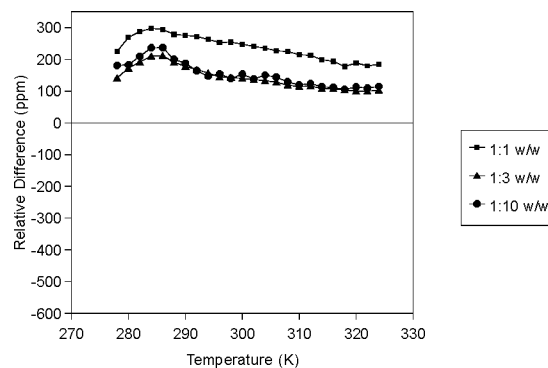
Figure 5.5:   *Interaction of* Na$^+$, K$^+$-*ATPase and 16:0,18:1-PC. The relative bandshift of $\tilde{\nu}_s$(CH$_2$) is plotted as a function of temperature. This value is obtained by subtracting the linear combination of the individual components (i.e. no interaction) from the measured value. This result is ratioed against the linear combination. Protein to lipid mixing ratios are given in the right hand box.*

Figure 5.6: *Interaction of* Na^+,K^+-*ATPase and 18:3,18:3-PC. The relative bandshift of $\tilde{\nu}_s$ (CH$_2$) is plotted as a function of temperature, in the same way as in figure 5.5.*

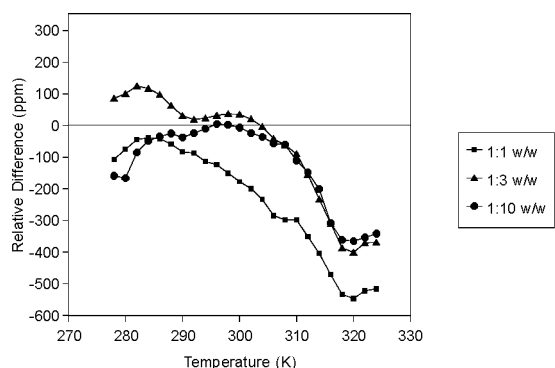weaker at decreasing protein concentrations. It is also noted that figure 5.5 and 5.6 show two distinghuished regions, i.e. around 283 K and around 310 K. At 283 K, both protein-lipid systems exhibit a maximum in the curve. At 310 K however, the protein-lipid interactions between Na^+,K^+-ATPase and 16:0,18:1-PC become weaker whereas the interactions between Na^+,K^+-ATPase and 18:3,18:3-PC develop a negative maximum.

Figure 5.7 summarizes the results for the interaction of Na^+,K^+-ATPase with the various phospholipids at a protein/lipid mixing ratio of 1:1. The phospholipids of low or intermediate unsaturation show relative differences around 0 ppm, i.e. no apparent interaction. This can be due to inefficient enzyme incorporation (18:0,18:1-PC) or to reaching the average lipid composition in the enzyme preparation (e.g. 18:1,18:1-PC), which makes the interaction of the enzyme with the added phospholipids indiscernible from those with the 'native' lipids, surrounding Na^+,K^+-ATPase in the purified enzyme fraction.

5.3.4 Identification of lipid-protein interactions

Having established that different lipid-protein interactions do occur, as monitored by the relative shift of the methylene symmetric stretching frequency, we subsequently tried to analyze these interactions in more detail, by exam-
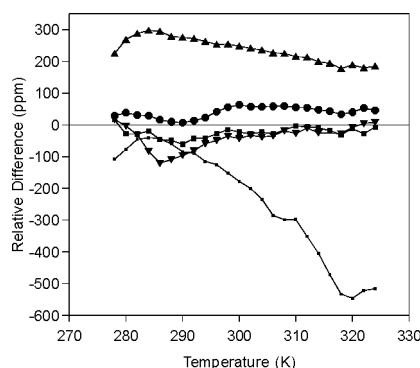
Figure 5.7: *Comparison of interactions in selected proteoliposomes (protein to added lipid weight ratio is 1:1 w/w). The relative bandshift of $\tilde{\nu}_s$(CH$_2$) is plotted as a function of temperature (see also figure 5.5 and 5.6). Na$^+$,K$^+$-- ATPase in 16:0,18:1-PC (positive curve) and 18:3,18:3-PC (negative curve) show the largest deviations. The other phosphatidylcholines show less pronounced interaction.*

ining the second derivative spectra at 283 and 310 K. Selection of these two temperatures was based on the maxima and minima in the relative frequency differences (Fig. 5.7). The second derivative spectra of Na$^+$,K$^+$-ATPase, reconstituted in 16:0,18:1-PC are shown in figure 5.8 at 283 K and 310 K respectively.

Upon reconstitution of Na$^+$,K$^+$-ATPase in 16:0,18:1-PC, the carbonyl stretching mode region (Fig. 5.8 left) shows the free and hydrogen-bonded lipid ester carbonyl bands at 1739 and 1719 cm^{-1} (shoulder) respectively [88, 11]. Below 1700 cm^{-1}, the amide I components of the peptide backbone of the enzyme are disclosed: 1684 cm^{-1}, β-turns; 1656 cm^{-1}, α-helices (possibly plus H$_2$O signal) and 1635 cm^{-1}, β-sheets [101, 7]. Apart from changes in intensity, no major band shifts in this region are observed in the spectra of the reconstituents.

At 310 K, only the non-bonded ester carbonyl band (Fig. 5.8 right) gives rise to a minute downshift and the hydrogen bonded ester band broadens.

Although hardly visible at a first glance, the situation is quite different when Na$^+$,K$^+$-ATPase is incorporated in 18:3,18:3-PC (Fig. 5.9). The most remarkable effect upon reconstitution is the shift of the band at 1635 to 1630
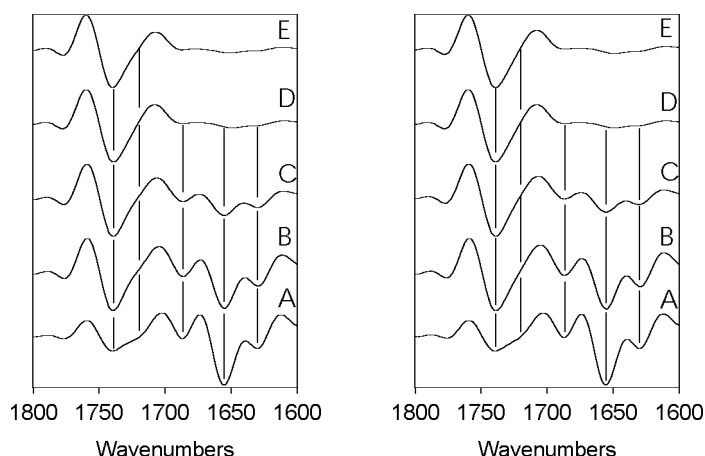
Figure 5.8: *Second derivative spectra of* Na^+, K^+*-ATPase reconstituted in 16:0,18:1-PC. Left panel, T=283 K; right panel, T=310 K. A, purified enzyme fraction; B, protein/lipid ratio 1/1; C, protein/lipid ratio 1/3; D, protein/lipid ratio 1/10; E, pure 16:0,18:1-PC.*

cm^{-1} in the spectra, acquired at 283 K (Fig. 5.9 left, traces B and C versus trace A). Moreover, the intensity of this band is stronger as compared to the α-helix band. The downshift and the change in intensity of this band, which is associated with β-type secondary structural elements, indicates that the secondary structure of the enzyme changes dramatically upon reconstitution in 18:3,18:3-PC. The observed shift is independent of the protein/lipid mixing ratio. The accompanying amide II component is expected to be relatively weak [7] and, accordingly, no significant change around 1555 cm^{-1} is found (not shown).

At 1740 and 1720 cm^{-1} again, the lipid ester carbonyl stretching bands are found. At 310 K, in the carbonyl stretching region (Fig. 5.9 right), the free ester band is slightly downshifted, whereas the hydrogen-bonded lipid ester carbonyl band broadens. The β-sheet band at 1630 cm^{-1} now shifts back to 1634 cm^{-1} and the intensity ratio of the bands is restored.

When comparing the carbonyl stretching region of the IR spectra of all prepared combinations of Na^+, K^+-ATPase with various phospholipids (protein/lipid mixing ratio of 1:1), the combinations which result in less efficient incorporation of the enzyme, i.e. 18:1,18:1-PC and, to some extent, 18:2,18:2-
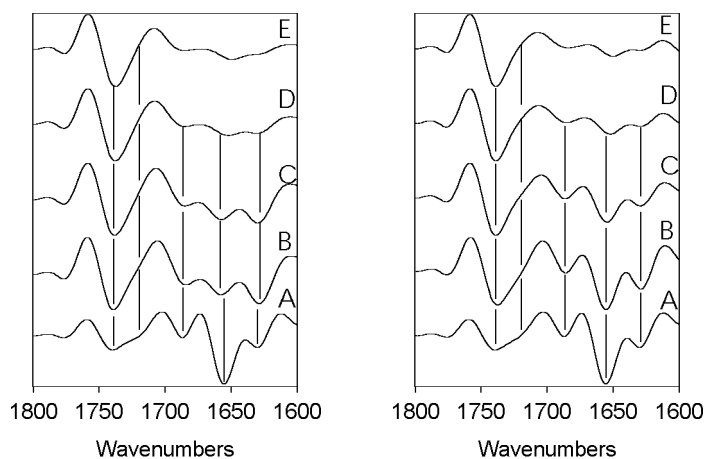
Figure 5.9: *Second derivative spectra of* Na^+,K^+-*ATPase reconstituted in 18:3,18:3-PC. Left panel, T=283 K; right panel, T=310 K. A, purified enzyme fraction; B, protein/lipid ratio 1/1; C, protein/lipid ratio 1/3; D, protein/lipid ratio 1/10; E, pure 18:3,18:3-PC.*

PC exhibit no downshift of the non-bonded ester carbonyl band, going from 283 to 310 K (not shown). It is noted that these phospholipids do not exhibit apparent hydrophobic interaction with the protein (Fig. 5.7).

5.4   Discussion

5.4.1   Phospholipid preference of Na^+,K^+-ATPase

The picture that emerges in relation to membrane bound ATPases and their preference to certain classes of phospholipids is that a fluidity, corresponding to a gel to liquid crystalline phase transition below that of 18:0,18:1-PC (281.5 K) is essential for reconstitution. However, a successful reconstitution is insufficient for maintaining enzymatic activity. For instance, 14:1,14:1-PC and 16:1,16:1-PC, although fulfilling the criterion of a low T_m (237 K or lower) give low ATPase activities [94]. The same holds for the polyunsaturated 18:2,18:2-PC (T_m= 220 K) and 18:3,18:3-PC (T_m= 213 K), but not for the long chain 20:1,20:1-PC and 22:1,22:1-PC ($T_m$of 269 K and 286 K respectively), the latter two of which sustain high levels of activity. In other words, the phase transition temperature of the phospholipid matrix

should be low (less than 281.5 K) but not too low (greater than 250 K). This restricts the phosphatidylcholines, supporting enzyme activity to a rather limited number.

Similar experience is encountered with sarcoplasmic reticulum (SR) Ca^{2+}-ATPase, where from the semi-unsaturated PC series (i.e., all carrying palmitoylate in the sn-1 position), only 16:0,18:1 and 16:0,18:2-PC (T_m of 270 K and 253 K respectively) sustain ATPase activity commensurate with that of purified SR [96]. The more strongly unsaturated higher homologues 16:0,20:4 and 16:0,22:6-PC (T_m of 252 K and 270 K) offer only 3-6 % of the specific activity, in line with data on the influence of increasing unsaturation on the Na^+, K^+-ATPase activity (see above). Phase transition temperatures of these phosphatidylcholine-members are in the range of the optimal activity-sustaining PC species, suggesting that the bilayer thickness and the position of the double bond are governing activity [71, 72]. These parameters also control the fluidity of the membrane.

When we take a look at the native phosphatidylcholines (table 5.1), one observes that 39 mole-% of the constituent fatty acids is 16:0 and 44 mole-% is 18:1+18:2 with little 18:0 and 18:3 [122]. Besides the phosphatidylcholines, only phosphatidylethanolamine (PE, 28 mole-%) bearing 18:1 (18 %) acyl chains, is a possible candidate for supporting ATPase activity. This suggests that under natural conditions, the enzyme is allowed to select a sufficient amount of phosphatidylcholine for regulating its activity.

A remarkable feature, confirmed by studies on sarcoplasmic reticulum Ca^{2+}-ATPase [98, 3], is the opposite effect exerted by the enzyme on the phospholipids. Phosphatidylcholines with one unsaturated and one saturated acyl chain yield an increased $\tilde{\nu}_s(CH_2)$ frequency, whereas $\tilde{\nu}_s(CH_2)$ of phosphatidylcholines with two polyunsaturated acyl chains is restricted. Conversely, the latter phospholipids appear to perturb the enzyme tertiary structure, as is evident from the increased half-maximally activating cation concentrations in the Na^+-activated phosphorylation.

5.4.2 Classification of interactions in proteoliposomes

The acyl chains constitute the largest part of phospholipid molecules and, allegedly, they form the major site of direct Van der Waals interaction with integral membrane proteins. The large extramembrane domains of the transporting ATPases may also bind to the polar headgroups of lipids through hydrogen bonding and salt bridges. In principle, these extramembrane do-

mains are also sites for direct protein-protein interactions. According to the mattress model [104, 105] for lipid-protein interactions, the Van der Waals interactions play the most important role in the lateral distribution of proteins in a lipid bilayer. The main parameter determining the strength of these interactions is the hydrophobic thickness of the lipid bilayer in relation to the hydrophobic thickness of the protein (Fig. 5.10).
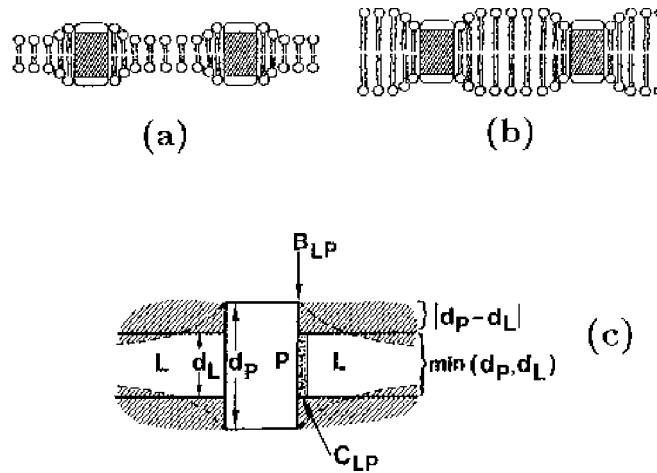
Figure 5.10: *The mattress model for protein-lipid interactions. Transmembrane protein domains are approximated by cylinders, disturbing the lipid bilayer. (a), protein length greater than bilayer thickness; (b), protein length less than bilayer thickness; (c), parameters, determining the mismatch:* d_L, *undisturbed lipid bilayer thickness,* d_P, *length of transmembrane domain,* C_{LP}, *stabilizing hydrophobic interaction parameter, depending on the minimum thickness of either the lipid bilayer or the protein;* B_{LP}, *disturbing interaction parameter, depending on the absolute value of the difference between the bilayer thickness and protein thickness. In this model extramembrane protein-lipid interactions are not taken into consideration (Adapted from [105]).*

However, if the interactions are too weak (thin bilayer), lipid-mediated protein-protein interactions and, possibly, the direct protein-protein interactions may become predominant, eventually leading to protein aggregation

and hence, loss of enzymatic activity. The chance that these attractive, polar protein-protein interactions can occur is expected to be larger in large proteins, such as Na^+,K^+-ATPase which, according to most recent neural network-based predictions of transmembrane domains [134, 135], has only 14–18 % of its amino acids inserted in the lipid bilayer, including the β subunit.

The second derivative spectra of Na^+,K^+-ATPase, reconstituted in 18:3,-18:3-PC actually show this behaviour (Fig. 5.9). At 283 K, the band normally at 1635 cm^{-1}, most probably representing β-type structures in extramembrane domains of the enzyme, is downshifted, thereby indicating that, at least, the protein structure has changed. In addition, the shift is independent of the protein/lipid mixing ratio, thereby confirming that protein-protein interactions are responsible for this shift. As a result of this attractive force, lipid separation may occur, as indicated by the relatively small frequency shift at lower temperatures (no protein-lipid interaction). By increasing the temperature, the protein-protein interactions are deminished, simultaneously creating the possibility for hydrophobic interactions between Na^+,K^+-ATPase and 18:3,18:3-PC, giving rise to an enhanced negative relative shift. According to our EM studies, at about 293 K, these hydrophobic interactions are apparently strong enough to preclude protein aggregation.

As deduced from the absence of the shift of the band at 1635 cm^{-1}(Fig. 5.8), Na^+,K^+-ATPase, reconstituted in 16:0,18:1-PC, maintains its native β-type structures and, coupled to that, high enzymatic activity. In this case, insertion of the enzyme in the more ordered bilayer (indicated by a lower $\tilde{\nu}_s(CH_2)$), results in the pushing apart of lipid molecules, thereby increasing the distance between the phospholipids as well as between protein molecules. In accordance with this phenomenon, the interaction plot shows a positive relative shift (Fig. 5.5).

The interaction plots of the intermediately unsaturated phosphatidylcholines are more difficult to interpret since in these cases the effects of the lower reconstitution efficiency and cancelling of interactions in the formed proteolipid complexes are indiscernible.

5.4.3 Multiple double bonds and bilayer thickness

The current model for lipid-protein interactions, the mattress model, assumes that insertion of a protein in a lipid bilayer introduces a local disturbance of

the bilayer structure, depending on the thickness of the undisturbed bilayer and the hydrophobic thickness of the protein. In our present study, we analyzed the influence of multiple double bonds in the lipid acyl chains on the structure and activity of Na^+, K^+-ATPase-containing membranes. Simple goniometric calculations, confirmed by experimental determinations [87], indicate that a *cis* double bond leads to the shortening of a hydrocarbon chain by about 0.9 Å, whereas addition of a methylene group leads to a lengthening by about 1.3 Å. Apparently, introduction of up to 3 *cis* double bonds results in a more flexible and thinner bilayer, thus increasing the hydrophobic mismatch between protein and lipid.

The palmitoyl (16:0) and linolenoyl (18:3) groups display about equal mismatch as compared to the 20:1 acyl chain, and this mismatch may give optimal incorporation (table 5.2). This principle explains the non-parallel occurrence of fluidity and protein incorporation, since the lipid phase transition temperature not only depends on the length of the acyl chains but also on the number and position of *cis* double bonds. In this respect, a remarkable feature of 16:0,18:1-PC came to our notice. While lacking 4 methylene groups in one of its acyl chains with respect to 20:1,20:1-PC acyl chains, it would exhibit a hydrophobic mismatch, as reflected by an increased $K_{0.5}(Na^+)$ value. Yet, $K_{0.5}(Na^+)$ in the phosphorylation mimics that of the native enzyme, which we explained assuming that ATP dependent cation binding and release processes remain unaffected. Conversely, this might imply that other phospholipids, which influence $K_{0.5}(Na^+)$ values in the phosphorylation process as well, do influence these binding and unbinding events, which is a problem that is still open to investigation.

The impact of hydrophobic mismatch on the enzyme's partial and overall activities is quite complicated, since this study has shown that certain phospholipids (16:0,18:1-PC) alter some partial reactions (cation affinity in the E_1 to E_2K transition), while leaving the Na^+ and ATP dependent phosphorylation relatively unaffected. A more detailed study of the effects of the acyl chain length and unsaturation on different other partial reactions (E_1P to E_2P transition, dephosphorylation) may shed some light on this complicated matter. The finding that ouabain sensitivity (I_{50}) and the relative unsaturation of phospholipids exhibit a linear relationship, may serve as an example [1].

5.5 Conclusion

We have characterized the types of lipid-protein interactions, occurring between Na^+, K^+-ATPase and selected phospholipids in the fluid crystalline phase, by means of FT-IR spectroscopy and we have demonstrated that these interactions differ both quantitatively and qualitatively, depending on the degree of unsaturation of the phospholipid. Na^+, K^+-ATPase disturbs the tight packing of saturated phospholipids whereas it confers a relatively higher degree of ordering to highly unsaturated phospholipids. As a result of a shorter acyl chain length, the highly unsaturated phospholipid mutually forces the transmembrane segments of the enzyme to compensate its need for hydrophobic interaction by self-aggregation, leading to deteriorated enzymatic activities such as the phosphorylation reaction.

Chapter 6

Peptide succinimide derivatives

6.1   Introduction

During their lifetime, proteins may lose their specific structure and function, due to aging processes. One of these processes involves nonenzymatic degradation, which occurs most likely at asparaginine or aspartic acid residues in peptides and proteins. The side chains of these residues are particularly susceptible to intramolecular succinimide formation, leading to isomerization, racemization and, in the case of asparaginyl residues, to deamidation and peptide bond cleavage as well. Figure 6.1 depicts the formation of a succinimide (L-Imide) from an aspartyl-containing peptide (L-Asp), which is subsequently hydrolyzed to the racemized aspartyl peptide (L-Asp and D-Asp) and the iso-aspartyl peptide (L-IsoAsp and D-IsoAsp).

   The propensity to form five-membered succinimide rings in native proteins largely depends on the local conformation around the residue and to a lesser extent on the subsequent amino acid residue [19, 52, 168]. Especially proteins, containing the asparaginylglycyl or the aspartylglycyl sequences, which are prone to form succinimide rings, have been studied with regard to succinimide-linked reactions. Among these proteins are ACTH [5] , human methionyl growth hormone [153] , calmodulin [73] and ribonuclease A [31]. In αA-crystallin, the major protein of the vertebrate eye lens, it was shown that deamidation, isomerization, racemization and peptide bond cleavage oc-
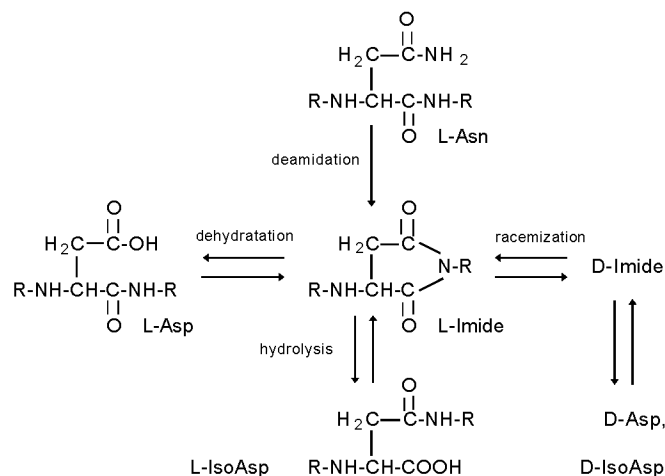
Figure 6.1: *Formation of a succinimide (L-imide), starting from an aspartyl peptide (L-Asp) or an asparaginyl peptide (L-Asn). Upon hydrolysis, a mixture of the racemized peptide (L-Asp and D-Asp) and the isoaspartyl peptide L-IsoAsp and D-IsoAsp) are formed.*

cur at Asn_{101} via imide ring formation [160]. αA-Crystallin contains Asp-Gly, Asp-Ala and Asp-Ser sequences as well. Only Asp_{151}, which is followed by an alanyl residue and is located in a flexible region of the protein, also exhibits pronounced racemization [58].

In this chapter, a study is described on the formation of succinimides in aspartylalanyl-containing peptides, which correspond with the sequence around Asp_{151} in bovine αA-crystallin. This study directly demonstrates and characterizes the formation of a succinimide intermediate from these aspartyl-containing peptides. FT-IR spectroscopy is used to detect the formation of the succinimide derivatives in small peptides since this class of compounds gives rise to characteristic absorption bands in the IR spectrum, which are easily distinguished from the bands originating from the untreated, native peptide. Raman spectroscopy has been used to support several assignments made on the basis of the FT-IR spectra.

6.2 Materials and methods

6.2.1 Sample preparation

Aspartylalanine and its isomer aspartyl-β-alanine, were purchased from Bachem (Bubendorf, Switzerland). Valinylaspartylalanylglycine was a generous gift from prof. dr. G.I. Tesser (Dept. Org. Chem., University of Nijmegen). According to TLC, these peptides were chromatographically pure (H-Asp-Ala-OH: R_f=0.17; H-Val-Asp-Ala-Gly-OH: R_f=0.20 in butanol/acetic acid/water 4:1:1 v/v/v, ninhydrin staining). ^2H_2O(deuteration better than 99.75 %) and Me_2SO were purchased from Merck (Darmstadt, FRG) and Fluka (Buchs, Switzerland) respectively.

To prepare the succinimide derivatives, aspartylalanyl containing peptides (0.5-1.0 mg) were acidified with 1 ml-0.1 N HCl, lyophilized and heated during at least 24 hours according to described procedures [90]. Starting with H-Asp-Ala-OH, this procedure yielded a single product with R_f=0.25. No residual starting material was detected. During heating of acidified H-Val-Asp-Ala-Gly-OH, the succinimide (R_f=0.37) partly hydrolyzed to form the starting material and 2 new products with R_f=0.24 and R_f=0.15. By comparison with authentic dipeptide samples, these products were identified as H-Val-Asp-OH and H-Ala-Gly-OH respectively. Since succinimide signals appear well separated from other peptide signals in the IR spectrum, no attempt was made to isolate the succinimide derivative of the tetrapeptide. After heating, the samples were taken up in 0.2 ml water and deposited rapidly as a film on IR-transparent AgCl windows, using the iso-potential spin drying method [18]. This procedure, originally developed for the preparation of membrane films, proves also very useful for measuring water-soluble protein samples in the solid state (this thesis, chapter 4).

6.2.2 FT-IR measurements

FT-IR spectra, measured in transmission mode, were obtained with a Mattson Cygnus 100 single beam spectrometer, equipped with a liquid nitrogen cooled, narrow band MCT detector and interfaced to a microcomputer. The sample compartment was continuously purged with dry nitrogen gas (20 l/min). IR spectra of heated dipeptides in Me_2SO or ^2H_2O solution were taken at ambient temperature with a liquid sample cell (Specac, Orpington, England), equipped with a 25 μm teflon spacer and AgCl windows.

Acquisition parameters: Resolution, 2 cm^{-1}; number of co-added interferograms, 1024 (256 in the case of liquid samples); moving mirror speed, 2.53 cm/s; wavenumber range, 4000–750 cm^{-1}; apodization function, triangle; time needed for acquisition and processing of a spectrum from 1024 interferograms, 9 minutes; typical signal/noise ratio (2200–2000 cm^{-1}), better than 4×10^3.

6.2.3   Raman measurements

Raman spectra were obtained with an extended Perkin Elmer 1760 X FT-IR spectrometer equipped with a liquid nitrogen cooled InGaAs detector. Spectra were not corrected for the instrumental response. Acquisition parameters: Resolution: 8 cm^{-1}; number of scans, 128; NdYAG laser power, 400 or 500 mW; acquisition time, 11 minutes. The frequency domain was calibrated with a Raman spectrum of benzene, and wavenumbers are reported with an accuracy of ± 1 cm^{-1}.

6.2.4   Data treatment

Data acquisition and analysis were performed with the EXPERT-IR (Mattson) or SpectraCalc (Galactic Industries) software. Solvent subtraction was applied where necessary. No baseline correction was performed for the absorption by the AgCl windows, which may vary in quality.

Fourier self-deconvolution parameters [76]: Bandwidth, 16 cm^{-1}; K-factor, up to 2.4; apodization function, $\sin^2(x)/x^2$; lineshape function, Lorentz. Second derivative spectra were smoothed over 13 datapoints [142].

The imide band parameters were derived from curve fitting analysis of the absorbance spectra between 1825 and 1625 cm^{-1}, using deconvoluted or second derivative spectra for determination of the number and position of the bands. The quality of the fitted spectrum was judged by the residual integrated intensity and by deconvoluting the generated spectrum with the same parameters as the measured spectrum (Kappers, M. and Van der Maas, J.H., personal communication).

6.3 Results and discussion

6.3.1 The succinimide bands are distorted by Fermi resonance

Succinimides are characterized by two carbonyl stretching bands in the IR spectrum between 1700 and 1800 cm^{-1}, separated by about 72 cm^{-1}. The intensity of the band with the lower frequency (anti-symmetric stretching mode, $\tilde{\nu}_{as}$) is stronger than the band with the higher frequency (symmetric stretching mode, $\tilde{\nu}_s$) [155, 37, 38, 114, 20]. These characteristics are the result of the vibrational coupling of the two imide carbonyl groups through the separating nitrogen atom, carrying a lone pair of electrons. Figure 6.2 shows the conversion of native H-Asp-Ala-OH to H-Asp-Ala-OH·HCl and its succinimide derivative, 2S-(3S-aminosuccinimidyl) propionic acid hydrochloride, (Trace A, B and C respectively), as monitored by FT-IR spectroscopy of solid samples.
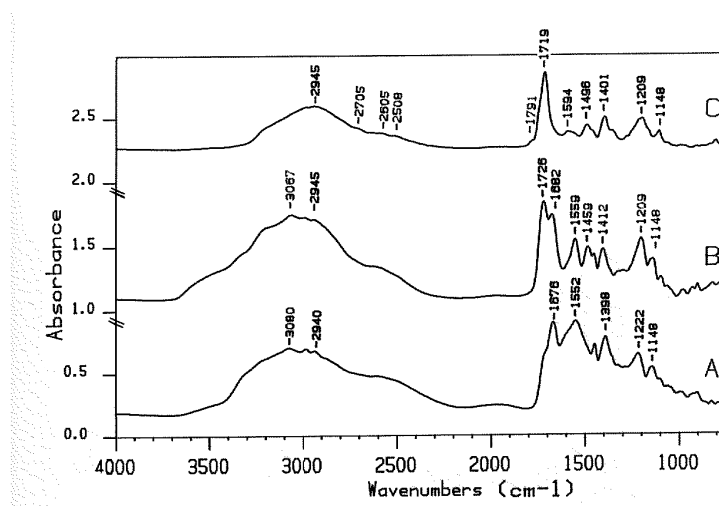
Figure 6.2: *FT-IR absorbance spectra, showing the formation of the H-Asp-Ala-OH succinimide derivative, measured in the solid state. A, H-Asp-Ala-OH; B, H-Asp-Ala-OH·HCl and C, H-Asp-Ala-OH·HCl after heating at 100°C for 48 h, in vacuo. Spectra are obtained from 0.5 mg samples, deposited on AgCl windows. The absorbance axes of traces B and C are offset.*

Formation of the HCl-salt is marked by the disappearance of one of the carboxylate stretching bands (around 1600 and 1398 cm^{-1}), whilst the

carboxylic acid stretching band (around 1726 cm^{-1}) increases. Following heating, an increase in intensity is observed around 1791 (shoulder) and 1719 cm^{-1}(symmetric and anti-symmetric stretching modes of five-membered imide rings respectively). The disappearance of the amide I and amide II bands at about 1682 and 1559 cm^{-1} demonstrates that the original peptide has completely been converted.

Surprisingly, the broad feature around 1719 cm^{-1} consists of four bands (Fig. 6.3, trace B). The three bands at 1711, 1719 and 1728 cm^{-1} are more difficult to detect in less concentrated samples, but band fitting analysis, using a second derivative or a deconvoluted spectrum as a reference, is only succesful when five bands between 1800 and 1700 cm^{-1} are included in the band fitting procedure (Table 6.1).
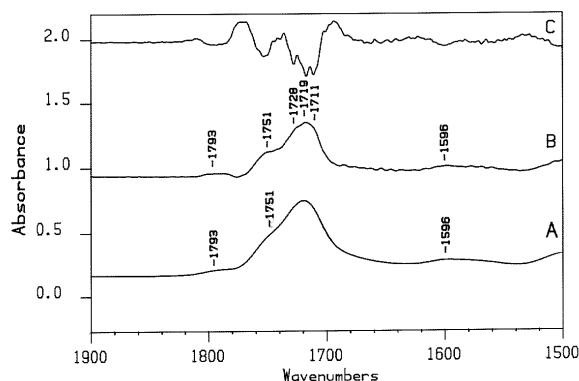
Figure 6.3: *Expanded carbonyl stretching mode region of H-Asp-Ala-OH·HCl (0.8 mg) after heating for 48 h. A, Absorbance spectrum; B, deconvoluted spectrum (bandwidth, 16* cm^{-1}; *K-factor, 2.2; apodization,* $\sin^2(x)/x^2$*) and C, second derivative spectrum (smoothing over 13 data points).*

To explain this observation, we suggest that in the solid state the IR spectrum is distorted by Fermi resonance [37, 114, 20], possibly owing to the formation of a yet unidentified succinimide dimer [37]. This mechanism describes the interaction between a fundamental and an overtone or combination vibration, having the same symmetry and almost the same energy. Under these conditions, the wavefunctions, describing the almost indiscernible vibrational states, have to be mixed, as a result of which the corresponding

$\tilde{\nu}$ (cm^{-1})	$\Delta\tilde{\nu}_{\frac{1}{2}}$	A$_{rel}$ %	assignment
1711 ± 1	15 ± 1	13 ± 1	α
1720 ± 1	21 ± 1	40 ± 3	β
1728 ± 1	22 ± 1	20 ± 1	$\tilde{\nu}$ (C=O) of COOH dimer
1751 ± 1	20 ± 1	23 ± 1	$\tilde{\nu}$ (C=O) of COOH monomer
1793 ± 1	13 ± 1	3 ± 1	$\tilde{\nu}_s$ (C=O) of imide

Calculated frequency of $\tilde{\nu}_{as}$ imide, 1718 cm^{-1}. Distance between $\tilde{\nu}_{as}$ and $\tilde{\nu}_s$ $\Delta\tilde{\nu}$, 75 cm^{-1}. Integrated intensity ratio of the calculated $\tilde{\nu}_{as}$ and $\tilde{\nu}_s$, A$_{as}$/A$_s$, 17±3.

Table 6.1: *IR band parameters of acidified and heated H-Asp-Ala-OH, as derived by band fitting. Peak positions and bandwidths in* cm^{-1}. *Fractional areas are given in percentage of the total band area. (three spectra of different samples, which were fully converted to the corresponding succinimide, were analyzed).*

energy levels diverge and the transition probabilities (i.e. peak intensities) equalize more or less. In this way, overtones or combinations, which otherwise would not be observed in the IR spectrum, may show up more clearly. It should be noted that the two bands, resulting from Fermi resonance, cannot be assigned to discrete vibrations since they both result from the mixing of two different vibrations.

Following the concept of Fermi resonance, the observed bands around 1719 cm^{-1} in the spectrum of acidified and heated aspartylalanine (Fig. 6.3) can be interpreted as a doublet at 1711 and 1720 cm^{-1}, caused by Fermi resonance between the imide anti-symmetric stretching vibration and an overtone or combination vibration, and a singlet at 1728 cm^{-1}, possibly resulting from a carboxylic acid dimer vibration.

The tentative assignment of α and β bands (Table 6.1) to the components of the proposed Fermi-doublet is a consequence of the concept, these bands being the result of mixed vibrations. Assuming that only one band (i.e. the fundamental) is detectable in the undisturbed spectrum, the other (i.e. the weak overtone or combination band) having almost zero intensity, the undisturbed band positions may be calculated from the integrated intensities

and the observed band positions, according to [17,18]:

$$\tilde{\nu}_{as} = \frac{\tilde{\nu}_\alpha + \tilde{\nu}_\beta}{2} \pm \frac{\tilde{\nu}_\alpha - \tilde{\nu}_\beta}{2} \times \left(\frac{\rho - 1}{\rho + 1}\right) \qquad (6.1)$$

In this formula, $\tilde{\nu}_{as}$ is the frequency of $\tilde{\nu}_{as}$ in the absence of Fermi resonance, $\tilde{\nu}_\alpha$ and $\tilde{\nu}_\beta$ the frequencies of the Fermi-doublet and ρ the integrated intensity ratio of the α and β bands, as derived by curve fitting analysis (Table 6.1). This calculation yields values of 1718 cm^{-1} and 1713 cm^{-1}. The band at 1718 cm^{-1} is assigned to $\tilde{\nu}_{as}$ since this frequency is more close to the band, having the strongest intensity in the disturbed spectrum. As a check on the calculation, the combination of the bands found at 1720 and 1711 cm^{-1}, should equal the combination of the calculated undisturbed levels (1718 and 1713 cm^{-1}). This follows from the principle of conservation of energy or the equation which is used to calculate the undisturbed band frequencies. The area of $\tilde{\nu}_{as}$ is taken as the sum of the areas under the α and β bands. The separation of $\tilde{\nu}_{as}$ and $\tilde{\nu}_s$ then becomes 75 cm^{-1} and the integrated intensity ratio of $\tilde{\nu}_{as}$ and $\tilde{\nu}_s$, which is related to the angle between the imide carbonyl groups [38], is 17±3. This is in good accordance with the characteristics of these bands in unperturbed spectra of cyclic imides.

6.3.2   Identification of carboxylic acid group vibrations

In order to verify these findings, spectra were also taken in a polar solvent. Under these conditions Fermi resonance is not expected to occur since hydrogen bond interaction between the solvent and the succinimide derivative results in the shifting of the bands, which produced the Fermi doublet. If the energy difference between the fundamental and the overtone or combination band becomes too large, Fermi resonance is prevented. This reduces the complexity of the spectral range between 1800 and 1700 cm^{-1}. In figure 6.4, the solid state spectrum (trace C) of the acidified and heated dipeptide is compared with the spectra, measured in Me_2SO (trace A) and in ^2H_2O (trace B). Clearly, in solution the 1719 bandshape is rather narrow and almost symmetric, implying that this band consists of less components, as compared to the solid state spectrum.

Table 6.2 summarizes the band positions between 1800 and 1700 cm^{-1}, as derived by deconvolution and second derivative analysis of the spectra, shown in figure 6.4.
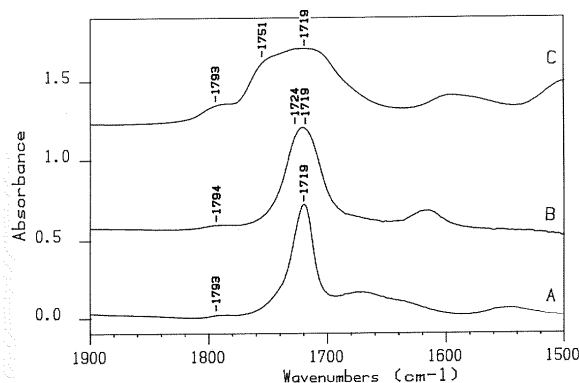
Figure 6.4: *Comparison of expanded carbonyl stretching region of H-Asp-Ala-OH·HCl after heating for 48 h, measured under different conditions. A, In Me$_2$SO solution. The broad feature around 1670* cm^{-1} *results from incomplete spectral subtraction of a trace amount of* H$_2$O *in* Me$_2$SO; *B, in* ^{2}H$_2$O *solution; C, in the solid state. The absorbance axes of trace B and C are offset and are displayed with arbitrary absorbance units.*

Indeed, in solution a single component at 1719 cm^{-1} is detected, which is very close to the calculated undisturbed frequency of $\tilde{\nu}_{as}$ in the solid state.

Carboxylic acids may associate to form dimers by hydrogen bonding [20]. This results in a lowering of the frequency for the carboxylic acid carbonyl anti-symmetric stretching mode, relative to the monomer carbonyl stretching mode. In our spectra, measured in the solid state, both monomer and dimer bands are observed. Weak overtones and combination bands, characteristic for carboxylic acid dimers, which are observed at 2705, 2605 and 2508 cm^{-1} (Fig. 6.2, trace C), support this assignment.

In ^{2}H$_2$O, the carboxylic acid dimer band is not observed, and the carboxylic acid monomer band is downshifted to 1724 cm^{-1}, due to ^{1}H/^{2}H exchange of the acidic proton and H-bond interaction between the acid carbonyl oxygen and ^{2}H$_2$O molecules. In Me$_2$SO, which is a polar and aprotic solvent, the carboxylic acid monomer is observed at 1739 cm^{-1}, owing to the formation of hydrogen bonds from the acid OH group to the oxygen atom of Me$_2$SO only.

solid	^{2}H$_2$O	Me$_2$SO	assignment
1711	-	-	α
*	1719	1719	$\tilde{\nu}_{as}$(C=O) of imide
1720	-	-	β
-	1724	-	$\tilde{\nu}$(C=O) of COO^{2}H monomer
1728	-	-	$\tilde{\nu}$(C=O) of COOH dimer
1751	-	1739	$\tilde{\nu}$(C=O) of COOH monomer
1793	1794	1793	$\tilde{\nu}_s$(C=O) of imide

* : Calculated frequency of $\tilde{\nu}_{as}$ imide, 1718 cm^{-1}(see table 6.1).

Table 6.2: *Comparison of IR band positions of acidified and heated asparty-lalanine under several experimental conditions. Peak positions in* cm^{-1}.

6.3.3   The carbon-carbon stretching mode region

The band which mixes with the imide $\tilde{\nu}_{as}$ band at 1718 cm^{-1} probably is a combination band of two imide skeletal stretching vibrations ($\tilde{\nu}$(C-C)), which absorb between 1000 and 800 cm^{-1}. Examination of this region shows bands at 918, 889, 841 and 811 cm^{-1} (Fig. 6.5, trace B). The bands at 889 and 841 cm^{-1} are close to the values for N-phenylphthalimide (881 and 847 cm^{-1}) reported by Fayat and Foucaud [37], and combination of these bands adds up to 1730 cm^{-1}. If this combination band results in Fermi resonance, a considerable anharmonicity must be allowed for, in order to achieve a frequency close to 1718 cm^{-1}, which is the calculated frequency for $\tilde{\nu}_{as}$.

6.3.4   Verification of assignments by Raman spectroscopy

Due to the low intensity of $\tilde{\nu}_s$ at 1793 cm^{-1}, we cannot decide from the IR spectrum whether Fermi resonance also occurs for this vibration. To resolve this aspect, we turned to Raman spectroscopy. For the imide carbonyl symmetric stretching vibration, the change in polarizability is much larger than the change in dipole moment [37]. This means that the intensity of $\tilde{\nu}_s$ should be much stronger in the Raman spectrum than in the IR spectrum. As expected (Fig. 6.6, trace A and B), the intensity ratio of the anti-symmetric (below 1720 cm^{-1}) and the symmetric (around 1796 cm^{-1}) imide carbonyl
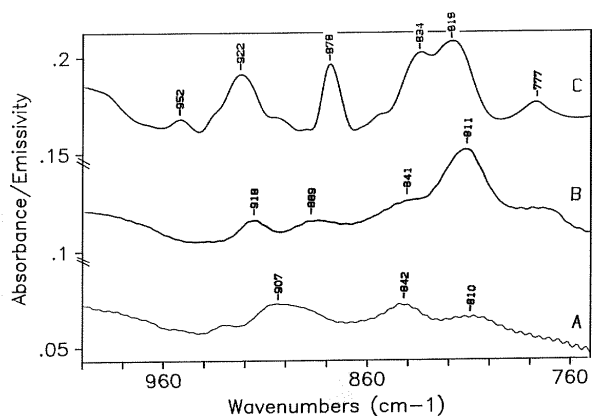
Figure 6.5: *Expanded carbon-carbon stretching mode region of the peptide succinimide derivatives. A, IR spectrum of acidified and heated H-Val-Asp-Ala-Gly-OH. The interference pattern in this spectrum is caused by internal reflection in the AgCl window; B, IR spectrum of acidified and heated H-Asp-Ala-OH; C, Raman spectrum of acidified and heated H-Asp-Ala-OH. The absorbance axes of trace A and B are displayed in arbitrary absorbance units. Trace C is displayed in arbitrary emissivity units.*

stretching bands reverses in the Raman spectrum as compared to the IR spectrum (Fig. 6.3, trace C). The second derivative Raman spectrum (Fig. 6.6, trace C) clearly shows that the symmetric stretching mode is split into two bands at 1802 and 1790 cm^{-1}.

The C-C stretching region between 1000 and 800 cm^{-1} in the Raman spectrum shows, among others, two bands at 922 and 878 cm^{-1} (Fig. 6.5, trace C), and the combination of these bands (1800 cm^{-1}), might be in resonance with $\tilde{\nu}_s$. We conclude that $\tilde{\nu}_s$ also exhibits Fermi resonance, although this cannot be clearly observed in the IR spectrum.

The intensity changes of the bands at 1727 and 1746 cm^{-1}in the Raman spectrum (Fig. 6.6, trace B and A), caused by heating of the sample by the increased laser power, reflects the shift of the carboxylic acid dimer/monomer equilibrium towards the monomer. This confirms the assignment of these bands to carboxylic acid dimer and monomer vibrations, respectively.
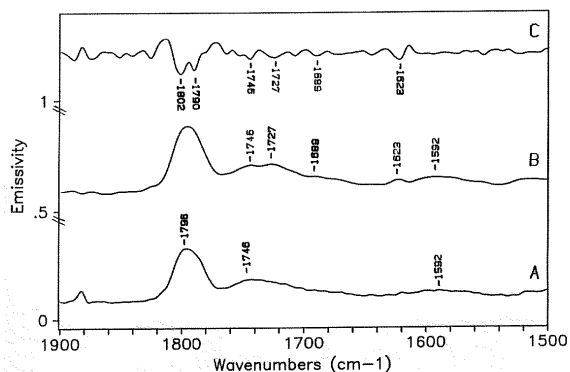
Figure 6.6: *Raman spectra of heated H-Asp-Ala-OH·HCl in the solid state. A, Carbonyl stretching, observed with a laser power of 500 mW; B, the same region, but laser power is 400 mW; C, second derivative of trace B, smoothed over 13 data points. Spectra are offset and are displayed in arbitrary emissivity units.*

6.3.5 FT-IR analysis of H-Val-Asp-Ala-Gly-OH

Since the IR spectrum of the succinimide derivative of H-Asp-Ala-OH in the solid state is distorted by Fermi resonance, we also examined the succinimide derivative of H-Val-Asp-Ala-Gly-OH. This sequence occurs in bovine αA crystallin, where it is involved in peptide chain cleavage and racemization [58]. Figure 6.7 shows that the succinimide derivative is still formed in the tetrapeptide and curve fitting analysis (Table 6.3) shows that the imide band separation of 75 cm^{-1} is preserved, but the band positions are somewhat downshifted to 1716 ($\tilde{\nu}_{as}$) and 1791 cm^{-1} ($\tilde{\nu}_s$). In the resulting succinimide derivative, Fermi resonance seems not to occur, possibly since its larger size prevents the formation of an imide dimer in the solid state. A further change is the decrease of the positive field elicited by the charged amino terminus, which resides now on Val.

The C-C stretching mode region (Fig. 6.5, trace A) in IR spectra of H-Val-Asp-Ala-Gly-OH after acidification and heating, also gives a pattern that differs from H-Asp-Ala-OH (Fig. 6.5, trace B), which was treated likewise. The band at 810 cm^{-1} is rather weak and the component at 889 cm^{-1} seems to be upshifted towards 907 cm^{-1}.
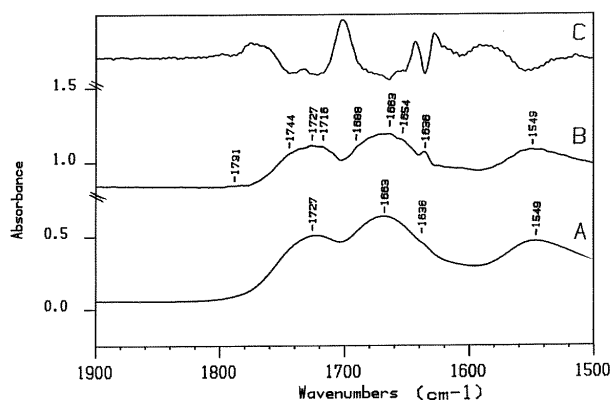
Figure 6.7: *Expanded carbonyl stretching region of heated H-Val-Asp-Ala-Gly-OH·HCl. A, Absorbance spectrum; B, deconvoluted spectrum and C, second-derivative spectrum. Deconvolution and derivatization are carried out with the same parameters, used in Fig. 6.3. The sample contained 0.5 mg. Spectra are offset and are displayed in arbitrary absorbance units.*

Hence, the succinimide derivatives of larger peptides probably can be identified in solid state IR spectra, by two carbonyl vibrations near 1716 and 1791 cm^{-1}, with a characteristic interval of 75 cm^{-1} and an intensity ratio of 17±3. In view of our assignments, we dispute the claim made by Martin et al. [95] that a band around 1735 cm^{-1} in the IR spectrum of acidified and heated calmodulin, observed by FT-IR PAS results from a succinimide

$\tilde{\nu}$ (cm^{-1})	$\Delta\tilde{\nu}_{\frac{1}{2}}$	assignment
1716 ± 1	16 ± 1	$\tilde{\nu}_{as}$ (C=O) of imide
1727 ± 1	22 ± 1	$\tilde{\nu}$ (C=O) of COOH dimer
1744 ± 1	21 ± 1	$\tilde{\nu}$ (C=O) of COOH monomer
1791 ± 1	11 ± 1	$\tilde{\nu}_s$ (C=O) of imide

Integrated intensity ratio of $\tilde{\nu}_{as}$ and $\tilde{\nu}_s$, A$_{as}$/A$_s$, 17±3.

Table 6.3: *IR band parameters of acidified and heated H-Val-Asp-Ala-Gly-OH, as derived by band fitting analysis. Peak positions and bandwidths in cm^{-1}. All values: mean ± rounded S.D. (three spectra were analysed)*

derivative. This band does not match either the IR spectra of native succinimide or any N-substituted succinimide, derived from oligopeptides.

6.4   Conclusion

We have made a revised assignment of the succinimide carbonyl stretching bands in the IR spectrum, which appear upon heating the HCl-salts of H-Asp-Ala-OH and H-Val-Asp-Ala-Gly-OH. In the case of H-Asp-Ala-OH, the antisymmetric imide carbonyl stretching band is distorted by Fermi resonance. In larger peptides or proteins, the imide carbonyl stretching bands are expected to occur around 1716 cm^{-1} ($\tilde{\nu}_{as}$) and around 1791 cm^{-1} ($\tilde{\nu}_{s}$).

The results, obtained with the tetrapeptide, can be used as a reference for the detection of succinimides in larger peptides or proteins, but one has to keep in mind that the detection of one or two succinimide rings in a sequence of twenty or even hundred amino acid residues will become very difficult, since the extinction coefficients of the imide bands are rather small relative to those of the adjacent carboxylic acid bands above 1720 cm^{-1} and the peptide backbone vibrations, associated with β-type secondary structures, just below 1700 cm^{-1}[7].

Bibliography

[1] Abeywardena, M.Y., McMurchie, E.J., Russell, G.R. and Charnock, J.S. (1984) *Biochem. Pharmacol.* 33, 3649–3654.

[2] Al-Maghtheh, M., Gregory, C., Inglehearn, C., Hardcastle, A. and Bhattacharya, S. (1993) *Human Mutation* 2, 249–255.

[3] Anderle, G. and Mendelsohn, R. (1986) *Biochemistry* 25, 2174–2179.

[4] Andrew, B.E. (1993) *Analyst* 118, 153–155.

[5] Aswad, D. (1984) *J. Biol. Chem.* 259, 10714–10721.

[6] Baenziger, J.E., Miller, K.W. and Rothschild, K.J. (1993) *Biochemistry* 32, 5448–5454.

[7] Bandekar, S. (1992) *Biochim. Biophys. Acta* 1120, 123–143 and references therein

[8] Bennett, J.P., Smith, G.A., Houslay, M.D., Hesketh, T.R., Metcalfe, J.C. and Warren, G.B. (1978) *Biochim. Biophys. Acta* 513, 310–320.

[9] Benson, E.L. (1993) *Invest. Ophtalmol. Vis. Sci.* 34, 1659–1676.

[10] Bloemendal, H. (1981) *Molecular and Cellular Biology of the Eye Lens* (John Wiley and Sons, New York).

[11] Blume, A. , Hübner, W. and Messner, G. (1988) *Biochemistry* 27, 8239–8249.

[12] Braiman, M. and Rothschild, K.J. (1988) *Ann. Rev. Biophys. Chem.* 17, 541-570.

[13] Brenner-Hénaff, C., Valdor, J.-F., Plusquellec, D. and Wróblewski, H. (1993) *Anal. Biochem.* 212, 117-127.

[14] Broekhuyse, R.M. (1968) *Biochim. Biophys. Acta.* 152, 307–315.

[15] Caffrey, M. (1993) *LIPIDAT: A Database of Thermodynamic Data and Associated Information on Lipid Mesomorphic and Polymorphic Transitions* CRC Press, Boca Raton.

[16] Chou, P.Y., and Fasman, G.D. (1974) *Adv. Enzymol.* 47, 45–148.

[17] Chou, P.Y. and Fasman, G.D. (1977) *J. Mol. Biol.* 115, 135–175.

[18] Clark, N.A., Rothschild, K.J., Simon, B.A. and Luippold, D.A. (1980) *Biophys. J.* 31, 65–96.

[19] Clarke, S. (1987) *Int. J. Peptide Protein Res.* 30, 808-821.

[20] Colthup, N.B., Daly, L.H., Wiberley, S.E. (1964) *Introduction to Infrared and Raman Spectroscopy*, pp. 257–260 and 266–267, Academic Press, New York.

[21] Cooley, J.W. and Tukey, J.W. (1965) *Math. Comput.* 19, 297–301.

[22] Cornelius, F. and Skou, J.C. (1984) *Biochim. Biophys. Acta* 772, 357–373.

[23] Crowe, J.H., Crowe, L.M. and Hoekstra, F.A. (1989) *J. Bioenergetics Biomembranes* 21, 77–91.

[24] De Foresta, B., Henao, F. and Champeil, P. (1992) *Eur. J. Biochem.* 209, 1023–1034.

[25] De Grip, W.J. and Bovee-Geurts, P.H.M. (1979) *Chem. Phys. Lipids* 23, 321–325.

[26] De Grip, W.J., Daemen, F.J.M. and Bonting, S.L. (1980) *Methods Enzymol.* 67, 301–320.

[27] De Grip, W.J., Gillespie, J. and Rothschild, K.J. (1985) *Biochim. Biophys. Acta* 809, 97–106.

[28] De Grip, W.J., Gray, D., Gillespie, J., Bovee, P.H.M., Van den Berg, E.M.M., Lugtenburg, J. and Rothschild, K.J. (1988) *Photochem. Photobiol.* 48, 57–62.

[29] Demel, R.A., Goormaghtigh, E. and De Kruijff, B. (1990) *Biochim. Biophys. Acta* 1027, 155–162.

[30] De Pont, J.J.H.H.M., Van Prooijen-Van Eeden, A. and Bonting, S.L. (1978) *Biochim. Biophys. Acta* 508, 464–477 and references therein.

[31] Di Donato, A., Galletti, P., D'Alessio, G. (1986) *Biochemistry* 25, 8361–8368.

[32] Dong, A., Huang, P. and Caughey, W.S. (1990) *Biochemistry* 29, 3303–3308.

[33] Downer, N.W., Bruchman, T.J. and Hazard, J.H. (1986) *J. Biol. Chem.* 261, 3640–3647.

[34] Van Duynhoven, J.P.M., Folkers, P.J.M., Prinse, C.W., Harmsen, B.J.M., Konings, R.N.H. and Hilbers, C.W. (1992) *Biochemistry* 31, 1254–1262.

[35] Earnest, T.N., Herzfeld, J. and Rothschild, K.J. (1990) *Biophys. J.* 58, 1539–1546.

[36] Fahmy, K and Siebert, F. (1993) *Proc. Natl. Acad. Sci. USA* 90, 10206–10210.

[37] Fayat, C., Foucaud, A. (1970) *Bull. Soc. Chim. Fr.* , 4491–4501.

[38] Fayat, C., Foucaud, A. (1970) *ibid.* , 4501–4505.

[39] Fellgett, P.B. (1958) *J. Phys. Radium* 19, 187–237.

[40] Fringeli, U.P., Apell, H.-J., Fringeli, M. and Laüger (1989) *Biochim. Biophys. Acta* 984, 301–312.

[41] Fringeli, U.P. and Gunthard, H.H. (1980) in: *Molecular Biology, Biochemistry and Biophysics, Membrane Spectroscopy (Grell, E. Ed.)* , Vol. 31, pp. 270–332, Springer Verlag, Berlin.

[42] Furth, A.J., Bolton, H., Potter, J. and Priddle, J.D. (1984) *Methods Enzymol.* 104, 318–328.

[43] Ganter, U.M., Charitopoulos, T., Virmaux, N. and Siebert, F. (1992) *Photochem. Photobiol.* 56, 57–62.

[44] Ganter, U.M., Schmid, E.D., and Siebert, F. (1988) *J. Photochem. Photobiol., B: Biology* 2, 417–426.

[45] Ganter, U.M., Gärtner, W. and Siebert, F. (1988) *Biochemistry* 27, 7480–7488.

[46] Ganter, U.M., Kashima, T.,Sheves, M. and Siebert, F. (1991) *J. Am. Chem. Soc.* 113, 4087–4092.

[47] Ganter, U.M., Gärtner, W. and Siebert, F. (1990) *Eur. Biophys. J.* 18, 295–299.

[48] Ganter, U.M., Schmid, E.D., Perez-Sala, D., Rando, R.R. and Siebert, F. (1989) *Biochemistry* 28, 5954–5962.

[49] Garcia-Quintana, D., Garriga, P. and Manyosa, J. (1993) *J. Biol. Chem.* 268, 2403–2409.

[50] Garnier, J., Osguthorpe, D.J. and Robson, B. (1978) *J. Mol. Biol.* 120, 97–120.

[51] Geering, K. (1990) *J. Membrane Biol.* 115, 109–121.

[52] Geiger, T., Clarke, S. (1987) *J. Biol. Chem.* 262, 785-794.

[53] Gibson, N.J. and Brown, M.F. (1993) *Biochemistry* 32, 2438–2454.

[54] Glasser, L. (1987) *J. Chem. Ed.* 64, A229–A233, *ibid*, A260–A266, *ibid*, A306–A313.

[55] Goodrich, R.P., Crowe, J.H., Crowe, L.M. and Baldeschwieler J.D. (1991) *Biochemistry* 30, 5313–5318.

[56] Goormaghtigh, E., Cabiaux, V., Ruysschaert, J.-M. (1990) *Eur. J. Biochem.* 193, 409–420.

[57] Goormaghtigh, E. and Ruysschaert, J.-M. (1989) in: *Molecular Description of Biological Membranes by Computer Aided Conformational Analysis* Volume I Ch. 1.B.3 pp. 285–328. (Brasseur, R. Ed.) CRC Press, Boca Raton.

[58] Groenen, P.J.T.A, Van den IJssel, P.R.L.A., Voorter, C.E.M., Bloemendal, H. and De Jong, W.W. (1990) *FEBS lett.* 269, 109–112.

[59] Hamm, H.E. (1991) *Cell. Mol. Neurobiol.* 11, 563–577.

[60] Hargrave, P.A. (1977) *Biochim. Biophys. Acta* 462, 83–94.

[61] Hargrave, P.A., Hamm, H.E. and Hofmann, K.P. (1993) *BioEssays* 15, 43–50.

[62] Hargrave, P.A., McDowell, J.H., Curtis, D.R., Wang, J.K., Juszczak, E., Fong, S.L., Rao, J.K.M. and Argos, P. (1983) *Biophys. Struct. Mech.* 9, 235–244.

[63] Haris, P.I., Coke, M. and Chapman, D. (1989) *biochim. Biophys. Acta* 995, 160-167.

[64] Herres, W. and Zachmann, G. (1984) *LaborPraxis* 6, 632–638.

[65] Hesse, M., Meier, H. and Zeeh, B. (1991) *Spectroscopische Methoden in der Organischen Chemie* Chapter 2, pp. 29–68, Thieme, Stuttgart.

[66] Hjelmeland, L.M. and Chrambach, A. (1984) *Methods Enzymol.* 104, 305–318.

[67] Hollenberg, M.D. (1991) *FASEB J.* 5, 178–186.

[68] Hübner, W., Mantsch, H.H. and Kates, M. (1991) *Biochim. Biophys. Acta* 1066, 166–174.

[69] Jackson, M. and Mantsch, H.H. (1991) *Biochim. Biophys. Acta* 1078, 231–235.

[70] Jackson, M. and Mantsch, H.H. (1992) *Biochim. Biophys. Acta* 1118, 139–143.

[71] Johannsson, A., Keightley, C.A., Smith, G.A., Richards, C.D., Hesketh, T.R. and Metcalfe, J.C. (1981a) *J. Biol. Chem.* 256, 1643–1650.

[72] Johannsson, A., Smith, G.A. and Metcalfe, J.C. (1981b) *Biochim. Biophys. Acta.* 641, 416–421.

[73] Johnson, B.A., Freitag, N.E., Aswad, D. (1985) *J. Biol. Chem.* 260, 10913-10916.

[74] Jørgensen, P.L. (1974) *Biochim. Biophys. Acta* 356, 36–52.

[75] Karlish, S.J.D. (1980) *J. Bioenergetics Biomembranes* 12, 111–136.

[76] Kauppinen, J.K., Moffat, D.J., Mantsch, H.H. and Cameron, D.G. (1981) *Appl. Spectrosc.* 35, 271–276.

[77] Kauppinen, J.K., Moffat, D.J., Mantsch, H.H. and Cameron, D.G. (1981) *Anal. Chem.* 53, 1454–1457.

[78] Klausner, R.D., Van Renswoude, J. and Rivnay, B. (1984) *Methods Enzymol.* 104, 340–347.

[79] Koenig, J.L., L. D'Esposito and M.K. Antoon. 1977. *Appl. Spectrosc.* 31, 292–295.

[80] König, B., Arendt, A., McDowell, J.H., Kahlert, M. Hargrave, P.A. and Hofmann, K.P. (1989) *Proc. Natl. Acad. Sci. USA* 86, 6878–6882.

[81] Kühn, H., Mommertz, O. and Hargrave, P.A., (1982) *Biochim. Biophys. Acta* 679, 95-100.

[82] Kyte, J. and Doolittle, R.F. (1982) *J. Mol. Biol.* 157, 105–132.

[83] Lagnado, L. and Baylor, D. (1992) *Neuron* 8, 995–1002.

[84] Lamba, O.P., Borchman, D., Sinha, S.K., Shah, J., Renugopalakrishnan, V. and Yappert, M.C. (1993) *Biochim. Biophys. Acta* 1163, 113–123.

[85] Lee, D.C., Haris, P.I., Chapman, D. and Mitchell, R.C. (1990) *Biochemistry* 29, 9185–9193.

[86] Levitt, M. and Greer, J. (1977) *J. Mol. Biol.* 114, 181–239.

[87] Lewis, B.A. and Engelman, D.M. (1983) *J. Mol. Biol.* 166, 203–210 and 211–217.

[88] Lewis, R.N.A.H., McElhaney, R.N., Pohle, W. and Mantsch, H.H. (1994) *Biophys. J.* 67, 2367–2375.

[89] Lingrel, J.B. and Kuntzweiler, T. (1994) J. *Biol. Chem.* 269, 19659–19662.

[90] Luo, S., Liao, C.-X., McClelland, J.F., Graves, D.J. (1987) *Int. J. Peptide Protein Res.* 29, 728–733.

[91] Luo, S., Huang, C.-Y.F., McClelland, J.F. and Graves, D.J. (1994) *Anal. Biochem.* 216, 67–76.

[92] Lutsenko, S. and Kaplan, J.H. (1993) *J. Biol. Chem.* 269, 19659–19662.

[93] Maddams, W.F. (1980) *Appl. Spectrosc.* 34, 245-267.

[94] Marcus, M.M., Apell, H.J., Roudna, M., Schwendener, R.A., Weder, H.G. and Läuger, P. (1986) *Biochim. Biophys. Acta.* 854, 270–278.

[95] Martin, B.L., Wu, D., Tabatabai, L., Graves, D.J. (1990) *Arch. Biochem. Biophys.* 276, 94–101.

[96] Matthews, P.L.J., Bartlett, E., Ananthanarayanan, V.S. and Keough, K.M.W. (1993) *Biochem. Cell. Biol.* 71, 381–389.

[97] McDowell, J.H., Nawrocki, J.P. and Hargrave, P.A. (1993) *Biochemistry* 32, 4968–4974.

[98] Mendelsohn, R., Anderle, G., Jaworsky, M., Mantsch, H.H. and Dluhy, R.P. (1984) *Biochim. Biophys. Acta* 775, 215–224.

[99] Miyazawa, T. (1960) *J. Chem. Phys.* 32, 1647–1652.

[100] Mimura, K., Matsui, H., Takagi, T. and Hayashi, Y. (1993) *Biochim. Biophys. Acta* 1145, 63–74.

[101] Mitchell, R.C., Haris, P.I., Fallowfield, C., Keeling, D.J. and Chapman, D. (1988) *Biochim. Biophys. Acta* 941, 31–38.

[102] Mollevanger, L.C.P.J. (1987) Ph.D. Thesis, Nijmegen

[103] Mollevanger, L.C.P.J. and De Grip, W.J. (1984) *FEBS Lett.* 169, 256–260.

[104] Mouritzen, O.G. and Bloom, M. (1984) *Biophys. J.* 46, 141–153.

[105] Mouritzen, O.G. and Bloom, M. (1993) *Annu. Rev. Biophys. Biomol. Struct.* 22, 145–171.

[106] Naik, V.M., Krimm, S., Denton, J.B., Nemethy, G. and Scheraga, H.A. (1984) *Int. J. Peptide Protein Res.* 24, 613–626.

[107] Nakanishi, K. (1991) *Pure & Appl. Chem.* 63, 161–170.

[108] Nathans, J. (1987) *Ann. Rev. Neurosci.* 10, 163–194.

[109] Ohguro, H., Palczewski, K., Ericsson, L.H., Walsh, K.A. and Johnson, R.S. (1993) *Biochemistry* 32, 5718–5724.

[110] Ostrowski, J., Kjelsberg, M.A., Caron, M.G. and Lefkowitz, R.J. (1992) *Annu. Rev. Pharmacol. Toxicol.* 32, 167–183.

[111] Ovchinnikov, Y.A. (1982) *FEBS Lett.* 148, 179–191.

[112] Ovchinnikov, Y.A. (1987) *Trends Bioch. Sci.* 12, 434-438.

[113] Ovchinnikov, Y.A., Abdulaev, N.G. and Bogachuk, A.S. (1988) *FEBS Lett.* 230, 1–5.

[114] Overend, J. (1963) in: *Infrared Spectroscopy and Molecular Structure* (Davies, M., ed.), chapter X, pp. 345-376, Elsevier, New York

[115] Palings, I., Van den Berg, E.M.M., Lugtenburg, J. and Mathies, R.A. (1989) *Biochemistry* 28, 1498–1507.

[116] Papac, D.I., Oatis, J.E., Crouch, R.K. and Knapp, D.R. (1993) *Biochemistry* 32, 5930–5934.

[117] Pappin, D.J.C., Eliopoulos, E., Brett, M. and Findlay, J.B.C (1984) *Int. J. Biol. Macromol.* 6, 73–76.

[118] Pellicone, C., Nullans, G., Cook, N.J. and Virmaux, N. (1985) *Biochem. Biophys. Res. Comm.* 127, 816–821.

[119] Perkins, W.D. (1986) *J. Chem. Ed.* 63, A5-A10.

[120] Perkins, W.D. (1987) *J. Chem. Ed.* 64, A269-A271.

[121] Perkins, W.D. (1987) *J. Chem. Ed.* 64, A296-A305.

[122] Peters, W.H.M., Fleuren-Jakobs, A.M.M., De Pont, J.J.H.H.M. and S.L. Bonting. (1981) *Biochim. Biophys. Acta* 649, 541–549.

[123] Peterson, G.L. (1977) *Anal. Biochem.* 83, 346–356.

[124] Philipson, K.D. and Ward, R. (1987) *Biochim. Biophys. Acta* 897, 152–158.

[125] Prado, A., Muga, A. Castresana, J., Goñi, F.M. and Arrondo, J.L.R. (1990) *FEBS Lett.* 269, 324–327.

[126] Prestrelski, S.J., Tedeschi, N., Arakawa, T. and Carpenter, J.F. (1993) *Biophys. J.* 65, 661–671.

[127] Probst, W.C., Snyder, L.A., Schuster, D.I. Brosius, J. and Sealfon, S.C. (1992) *DNA and Cell Biology* 11, 1–20.

[128] Pugh Jr., E.N. and Lamb, T.D. (1990) *Vision Res.* 30, 1293–1948.

[129] Rath, P., De Caluwé, G.L.J., Bovee-Geurts, P.H.M., De Grip, W.J. and Rothschild, K.J. (1993) *Biochemistry* 32, 10277–10282.

[130] Renugopalakrishnan, V., Chandrakasan, G., Moore, S., Hutson, T.B., Berney, C.V. and Bhatnagar, R.S. (1989) *Macromolecules* 22, 4121–4124.

[131] Repke, K.R.H. and Schön, R. (1992) *Biol. Rev.* 67, 31–78.

[132] Roelofsen, B. (1981) *Life Sci.* 29, 2235–2247.

[133] Rost, B. and Sander, C. (1993) *J. Mol. Biol.* 232, 584–599.

[134] Rost, B. and Sander, C. (1994) *Proteins* 19, 55–72.

[135] Rost, B. Casadio, R., Fariselli, P. and Sander, C. (1995) *Protein Science* 4, 521–533.

[136] Rothschild, K.J., Gillespie, J. and De Grip, W.J. (1987) *Biophys. J.* 51, 345–350.

[137] Rothschild, K.J., Sanches, R., Hsiao, T.L. and Clark, N.A. (1980) *Biophys. J.* 31, 53–64.

[138] Safar, J., Roller, P.P., Ruben, G.C., Gajdusek, D.C. and Gibbs Jr., C.J. (1993) *Biopolymers* 33, 1461–1476.

[139] Sarver, R.W. and Krueger, W.C. (1991) *Anal. Biochem.* 194, 89-100.

[140] Sarver, R.W. and Krueger, W.C. (1991) *Anal. Biochem.* 199, 61–67.

[141] Sarver, R.W. and Krueger, W.C. (1993) *Anal. Biochem.* 212, 519–525.

[142] Savitsky, A., Golay, M.J.E. (1964) *Anal. Chem.* 36, 1627–1638.

[143] Schalken, J.J., Janssen, J.J.M., Sanyal, S., Hawkins, R.K. and De Grip, W.J. (1990) *Biochim. Biophys. Acta* 1033, 103–109.

[144] Schertler, G.F.X, Villa, C. and Henderson, R. (1993) *Nature* 362, 770–772.

[145] Schuurmans Stekhoven, F.M.A.H., Tesser, G.I., Ramsteyn, G., Swarts, H.G.P. and De Pont, J.J.H.H.M. (1992) *Biochim. Biophys. Acta* 1109, 17–32.

[146] Shankland, R.S. (1977) *The Physics Teacher* 1, 19–25.

[147] Silvius, J.R. (1992) *Annu. Rev. Biophys. Biomol. Struct.* 21, 323–348.

[148] Skinner, M.M., Zhang, H., Leschnitzer, D.H., Guan, Y. Bellamy, H., Sweet, R.M., Gray, C.W., Konings, R.N.H., Wang, A.H.J. and Terwilliger, T.C. (1994) *Proc. Natl. Acad. Sci. USA* 91, 2071–2075.

[149] Stryer, L. (1985) *Biopolymers* 24, 29–47.

[150] Stubbs, G.W., Smith, H.G. and Litman, B.J. (1976) *Biochim. Biophys. Acta* 426, 46–56.

[151] Surewicz, W.K. and Mantsch, H.H. (1988) *Biochim. Biophys. Acta* 952, 115–130.

[152] Surewicz, W.K., Mantsch, H.H. and Chapman, D. (1993) *Biochemistry* 32, 389–394.

[153] Teshima, G., Stults, J.T., Ling, V., Canova-Davis, E. (1991) *J. Biol. Chem.* 266, 13544–13547.

[154] Uhmann, W., Becker, A., Taran, C. and Siebert, F. (1991) *Appl. Spectrosc.* 45, 390–397.

[155] Vanclef, A., Bouche, R. (1979) *Spectrosc. Lett.* 12, 371–385.

[156] Vandeginste, B.G.M. and De Galan, L. (1975) *Anal. Chem.* 47, 2124–2132.

[157] Vandenbussche, G., Clercx, A., Curstedt, T., Johansson, J., Jornvall, H. and Ruysschaert, J.-M. (1992) *Eur. J. Biochem.* 203, 201–209.

[158] Veerkamp, J.H., Peeters, R.A. and Maatman, R.G.H.J. (1991) *Biochim. Biophys. Acta* 1081, 1–24.

[159] Van Winkle, W.B., Lane, L.K. and Schwartz, A. (1976) *Expt. Cell Res.* 100, 291–296.

[160] Voorter, C.E.M., De Haard-Hoekman, W.A., Van den Oetelaar, P.J.M., Bloemendal, H., De Jong, W.W. (1988) *J. Biol. Chem.* 263, 19020–19023.

[161] Wald, G. (1968) *Nature* 219, 800–807.

[162] Wallach, D.F.H., Verma, S.P. and Fookson, J. (1979) *Biochim. Biophys. Acta* 559, 153–208.

[163] Warren, G.B., Toon, P.A., Birdsall, N.J.M., Lee, A.G. and Metcalfe, J.C. (1974) *Proc. Natl. Acad. Sci. U.S.A.* 71, 622–626.

[164] Wayne, R.P. (1987) *Chemistry in Brittain* 5, 440–446.

[165] Wiedmann, T.S., Pates, R.D., Beach, J.M., Salmon, A. and Brown, M.F. (1988) *Biochemistry* 27, 6469–6474.

[166] Wistow, G., Turnell, B., Summer, L., Slingsby, C., Moss, D., Miller, L., Lindley, P. and Blundell, T. (1983) *J. Mol. Biol.* 170, 175–202.

[167] Womack, M.D., Kendall, D.A. and MacDonald, R.C. (1983) *Biochim. Biophys. Acta* 733, 210–215.

[168] Wright, H. T. (1991) *Prot. Eng.* 4, 283–294.

[169] Yeagle, P.L., Alderfer, J.L. and Albert, A.D. (1995) *Biochemistry* 34, 14621–14625.

[170] Yeagle, P.L., Alderfer, J.L. and Albert, A.D. (1995) *Nature Struct. Biol.* 2, 832–834.

[171] Yoshizawa, T. and Schichida, Y. (1982) *Methods Enzymol.* 81, 333–353.

[172] Zanotti, G., Scapin, G., Spadon, P., Veerkamp, J.H. and Sacchettini, J.C. (1992) *J. Biol. Chem.* 267, 18541–18550.

[173] Zuber, G., Prestrelski, S.J. and Benedek, K. (1992) *Anal. Biochem.* 207, 150–156.

Summary

This thesis describes the use of (FT-)IR spectroscopy in general biochemical research. Infrared spectroscopy is a technique, based on the detection of molecular vibrations (*chapter 1*). Since these vibrations are characteristic for the system under study, analysis of IR spectra may result in a more detailed knowledge of structure and function of such a system. The success of infrared spectroscopy lies in the fact that the vibrations of many functional groups, occurring in biopolymers can be discerned. Furthermore, it is a non-invasive technique, which means that no additional probe molecules need to be introduced.

Biochemistry itself, provides methods to make small changes in biopolymers: ligand binding, enzymatic modifications and even the effect of a strategic point mutation in a protein are detectable by infrared spectroscopy. Also, measuring the response of a biochemical system to changes in the environment (e.g. pH, temperature, light) yields invaluable information. These changes mutually aid in the interpretation of complex spectra with many, often overlapping, peaks. The final part of chapter 1 describes the use and possible misuse of mathematical procedures to (partially) resolve overlapping spectral components.

One of the subjects of study throughout this thesis, the photoreceptor, rhodopsin, is introduced in *chapter 2*. This integral membrane protein, containing a covalently linked chromophore, 11-*cis* retinal, is responsible for vision under dim light conditions. In response to a light pulse, the retinal isomerizes to *all-trans* and the structure of the protein changes to adapt to the structural change of the chromophore. These structural changes result in the binding of a G-protein or transducin, which conveys the message to the cell membrane. Hyperpolarization of this membrane finally results in a nerve impulse.

Largely, because of the availability, both in quality and in quantity, rho-

dopsin has become a model for the still growing superfamily of the G-protein coupled receptors. All these receptors have the seven trans-membrane helical domain architecture in common, as well as binding/release of an effector and the involvement of a specific G-protein for transfer of the signal.

In *chapter 3*, IR spectroscopy is used in the quantitation of residual detergent after reconstitution of an integral membrane protein in a pre-defined lipid matrix. This chapter discusses the choice of the vibrational band for quantitation, which is aimed to minimize the disturbing influences of other components in the mixture. Calibration is performed by ratioing the peak height of a detergent signal against the peak height of a phospholipid signal. Compared to other quantitative analytical methods, IR spectroscopy in general, is applicable in a wider range of different types of detergents, despite its somewhat lesser sensitivity.

In the past few years, FT-IR spectroscopy has become very popular to study the secondary structure of proteins. This application focusses on the amide I and amide II bands, around 1650 cm^{-1} and 1550 cm^{-1} respectively, representing the vibrations in the peptide backbone of a protein. Owing to different hydrogen bonding patterns in secondary structural elements, these bands are composed of several sub-components, together representing the overall secondary structure. *Chapter 4* describes such a study on rhodopsin, employing a methodology to circumvent practical difficulties, encountered when measuring IR spectra of aqueous solutions. By analyzing dehydrated samples, no correction for the solvent, water, needs to be made. In these samples, a correct secondary structure is observed, since this level of protein structure is determined by *intra-molecular* hydrogen bonding. Although no definitive proof of correctness, the results of this method compare well with those, obtained by NMR spectroscopy or X-ray crystallography; techniques which yield 3-dimensional structural information with a very high spatial resolution.

By making use of Fourier self-deconvolution and analysis of second derivative spectra, the amide I band is decomposed in contributions by α-helices, β-sheets and β-turns. This is the most critical step in the entire procedure, since incorrect use of these methods erroneously introduces additional spectral components, which are easily misinterpreted as real structural features. Subsequently, the area under the spectral components, found in the previous step, is determined by means of a band fitting procedure. The amounts of secondary structural elements present, are expressed as a percentage of the total area under the amide I band.

Determination of the secondary structure of a protein only becomes interesting when structural elements can be localized in the protein. Thus, comparing the results from the complete photoreceptor protein with those obtained from proteolytically treated samples, it is concluded that the C-terminal region of rhodopsin adopts a β-sheet structure and that the third cytoplasmic loop is formed by an α- helix. This is the first detailed analysis of the secondary structure of rhodopsin, insofar that, apart from the seven helical transmembrane domains, some structural elements have been assigned to protein domains, responsible for interaction with the G-protein or transducin.

In *chapter 5*, a study on interactions occurring between Na^+, K^+-ATPase and phospholipids with increasing unsaturated acyl chains is presented. The use of a relative frequency shift is introduced as a method to correct for the effect of creating a mixture of two components, exhibiting no interaction between the components.

As deduced from the positive relative bandshift of the specific lipid absorption band at about 2852 cm^{-1}(representing CH_2 symmetric stretching), as a function of temperature, Na^+, K^+-ATPase disturbs the lipid order in relatively saturated phospholipid membranes. Incorporating the protein in a highly unsaturated lipid matrix at low temperature results in no apparent hydrophobic interaction. From the changes in the amide I band it is concluded that protein aggregation has occurred. By increasing the temperature however, aggregation is diminished, thereby increasing the possibility for hydrophobic interaction between the protein and phospholipid. Accordingly, a relatively strong downshift of the lipid methylene vibrational band is found. These results are in accordance with the mattress model for protein-lipid interactions, except for the protein-protein interactions in extra-membrane domains, which are not explicitly treated by this model.

Finally, *chapter 6* deals with an analysis of the formation of succinimide derivatives in small peptide fragments. Formation of such derivatives provides a mechanism for the age-dependent degradation of proteins *in vivo*, since for example, some breakdown products of αA-crystallin, found in the ageing eye lens, can be the result of hydrolysis of a succinimide. Although the conditions, described in this chapter are by no means physiologically relevant, it should be pointed out that Nature provides other routes to activated intermediates, viz. phosphorylation. A well-known example is the enzyme Na^+, K^+-ATPase, presented in chapters 3 and 5. During a catalytic cycle, this enzyme is activated by phosphorylation of an aspartic acid residue

(Asp_{376}), resulting in a mixed anhydride. In the case of Na^+,K^+-ATPase however, no break-down occurs at this position, owing to the less flexible protein structure (presumably β-type) in this region.

In conclusion, FT-IR spectroscopy is an elegant technique to tackle a manifold of biochemical problems. Although it cannot rival NMR for its structure resolving power, it can give more global information about larger biochemical systems, where the use of high resolution NMR spectroscopy is not possible. Especially by combination with modern molecular biological techniques, detailed structure-function relationships on a topical level can be revealed.

Samenvatting

Dit proefschrift beschrijft het gebruik van infrarood (IR) spectroscopie in diverse takken van biochemisch onderzoek. Infrarood spectroscopie is een techniek die gebaseerd is op de detectie van moleculaire vibraties (*hoofdstuk 1*). Aangezien deze vibraties karakteristiek zijn voor het te onderzoeken systeem, kan analyse van IR spectra een beter inzicht geven in de structuur en de werking van een dergelijk (biochemisch) systeem. Dat spectra tegenwoordig worden opgenomen met een Fourier transform infrarood (FT-IR) spectrofotometer is voornamelijk een technische bijzonderheid en doet niets af aan de aard van de informatie, die deze techniek oplevert. Het geheim van het succes van infrarood spectroscopie is dat de vibraties van functionele groepen, zoals die voorkomen in bio-polymeren, onderscheiden kunnen worden. Hiernaast is het een niet-invasieve techniek, hetgeen betekent dat er geen label-moleculen ingebouwd hoeven te worden om iets te kunnen meten.

Het is de biochemie zelf, die methodes aanreikt om kleine veranderingen aan te brengen in bio-polymeren: de binding van een ligand, enzymatische modificaties en zelfs het effect van een strategisch aangebrachte punt-mutatie in een eiwit leiden tot detecteerbare veranderingen in een infrarood spectrum. Ook de respons van een biochemisch systeem op een verandering van omgeving (zuurgraad, temperatuur, licht) levert zeer waardevolle informatie op. Omgekeerd maken deze veranderingen de interpretatie van complexe spectra, met vele overlappende pieken, een stuk gemakkelijker. Het laatste deel van hoofdstuk 1 is gewijd aan het gebruik en mogelijk misbruik van wiskundige procedures om overlappende pieken te kunnen ontrafelen.

In *hoofdstuk 2* van dit proefschrift wordt de fotoreceptor, rhodopsine, geïntroduceerd als een van de onderzoeksobjecten. Dit integrale membraaneiwit bevat een covalent gebonden chromofoor, 11-*cis* retinal, en is verantwoordelijk voor het visuele proces bij lage lichtsterktes. Als gevolg van detectie van licht, isomeriseert het gebonden retinal naar een *all-trans* configuratie.

De structuur van het eiwit past zich aan bij de veranderde structuur van de chromofoor. Het totaal van deze structuurveranderingen resulteert in de binding van een zogenaamd G-eiwit oftewel transducine. Dit eiwit zorgt verder voor de overdracht van de visuele boodschap naar de celmembraan. Hyperpolarisatie van deze membraan leidt uiteindelijk tot een zenuwimpuls naar het centrale zenuwstelsel.

Vooral vanwege de beschikbaarheid van ruime hoeveelheden gezuiverd rhodopsine, is het fotoreceptoreiwit een model geworden voor de superfamilie van G-eiwit gekoppelde receptoren, waarvan nog steeds nieuwe leden worden ontdekt. Al deze receptoren hebben als gemeenschappelijke kenmerken: een zeven trans-membrane helix-architectuur, binding van een effector (geldt niet voor fotoreceptoren) en binding van een receptor-specifiek G-eiwit voor het verder doorgeven van het signaal.

In *hoofdstuk 3* is IR spectroscopie gebruikt voor de kwantitatieve bepaling van detergentia, die achterblijven na de inbouw (reconstitutie) van een integraal membraaneiwit in een vooraf gekozen lipide matrix. Dit hoofdstuk behandelt de keuze van de spectrale band, die gebruikt wordt in de bepaling. Het is van belang dat andere componenten, die de bepaling verstoren (eiwit, lipiden), zo min mogelijk bijdragen aan deze piek. IJking vindt plaats door de piekhoogte van de detergens-band te delen door de piekhoogte van een specifieke fosfolipide-band. Omdat de lipide-samenstelling bekend is, kan uit de piekverhouding de hoeveelheid detergens bepaald worden. In het algemeen geldt dat, vergeleken met andere kwantitatieve analytische methodes, infrarood-spectroscopie geschikt is voor de bepaling van meerdere typen detergentia, maar dat de gevoeligheid wat lager ligt.

In de afgelopen paar jaren is FT-IR spectroscopie in toenemende mate gebruikt om de secundaire structuur van eiwitten te bestuderen. Deze methodiek concentreert zich op de analyse van de amide I en amide II banden, rond respectievelijk 1650 en 1550 cm^{-1}, die afkomstig zijn van vibraties van de peptide-bindingen van het eiwit. Als gevolg van verschillen in de patronen van waterstof-bruggen in de diverse secundaire structuur-elementen, bestaan de amide I en amide II banden uit meerdere sub-componenten, die tesamen de globale secundaire structuur van het eiwit weergeven.

Hoofdstuk 4 beschrijft een dergelijke studie aan rhodopsine, waarbij een methode is gevolgd, die er op gericht is om de praktische problemen te omzeilen die er zijn bij de acquisitie van IR spectra van waterige oplossingen. Door de materialen in gedehydrateerde toestand te analyseren, hoeft er geen correctie voor het oplosmiddel, water, plaats te vinden. Dat op deze manier

een correcte secundaire structuur wordt gevonden, is een gevolg van het feit dat op dit niveau de eiwitstructuur bepaald wordt door *intra-moleculaire* waterstofbruggen, die in oplossing niet worden verbroken. Er is aangetoond dat de gevolgde procedure resultaten oplevert die goed overeenkomen met de resultaten van NMR spectroscopie of Röntgen diffractie: technieken die 3-dimensionale structuur-informatie opleveren, met een hoog oplossend vermogen.

Door gebruik te maken van Fourier zelf-deconvolutie en tweede afgeleide spectra wordt de amide I band opgesplitst in de bijdragen door α-helices, β-sheets en β-turns. Dit is de meest kritieke stap in de hele procedure. Onjuist gebruik van deze methodes kan leiden tot de introductie van extra, foutieve pieken die gemakkelijk als structuur-elementen kunnen worden geïnterpreteerd. Hierna wordt, door middel van curve-fit analyse, de oppervlakte bepaald onder de pieken, die gevonden zijn in de eerste stap. De hoeveelheid van de secundaire structuur-elementen wordt uitgedrukt in een percentage van het totale oppervlakte onder de amide I band.

Bepaling van de secundaire structuur van een eiwit wordt pas ècht interessant wanneer de structuur-elementen in het eiwit gelocaliseerd kunnen worden. Door de resultaten van het complete fotoreceptor eiwit te vergelijken met de resultaten van het door proteolyse behandelde eiwit, kan men concluderen dat de carboxy-terminus van rhodopsine een β-sheet-structuur aanneemt en dat de derde cytoplasmatische lus wordt gevormd door een α-helix. Dit is de eerste gedetailleerde analyse van de secundaire structuur van rhodopsine. Naast de zeven, reeds bekende, transmembraan-helices zijn nu ook enkele structuur-elementen toegekend, die verantwoordelijk zijn voor de binding van het G-eiwit of transducine.

In *hoofdstuk 5* wordt een onderzoek naar de interacties tussen het enzym Na^+, K^+-ATPase en fosfolipiden met een toenemend gehalte aan onverzadigde vetzuurketens gepresenteerd. Gebruik wordt gemaakt van relatieve piekverschuivingen in het IR-spectrum als criterium om de hydrofobe interacties tussen de twee componenten (eiwit en lipiden) in een mengsel te kunnen vaststellen.

Zoals afgeleid uit de positieve relatieve piekverschuiving van de specifieke lipide-absorptieband rond 2852 cm^{-1} als functie van temperatuur, verstoort Na^+, K^+-ATPase de ordening van de lipidemoleculen in verzadigde fosfolipide membranen. Inbouw van het enzym in membranen met een grote hoeveelheid meervoudig onverzadigde vetzuurketens leidt bij lage temperatuur tot weinig interactie van het eiwit met deze klasse van lipiden. Uit de verandering

van de eiwit-specifiek amide I band wordt geconcludeerd dat het eiwit onder deze omstandigheden aggregeert (samenklontert). Bij hogere temperaturen ($37 \ ^{o}C$) is deze aggregatie echter verminderd. Hierdoor ontstaat weer een extra mogelijkheid voor hydrofobe interactie tussen het eiwit en de hoog onverzadigde fosfolipiden. Als een gevolg hiervan wordt een betrekkelijk sterke, negatieve verschuiving van de lipidepiek rond 2852 cm^{-1} gevonden. Deze resultaten zijn in overeenstemming met het zogenaamde 'matras model' voor lipide-eiwit interacties, behalve op het punt van eiwit-eiwit interacties in domeinen die uit het membraan steken en niet expliciet in dit model worden behandeld.

Tenslotte behandelt *hoofdstuk 6* de analyse van succinimide derivaten, zoals die gevormd worden in kleine peptide-fragmenten. Deze derivaten vormen het belangrijkste intermediair in het mechanisme van de niet-enzymatische, leeftijds-afhankelijke afbraak van eiwitten *in vivo*. Dit houdt in dat de vorming van een aantal afbraakproducten van αA-crystalline, gevonden in de verouderende ooglens, verklaard kan worden met de hydrolyse van een succinimide. Hoewel de omstandigheden, beschreven in dit hoofdstuk, niet fysiologisch relevant zijn, moet er op gewezen worden dat er in de Natuur een andere route voorkomt, die tot geactiveerde intermediairen leidt, namelijk fosforylering. Een bekend voorbeeld is het enzym Na^{+},K^{+}-ATPase, gepresenteerd in de hoofdstukken 3 en 5. In een katalytische cyclus wordt dit enzym geactiveerd door fosforylering van een asparaginezuur residu (Asp$_{376}$), hetgeen resulteert in een gemengd anhydride. In het geval van Na^{+},K^{+}-ATPase zal er echter geen afbraak van het eiwit plaatsvinden omdat het gefosforyleerde aminozuur zich in een minder flexibel gedeelte van het eiwit bevindt (vermoedelijk in een β-type domein).

Concluderend kan gesteld worden dat FT-IR spectroscopie een elegante techniek is voor de benadering van een veelheid aan biochemische problemen. Hoewel deze techniek het structuuroplossend vermogen van de NMR spectroscopie niet kan benaderen, geeft het toch meer globale informatie over grotere biochemische systemen, waarbij de toepassing van NMR niet mogelijk is. Door combinatie van IR spectroscopie met moderne moleculair-biologische technieken kunnen, op een lokaal niveau, gedetailleerde structuur-functie relaties worden blootgelegd.

Lijst van publicaties

1. Claesen, C.A.A., Pistorius, A.M.A. en Tesser, G.I. (1985) *Tetr. Lett.* 26, 3859–3862.

2. Pistorius, A.M.A., Claesen, C.A.A., Kremer, F.J.B., Rijk, E.A.V. en Tesser, G.I. (1987) *Nucleosides and Nucleotides* 6, 389–390.

3. Pistorius, A.M.A., Groenen, P.J.T.A. en De Grip, W.J. (1993) *Int. J. Peptide Protein Res.* 42, 570–577.

4. Pistorius, A.M.A. en De Grip, W.J. (1994) *Biochem. Biophys. Res. Commun.* 198, 1040–1045.

5. Pistorius, A.M.A., Schuurmans Stekhoven, F.M.A.H., Bovee-Geurts, P.H.M. en De Grip, W.J. (1994) *Anal. Biochem.* 221, 48–52.

6. Sommerdijk, N.A.J.M., Buynsters, P.J.A.A., Pistorius, A.M.A., Wang, M., Feiters, M.C., Nolte, R.J.M. en Zwanenburg, B. (1994) *J. Chem. Soc. Chem. Commun.* 1941–1942.

7. Pistorius, A.M.A. (1995) *Spectrosc. Eur.* 7, 8–15.

8. Wolkers, W.F., Haris, P.I., Pistorius, A.M.A., Chapman, D. en Hemminga, M.A. (1995) *Biochemistry* 34, 7825–7833.

Curriculum vitae

Arthur Pistorius werd geboren op 10 mei 1961 in Breda. Via de MAVO en de HAVO, werd in 1981 het VWO-diploma behaald aan de Thorbecke Scholengemeenschap in Arnhem. In ditzelfde jaar werd de studie scheikunde met extra bijvak biologie begonnen aan de Katholieke Universiteit Nijmegen. Het kandidaatsexamen volgens het oude curriculum vond plaats in oktober 1984. De hoofdrichting organische chemie (prof. dr. G.I. Tesser) omvatte de synthese van (spin-gelabelde) oligonucleotiden. In deze periode werd deelgenomen aan de zevende internationale ronde tafel conferentie over nucleosiden, nucleotiden en hun biologische toepassingen in Konstanz (Duitsland), waar een poster werd gepresenteerd. De tweede hoofdrichting biofysische chemie (prof. dr. C.W. Hilbers), aangevuld met capita farmacochemie (prof. dr. J. van Rossum), werd besteed aan simulatie van 2-dimensionale exchange NMR spectra en aan verkennende ESR metingen aan spin-gelabelde oligonucleotiden. Afstudeerdatum: 25 april 1988.

Van november 1988 tot februari 1993 was hij, in dienst van de stichting SON, verbonden aan het laboratorium voor biochemie van de faculteit der medische wetenschappen, waar het in dit proefschrift beschreven onderzoek werd verricht. Hiernaast werd geparticipeerd in onderzoeken van andere instituten. De resultaten werden gepresenteerd op de jaarlijkse bijeenkomsten van de SON werkgemeenschap "Lipiden en Biomembranen" in Lunteren. Als nevenwerkzaamheden werd eerstelijns ondersteuning verleend bij computertoepassingen en werden diverse practicumassistentschappen vervuld. In het kader van het opleidingsplan werden de cursussen "Proefdierkunde" en "Stralingshygiene-niveau III" met positief resultaat afgesloten.

Zijn hobbies zijn scheepsmodelbouwerij en hockey. Hij is een liefhebber van oude-stijl jazz en klassieke muziek.